GDAŃSK UNIVERSITY OF TECHNOLOGY
Faculty of of Applied Physics and Mathematics

The author of the PhD dissertation: Petr Ershov
Scientific discipline: physics

DOCTORAL DISSERTATION

Title of PhD dissertation: High resolution X-ray diffractometry and reflectometry of semiconductor nano- and micro- structures based on X-ray refractive optics

Title of PhD dissertation (in Polish): Wysoka rozdzielczość dyfraktometria rentgenowska i reflektometria półprzewodnikowej struktury mikro- i nano- oparciu o rentgenowskich refrakcji optyki

Supervisor *signature*	Cosupervisor *signature*
Dr. Anatoly Snigirev	Dr. hab. Anna Perelomova, prof.PG

Gdańsk, 2017

"Who is John Galt?"

Ayn Rand's novel Atlas Shrugged (1957)

TABLE OF CONTENTS

Introduction

The research of new properties of nano- and micro-sized objects with nano-sized detalization requires usage of an instrument that will make it possible to observe not only static objects, but also their dynamics. It requires also developing and modernizing already existing experimental methods of material research.

The new generation of synchrotrons, together with refractive optics, has opened up opportunity for research in the field of micro-sized materials. For example, a full-field X-ray microscope allows a researcher to make a view on objects with nanometer resolution in normal conditions without any special preparation of the objects [1, 2]; phase-contrast X-ray micro-imaging improves visibility of transparent for X-rays objects [3]; with the use of refractive lenses X-ray high resolution diffractometry can yield information about the symmetry and periodicity of an object in just one shot [4]; refractive optics for creating a coherent micro-spot for novel phase retrieval methods like ptychography[5] can perform detailed reconstructions of nano-objects.

Apart from excellent microfocusing [6, 7] and imaging applications[2, 8], one of the most notable and useful properties of compound refractive lenses (CRL) [9, 10] is its intrinsic ability to perform one- or two- dimensional Fourier transforms. In the case of hard X-rays, these properties have been demonstrated both theoretically[11] and experimentally[4, 12]. This kind of the Fourier transform has been successfully applied in the studies of colloidal and photonic crystals [1, 13].

In spite of the progress made in X-ray refractive optics, many synchrotron facilities which have been outdated methods and techniques incapable of using synchrotron radiation to its best advantage. It is noteworthy that today many high-resolution X-ray diffraction (HRXRD) and X-ray reflectivity (XRR) beamlines are based on the non-effective and complex conventional approaches.

Aims and objectives

Novel approaches in high-resolution X-ray diffractometry and reflectometry of semiconductor micro- and nano-structures based on CRL are discussed in this thesis. The overall aim of this work is to modernize the existing HRXRD and XRR methods by increasing the angular, space and time resolution for present-day synchrotron sources.

Other objectives of this thesis are as follows:

- To analyze conventional X-ray high-resolution methods of diffractometry and reflectometry.
- To design and implement an alternative X-ray optical scheme of HRXRD and XRR based on refractive X-ray lenses.
- To perform experiments and process data in order to generate the results demonstrating the advantages of new methods.

Ultimately, the two concepts as follows will be studied experimentally:

- X-ray Compound Refractive Lenses Fourier Transform (CRL FT) for HRXRD tasks.
- Hard X-ray Reflecto-Interferometer (HXRI) for X-ray Reflectometry tasks.

The list below provides an overview of the contents of the chapters.

Chapter 1. In this chapter the foundations of modern X-ray physics are outlined, as well as those of the X-rays nature and properties, X-ray interaction with the matter, modern X-ray optics and X-ray sources. The construction and features of the CRL will be described, and the main concept of the lenses Fourier transform (LFT) will be discussed.

Chapter 2. This chapter focuses on the fundamental laws and theory of the X-ray diffractometry and reflectometry: Bragg's law, the reciprocal space theory and traditional X -ray diffractometry and reflectometry methods.

Chapter 3. This chapter discusses refractive optics-based novel approaches in X-ray diffractometry and reflectometry, namely, a CRL FT technique for HRXRD and the HXRI concept for X-ray reflectometry.

Chapter 4. The experimental results of applying X-ray optical approach to the study of Si microstructures (SiO_2 lattice deposited on silicon and profiled silicon lattice), Si-Ge nano-heterostructure, Si_3N_4 sub-micron membranes, are presented in this part of the research, together with the study of 100 nm PMMA film degradation affected by the X-ray radiation.

Chapter 5. Conclusions and further outlook.

X-ray sources and optics

1.1 The nature of X -rays. Interaction of X-rays with matter

Discovered by William Roentgen in 1895[14], X-rays are a form of electromagnetic radiation with wavelengths ranging from 0.01 nm to 10 nm[15] (table 1). However, the regions of electromagnetic spectrum do not have clear-cut division. X-rays have a wavelength much shorter than that of ultraviolet, and longer ones than that of gamma-rays produced by nuclear reactions.

Historically, X-rays began to be used in the medical sphere due to their penetration properties. After more than 100 years of development, X-rays are still used as a powerful analytical tool of materials study.

Table 1. Electromagnetic spectrum

Radiation	Wavelength	Photon energy
Gamma ray	<0.01 nm	> 124 keV
X-ray	0.01 nm-10 nm	124 keV - 124 eV
Ultraviolet	10 nm - 400 nm	124 eV - 3 eV
Visible Light	400 nm - 750 nm	3 eV - 1.7 eV
Infrared	750 nm - 1 mm	1.7 eV - 1.24 meV
Microwave	1 mm - 1 m	1.24 meV - 1.24 μeV
Radio	> 1 m	<1.24 μeV

As an electromagnetic wave, X-rays are scattered by charged particles. The photons of electromagnetic radiation are known to have the property of wave-particle duality. Due to the particle nature of the photons, the interaction with charged particles can result in emitting same-frequency photons (the case of elastic interaction), or photons with less energy (nonelastic interaction, or Compton Effect). Due to wave nature, the processes of refraction, reflection, scattering, diffraction, interference, dispersion, absorption and polarization can take place (*Fig. 1*).

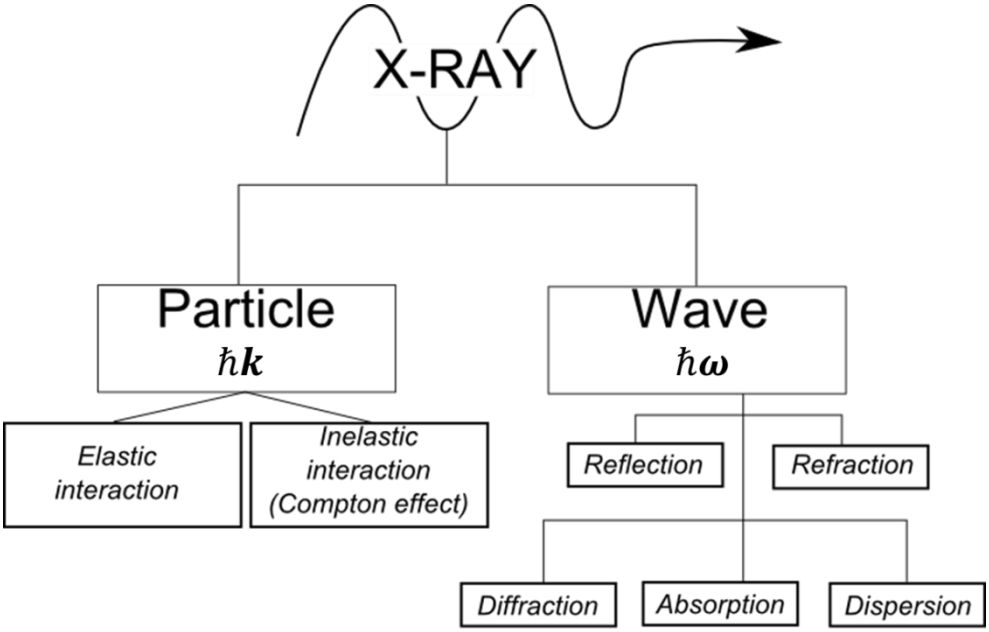

Fig. 1. Diagram of X-rays main interaction processes with the matter.

For a long time, it was unclear whether X-rays refract or not. Nevertheless, after a detailed X-rays study, it has become apparent that they do refract, but the effect is negligible. The law of refraction is the same as that for visible light (*Fig. 2*) and it is embodied in Snell's law [16].

Theory says that material refraction index n is the ratio of the phase velocities in vacuum c and in medium v:

$$n = \frac{c}{v} = \sqrt{1+\chi} \approx 1 - \delta + i\beta, \qquad (1)$$

where χ is dielectric susceptibility, δ is the decrement of the refractive index, β is the absorption index. For X-rays β and δ the values are in the order 10^{-6}, causing low refraction and absorption in comparison with the visible light region of electromagnetic spectrum [15].

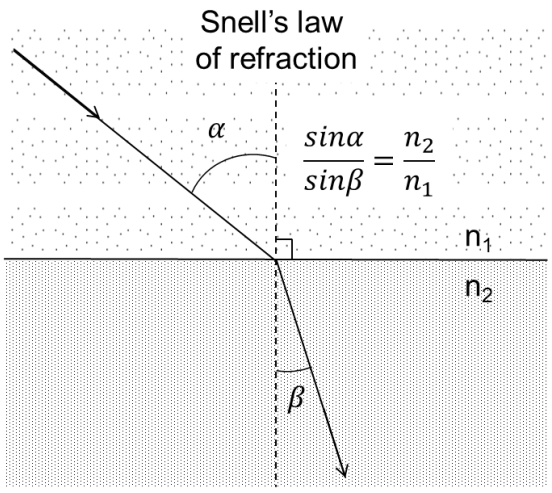

Fig. 2. Illustration of Snell's law satisfactory for visible light and X-rays.

X-rays absorption obeys the exponential law of the decrease in intensity *I(t),* like the visible light:

$$I(t) = I_0 e^{-\mu t} \tag{2}$$

where I_0 is the incident beam intensity, t is the path passed by a beam inside a medium, μ is the linear absorption coefficient of a material, which is defined as

$$\mu = \frac{4\pi}{\lambda}\beta(\lambda) \tag{3}$$

The real and imaginary part of a refractive index for different materials and wavelengths λ are recorded in [17], and basic X-rays wave interactions with the medium could be predicted and analyzed.

1.2. Modern X-ray sources

Started form the Crookes tubes [14], X-ray physics is currently well-developed. Along with the specially designed laboratory sources, huge research facilities exist - namely synchrotrons where vast research in biology, chemistry and physics are carried out.

The main characteristics of X-ray sources are: photon flux $\mathcal{F}$, brilliance $\mathcal{B}$, spectrum $\Delta\lambda$ and source size [18, 19]. X-ray flux $\mathcal{F}$ is defined as the number of photons N per second passing through a defined area. Brilliance $\mathcal{B}$ is determined by the specific number of photons N produced by an X-ray source covering area S within finite time t at defined spectral interval $\Delta\lambda/\lambda$ and observed at solid angle Ω:

$$\mathcal{B} = \frac{N}{t \cdot \Omega \cdot S \cdot \Delta\lambda/\lambda} \tag{4}$$

Brilliance $\mathcal{B}$ characterizes the distribution of flux $\mathcal{F}$ in a space and angular range, and it determines the smallest spot onto which an X-ray beam could in principle be focused.

For an X-ray optical application (X-ray phase contrast imaging[3], interferometry[20, 21], focusing/defocusing[10] and microscopy), the source size appears to be an important parameter. For ESRF, for example, this parameter is tens of microns[22], and for a laboratory sealed tube it stands at faction of a millimeter[23].

X-ray radiation from the tubes and synchrotrons is produced by electron- accelerated movement. In a sealed tube (*Fig. 3*), X-ray radiation is generated by electrons bombarding the special target - an anode. Cathode-produced electrons are accelerated by electromagnetic field and collide with anode. The X-ray source size depends on the size of the area in which it is possible to focus the electron beam.

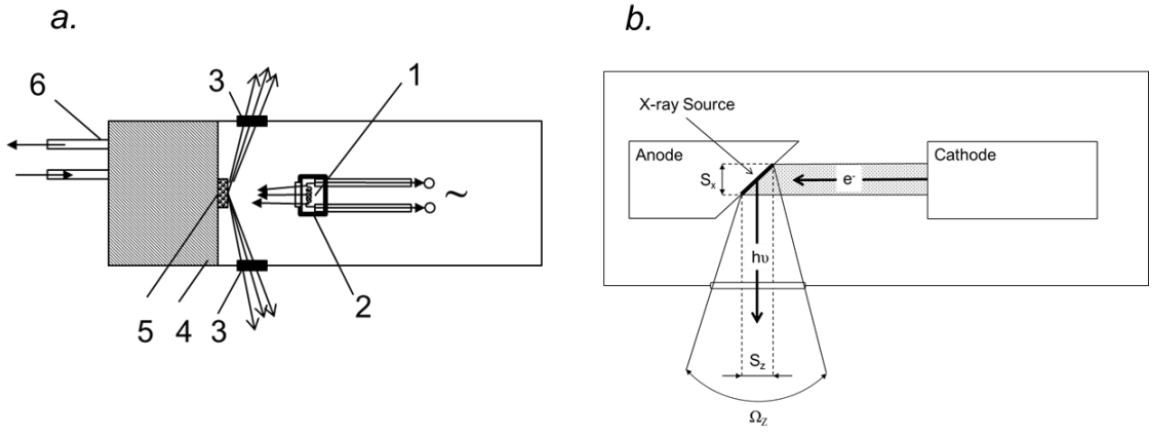

Fig. 3. A sealed X-ray tube. a. Tube construction: 1 – cathode filament, 2 – focusing system, 3 – X-ray window (usually beryllium foil), 4 – protective cover, 5 – anode, 6 – cooling system. b. The main sources' parameters are: size(S) and angular size (Ω). The illustration shows projections S_z and Ω_z.

After the interaction between electrons and the anode, X-rays are generated, to be further transmitted through special windows. The disadvantage of this type of X-ray source is low efficiency of the generated radiation. The loss of energy is accounted for anode heating.

The X-ray tube emission spectrum is a continuum of different wavelengths with intense and sharp lines on it. That lines are called characteristic lines. This continuum corresponds to electrons braking emission (bremsstrahlung, *Fig.* 4). Characteristic lines in a spectrum

are the results of electrons transitions between inner atom shells (*Fig.* 4). These transitions are induced by X-ray photons which strikes electrons from inner atom's shells. The characteristic lines wavelengths are determined by anode material (atoms shell configuration).

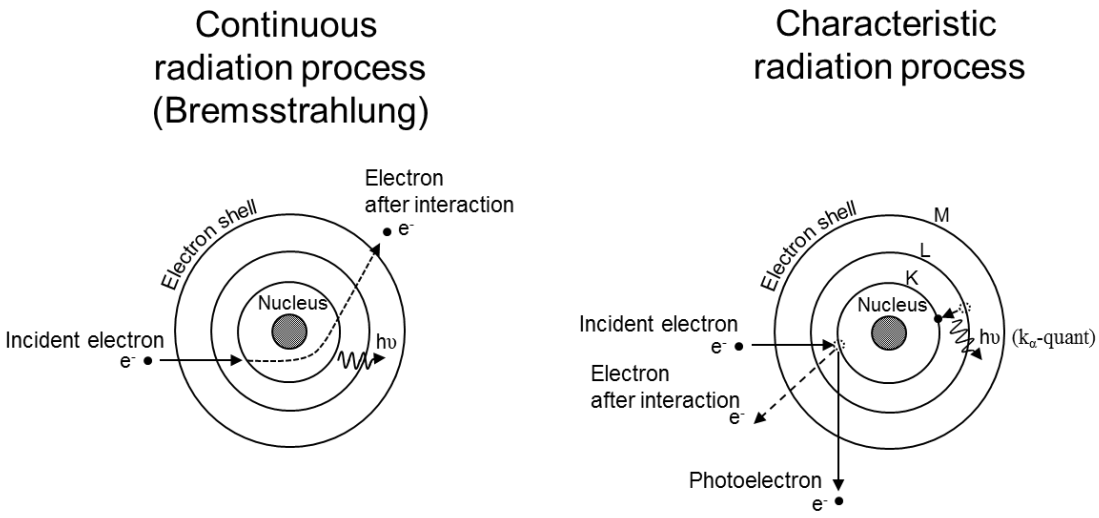

Fig. 4. Continuous radiation process(left) and characteristic radiation process(right).

The beginning of the X-ray tube spectrum is usually at 1-3KeV (*Fig.* 5). End of the spectrum is determined by value of applied high voltage (as an example, for standard operation of XRD Cu X-ray tube the high voltage is 40kV which corresponds to 40KeV ending of an emission spectrum). Every characteristic line is corresponded to the particular transition between atomic shell.

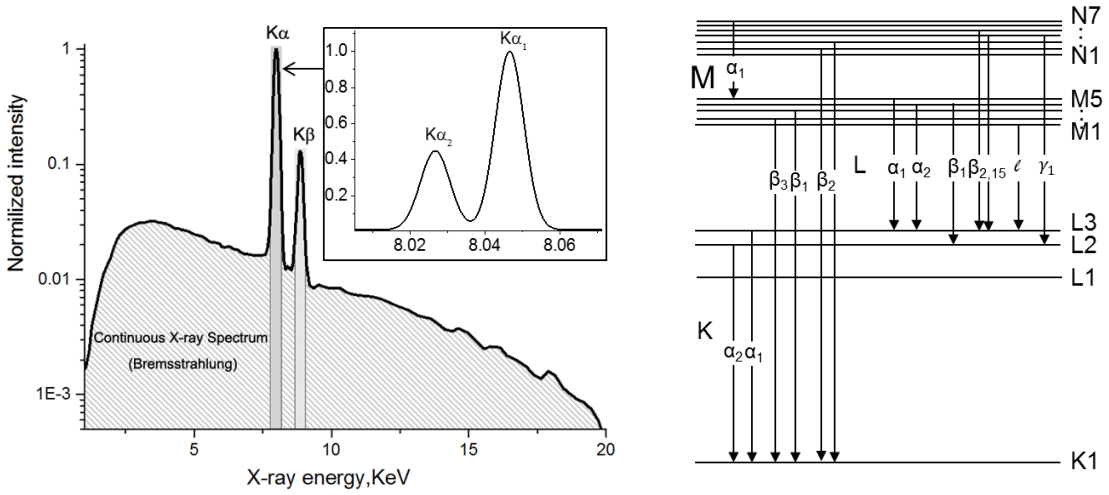

Fig. 5. X-ray tube emission spectrum of Cr anode at 20kV HV (left graph, adapted from [24]) and possible transitions between inner atomic shells (right scheme).

The X-rays radiates in all directions after interaction between electron beam and anode (*Fig.* 6). At angels close to the anode surface (less than 3 degree), the radiation level is low. But after 5-6 degree, the intensity level increase quickly and saturate. The angle of an X-ray intensity saturation is depended on anode material. For low-Z materials(Z<28) the saturation starts at 20 degree and for high-Z materials saturation starts at 3-6 degrees.

The take-off angle is the angle between anode surface and exit window and it is chosen according to optimal intensity level and X-ray source projection size.

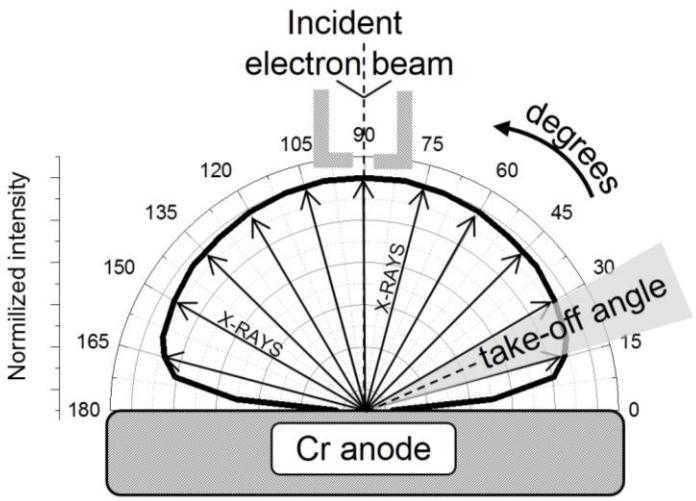

Fig. 6. X-ray radiation pattern of conventional X-ray tube (adapted from [25]).

The X-ray source size is determined by the electron beam projection on an anode surface. For conventional X-ray tubes that size is from 1mm to 10mm. The X-ray tube exit window cuts a part of an X-ray radiation and performs beam pre-collimation. Exit window could transmit a line source projection (line focus configuration) or a dot source projection (point focus configuration) according to the relative position of window and source.

The most popular and usable source projections of X-ray tube are 10 mm·1mm (line focus) and 1mm·1mm (point focus). For XRD and XRR applications commonly used line focus which provides high X-ray fluence on samples with sizes more than 5mm·5mm.

The more effective way of an X-ray generation is to use specialized electron accelerators, or synchrotrons (*Fig.* 7). It is possible to generate a high X-rays flux by electron movement with relativistic velocities on a circular trajectory.

Electrons from an electron gun (*Fig. 7(1)*) are accelerated in a linear accelerator (LINAC) (*Fig. 7(2)*) into an evacuated booster ring (*Fig. 7(3)*). Then they are injected into a storage ring (*Fig. 7(5)*). There, they are maintained in a closed path with the help of bending magnets (*Fig. 7(9)*) at arc sections. The beamlines consisting of front end (*Fig. 7(7)*) and

hutches (*Fig. 7(8)*) make use of the radiation emitted form insertion devices (*Fig. 7(6)*) and bending magnets. Hutches are special rooms for beam conditioning or experiments. The energy lost by radiation is replenished by radio frequency (RF) supply (*Fig. 7(4)*).

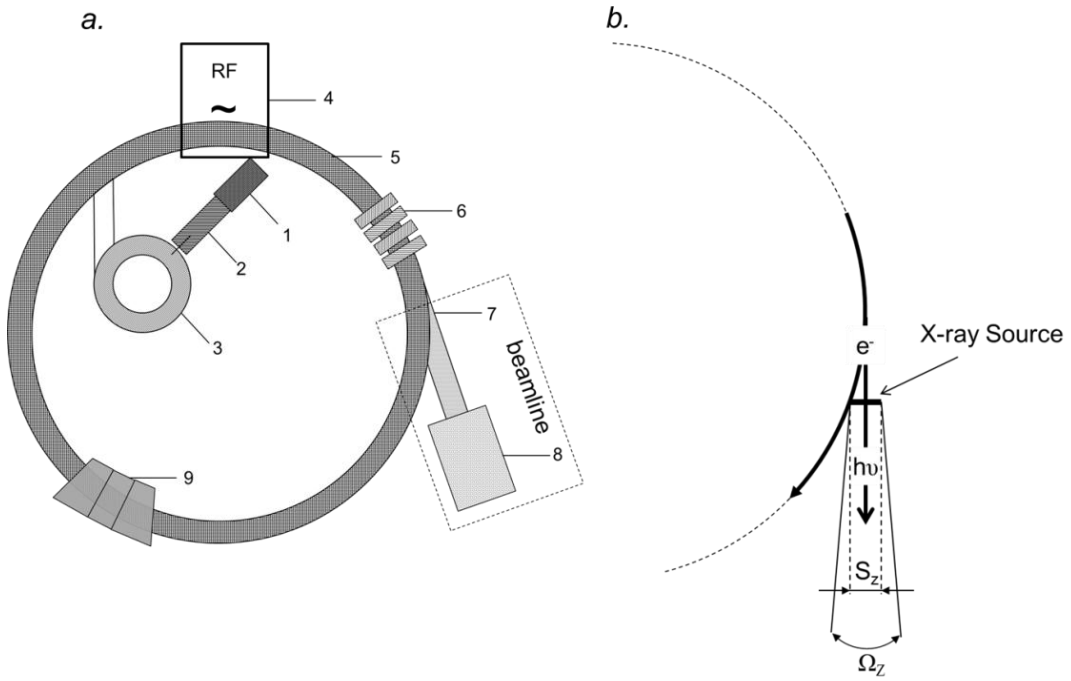

Fig. 7. Specialized electron accelerator for X-ray's generating – a synchrotron. a. A schematic of the most important components of a modern synchrotron source. 1 – electron gun; 2 – linear accelerator (LINAC); 3 - booster ring; 4 - radio frequency (RF) supply; 5 - storage ring; 6 - bending magnets; 7- front end; 8 – hutches; 9 - insertion devices. b. Main X-ray source parameters: size(S) and angular size (Ω). The illustration shows projections S_z and Ω_z.

The main advantage of synchrotron X-ray source is not only the brilliance but also it directivity. The electrons which move with relativistic velocities produce directed X-ray radiation (with divergence less than 1mrad).

On a synchrotron, the devices which produce X-rays are bending magnets, wigglers and undulators (*Fig.* 8). Bending magnet produce X-rays by turning of electron bunch. The divergence in one direction of emitted X-rays depend on a relativistic parameter γ.

$$\gamma = \frac{1}{\sqrt{1-\frac{\vartheta^2}{c^2}}} = \frac{\mathcal{E}e}{mc^2} \tag{5}$$

Where ϑ –electron velocities, c – speed of a light, $\mathcal{E}$e – electron energy, m - electron mass. For an average storage ring with energies about 5GeV, the X-ray source produced by

bending magnets has size about 100 μm and angular size approximately 0.1 mrad (in one direction)[26].

For increasing X-ray sources brilliance were developed special insertion devices. That are wigglers and undulators. Wiggler perform additional electron movement at horizontal plane by magnets with alternating poles.

Undulator similar to wiggler consists of periodic lattice of magnets, but due to the specially chosen period *N* of magnets lattice, X-rays sub-beams produced by each curved movement of electron bunch interfere constructively with each other. This interference decreases X-ray source spatial, angular sizes and length of an emission spectrum.

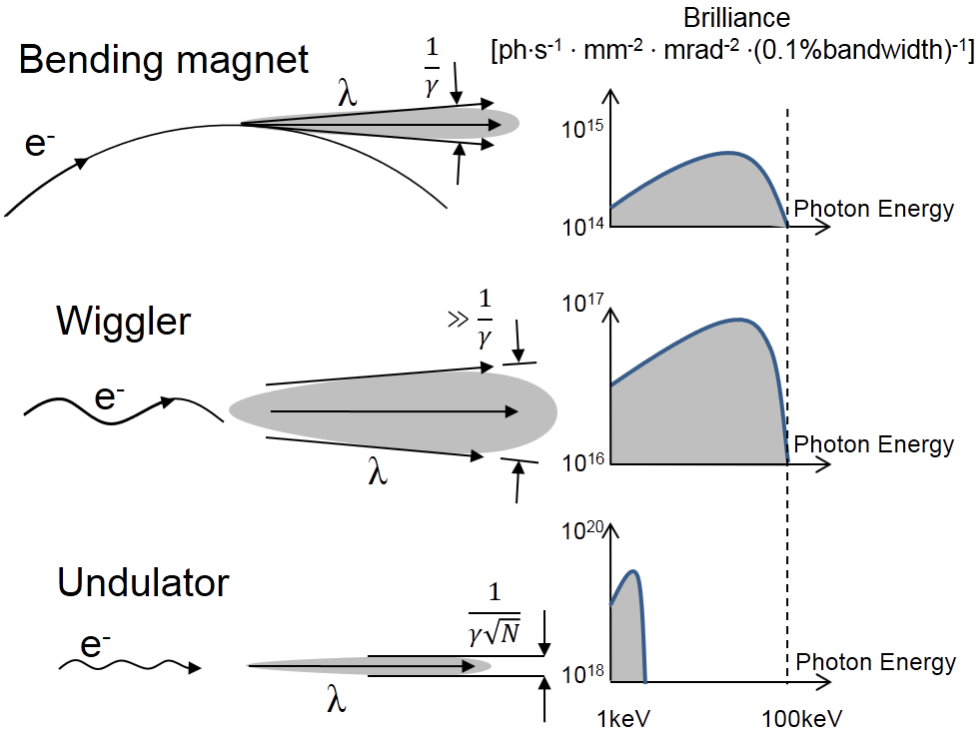

Fig. 8. Different sources of synchrotron radiation: bending magnet, wiggler, undulator.

The average undulator X-ray source spatial sizes are 100um·40 um, and angular sizes are 100urad·20urad for horizontal and vertical directions correspondingly at ESRF.

By the way, decreasing of horizontal X-ray source size and producing almost symmetrical X-ray source are planned at ESRF [27]. This innovation is important for increasing brilliance and coherency of synchrotron X-ray source.

One of the feature of the X-ray generation by synchrotron is the impulse structure of emission. The average X-ray pulse size is 20 ps and distance between pulses is from 3 ns to

3000 ns and it determined by synchrotron operation regime (filling mode http://www.esrf.eu/Accelerators/Operation/Modes).

The Free Electron Laser(FEL) is one of the most perspective and effective generators of X-rays. Presently two brilliant FEL's (for hard X-rays) are operated. That are LCLS (https://www6.slac.stanford.edu/facilities/lcls) and SACLA(http://xfel.riken.jp/eng/). The XFEL(http://www.xfel.eu/) is planned to start operating in 2017 in Hamburg, Germany.

The basic principle of FEL operation is SASE (Self Amplified Stimulated Emission). SASE is an effect of a coherent amplification of an X-ray emission produced by electron bunch moving at long undulator (*Fig.* 9). This effect is reached not only by undulator length but also by a special preparation of an electron bunch, which is smaller than at synchrotrons.

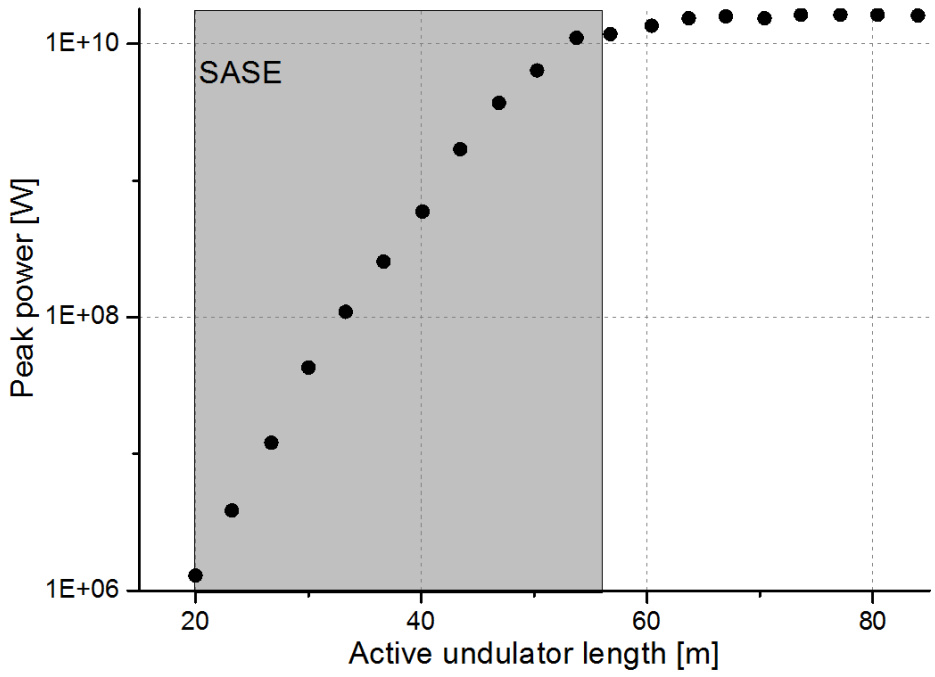

Fig. 9. The measured power emitted from the LCLS as a function of undulator length [19].

To improve laboratory capabilities in comparison with the synchrotron facilities, the new generation of microfocus X-ray tube – MetalJet systems[28] - was developed, with melted metal used as an anode (*Fig. 10*). Due to the liquid state of the anode, the electron power density was highly increased - up to ~2500 kW/mm^2 in comparison with older rotating anode technology [26] which reached the electron density of ~500 kW/mm^2.

In new laboratory MetalJet systems with the source size about 5 μm[29], brilliance is equal to that of 1st generation-synchrotrons.

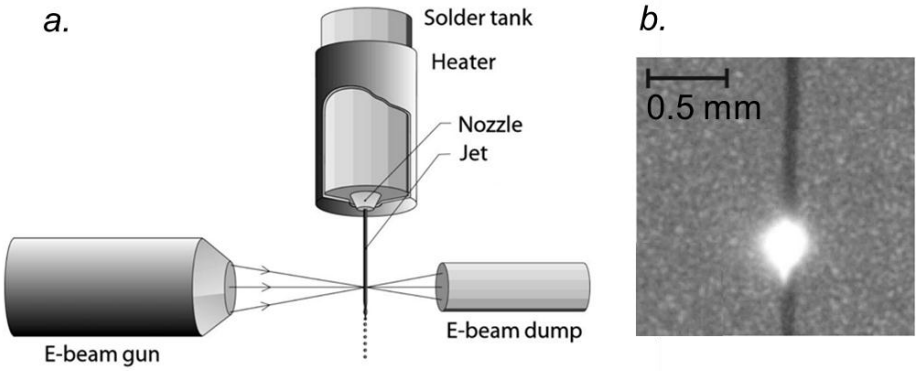

Fig. 10. The new type of a laboratory microfocus X-ray source, MetalJet. a. A special nozzle produces a fine jet of liquid metal and E-beam gun focuses electrons on a jet. b. Flash photograph of 75 μm tin jet targeted by 150 μm FWHM electron beam (adapted from [28]).

The MetalJet spectrum is the same as spectrum of typical solid state X-ray tube with Ga anode. The main MetalJet technological difficulty is producing stable laminar jet. The advantage of such laboratory X-rays generator is possibility to produce an X-ray source with small size and high brilliance (table 2). Unfortunately, the X-ray emission of such X-rays generator is not directed and X-ray flux decreases drastically with the distance from the X-ray source (proportional to r^{-2}, where r - distance to the source). Nevertheless, MetalJet is perfectly suitable for phase contrast X-ray microscopy.

Table 2. The X-ray sources brilliance in 2014

Type of a source	**Brilliance phot. /(sec·mrad^2·mm^2·0.1%bandw.)]**
Cu sealed tube	10^7
Excillium MetalJet	10^{11}
1st generation of SRF	10^{12}
2nd generation of SRF	10^{15}
3rd generation of SRF	10^{21}
LCLS	10^{33}

1.3. Modern X-ray optics

X-ray optics was well developed over the past 50 years and there are new variations of it were appeared. The main driving force was the development of a new coherent X-ray source such as the third generation of synchrotrons. Production of X-ray optics requires high-precision surface and materials processing technology, due to the high sensitivity of X-rays to the inhomogeneity.

X-rays optics could be divided into the following groups: refractive, reflective, diffractive, waveguide and capillary[30].

Reflective optics type is based on the mirrors. Its principle of operation is grounded on the X-ray reflection by a surface with elliptical or parabolic shape. Depending on the surface, optics will have one or two focal points.

If mirror's surface profile is parabolic, the mirror has one focus. If mirror's surface profile is elliptic mirror has two focus. By placing a point x-ray source at the parabolic mirror focus, one can obtain quasi-parallel beam (*Fig.* 11). Such mirror's (Göbel mirrors) are used at diffractometers for collimation and monochromatization of the X-ray beam. X-ray beam is focused by placing a point X-ray source at the focal point of the elliptical mirror (*Fig.* 11).

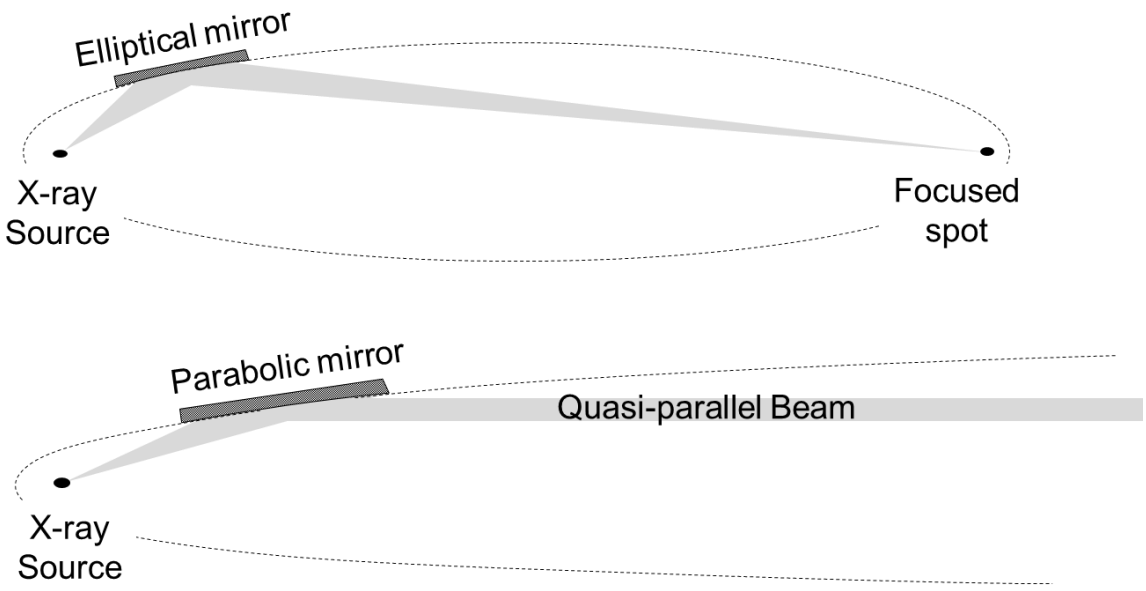

Fig. 11. The common arrangement of elliptical and parabolic mirrors relative to the point X-ray source.

For the reflective optics, there are two geometries: mirrors arranged directly one with another (Montel optics), mirrors situated one after the other (Kirkpatrick–Baez optics) (*Fig. 12*).

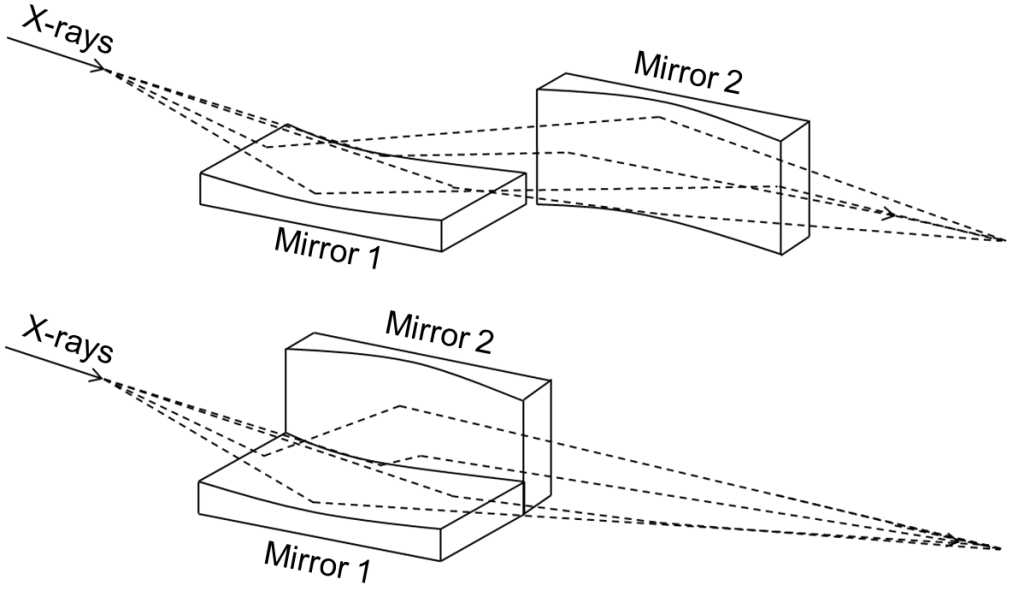

Fig. 12. Two geometries of mirrors placement: Kirkpatrick–Baez (upper image) and Montel (bottom image).

Depending on the optics type (Montel or Kirkpatrick-Baez), they have various applications. For example, a compact Montel optics is used in X-ray diffraction, since it increases intensity of diffraction reflections and the X-ray diffractometer resolution.

Kirkpatrick-Baez system is most often used on synchrotrons due to the possibility of their accurate adjustment to the detriment of the scheme compactness.

As the mirror for reflecting optics a polished silicon or specially manufactured multilayer mirror can be used, wherein the light layer (with a small atomic number Z, for example, silicon) is alternated with a heavy layer (e.g., tungsten).

Due to the multilayer mirror design, it is possible to achieve a high reflectance for the higher value of the angle of reflection. The formula for reflection angle θ is:

$$2dsin\theta = n\lambda \tag{6}$$

where d is the layer's period, n is the order of reflection and λ is the wavelength of X-rays. However, one can use a special calculation program for accurate estimation of mirror parameters, which takes into account the surface and interfaces roughness.

Fresnel zone plate (FZP) relates to the X-ray diffraction optics. The diffraction of radiation on alternating zones (*Fig. 13*) is provides focusing of an X-ray's which satisfy the formula:

$$2r_n dr_n = mF\lambda \tag{7}$$

where $2r_n$ is the zone plate diameter, dr_n is the outer zone width, m is the diffraction order and F is focal distance of FZP.

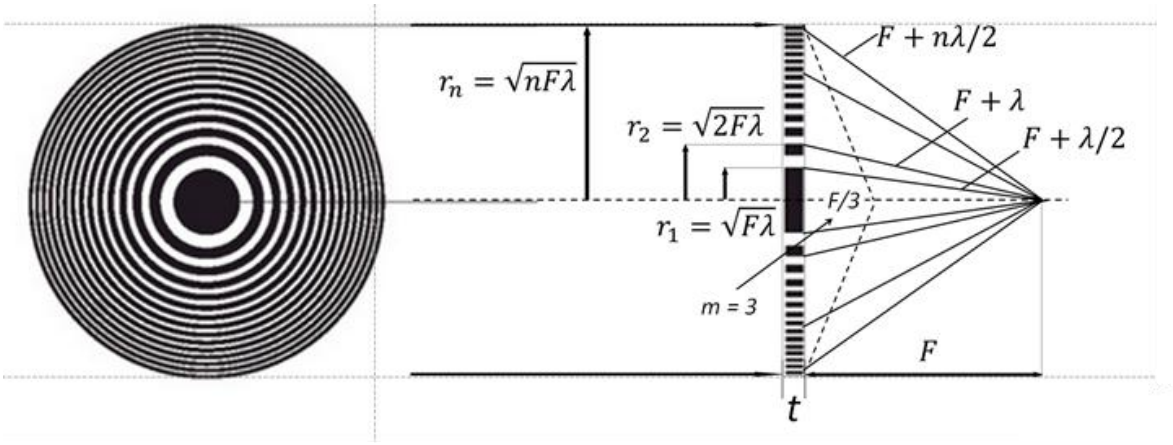

Fig. 13. Fresnel zone plate design.

Zone plate forms three focuses. FZP may serve both as the focusing lens, and as the lens of the imaging of an object. For optimal performance of FZP, one should use extra optical elements: the aperture and the beam stop. Order Sorting Aperture(OSA) is used to select a particular FZP focus (*Fig. 14*). Beam stop is required to block parasitic orders. The figure 14 shows a typical microscopy scheme based on FZP with the OSA and the beam stop.

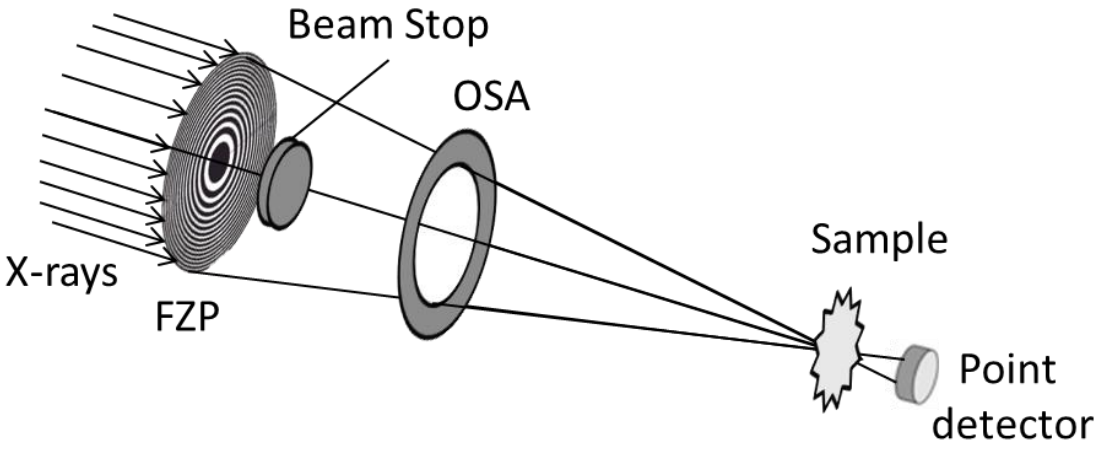

Fig. 14. The X-ray microscopy scheme based on a FZP with OSA and beam stop arrangement.

There are three types of FZP: amplitude, phase and kinoform (*Fig. 15*). In phase FZP, zones are formed by a phase shift of π, and in amplitude by the absorption in a zone. Despite its popularity, FZP efficiency is not high and does not exceed 40%.

To improve the FZP efficiency, kinoform FZP was proposed. The special shape of the kinoform FZP zones enlarges its effectiveness for the hard X-ray energy range [31]. FZP resolution is determined by the width of the last zone. The main technological challenge is to create perfect last zone. For that purpose, the multilayer zone plate has been proposed, which is formed by sputtering instead of etching.

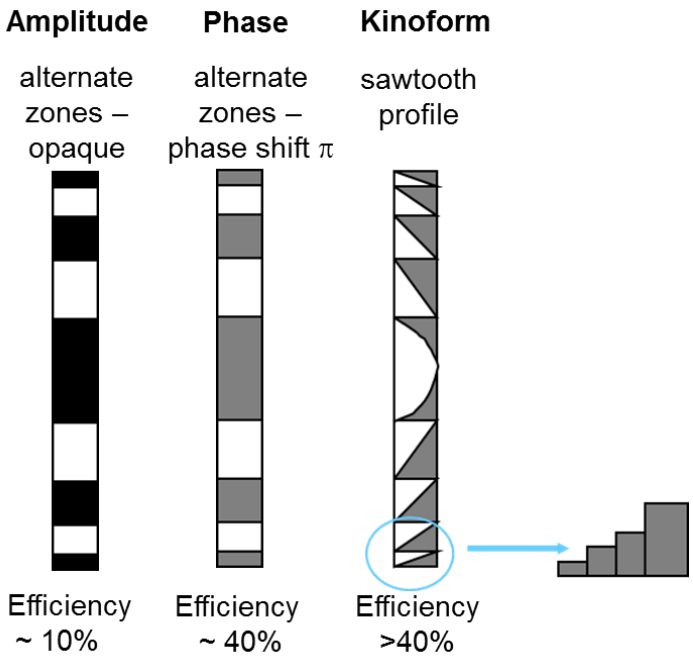

Fig. 15. The three main types of FZP: amplitude, phase and kinoform.

Kinoform multilayer zone plates yields efficiencies over 40%[32].

Capillaries are also used as an X-ray optics. Application of such optics is in focusing the radiation of a weak non-coherent X-ray source. For example, for laboratory X-ray spectroscopy capillary X-ray optics is preferred due to the requirements for the high flux despite of minimum focal spot.

Capillaries are made from a glass. By special technologies they give a special form. Capillary optics has a focal plane independent of wavelength due to the total external reflection from the walls of the capillary. Capillary optics can base on one (mono-capillary) or several capillaries (poly-capillary optics) (*Fig. 16*).

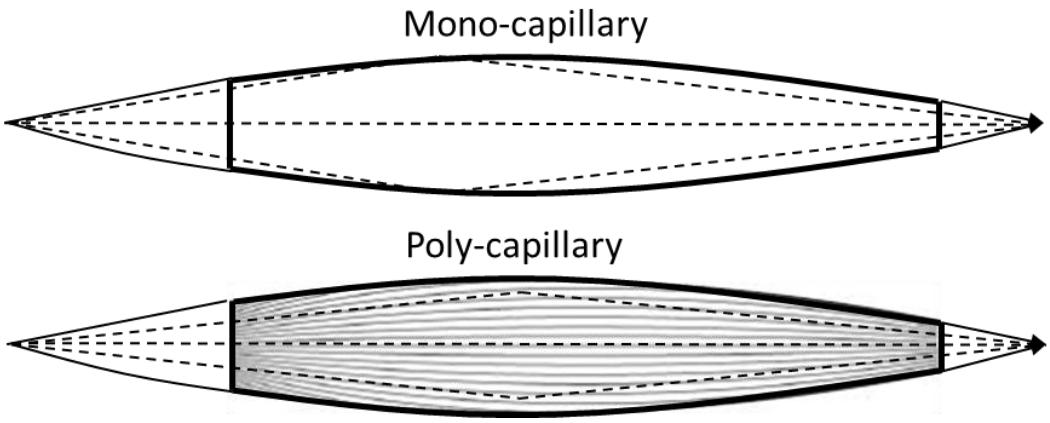

Fig.16. Mono- and poly-capillary X-ray optics.

An X-ray planar waveguide is a thin film resonator in which a low absorbing material is situated between two metal layers (*Fig. 17*). The refractive indexes of metal layers are smaller than refractive index of the low absorbing layer (resonator film). For a particular grazing incidence angles, a resonance takes place inside the resonator film. Such optics is less popular due to the low an X-ray focusing efficiency.

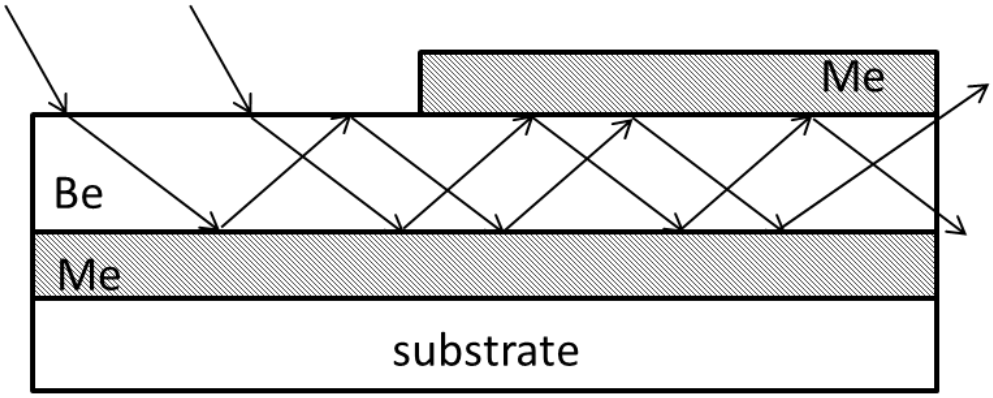

Fig.17. The waveguide X-ray optics.

Bragg-Fresnel optics is a perfect crystal with a zone structure etched on its surface(*Fig. 18*) [33]. The focusing of the radiation is achieved by the π phase shift at Bragg reflection in the crystal. This optics is effective for hard X-ray range. The focused radiation is monochromatized by a crystal.

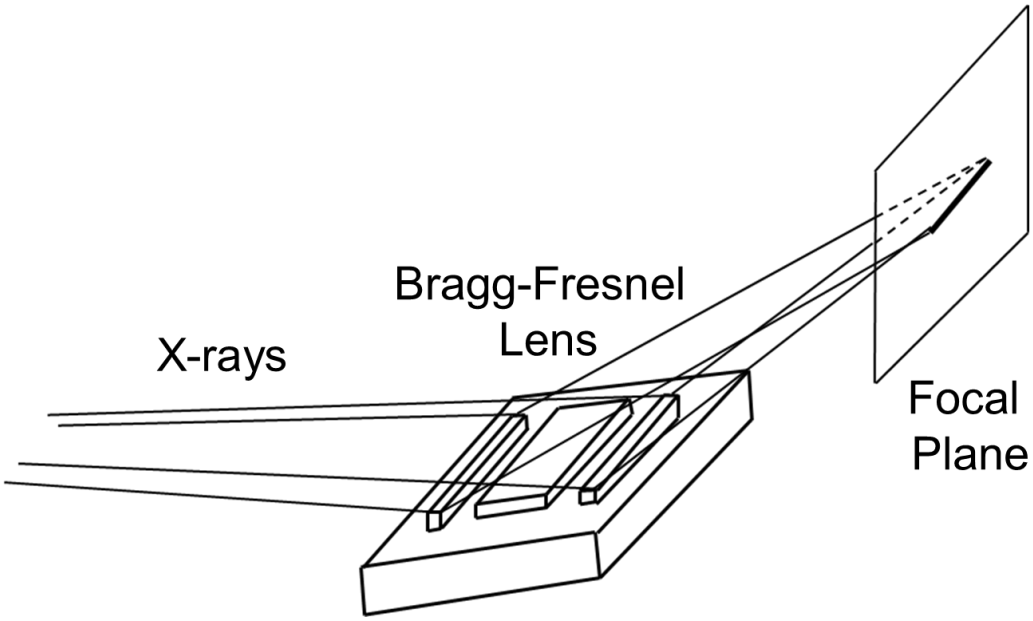

Fig. 18. Bragg-Fresnel X-ray optics.

Phase shift $\Delta\phi$ is determined by the formula:

$$\Delta\phi = 4\pi d\frac{\chi_0}{\lambda^2}h \tag{8}$$

where d is the crystal lattice period, h is the thickness of the etched zone, λ is the X-ray wavelength and χ_0 is the Fourier component of a crystal polarizability.

Perfect crystal with a specific thickness can focus an X-ray beam with wavelength λ which satisfies an equation:

$$t = \frac{\lambda L}{2\Lambda_S\,(sin\theta_B)^2}$$

$$\Lambda_s = \frac{\lambda cos\theta_B}{|\chi_{rh}|C_s} \tag{9}$$

$$C_s = \begin{cases} 1, & s = \sigma \\ \cos 2\theta_B, & s = \pi \end{cases}$$

where L is the source-to-detector distance, θ_B is the Bragg angle, χ_{rh} is the polarizability of the crystal, Λ_s is the extinction length, s is the polarization of X-rays (*Fig.* 19). That optics is based on dynamical diffraction phenomena. There are different focal spot positions for different wavelengths.

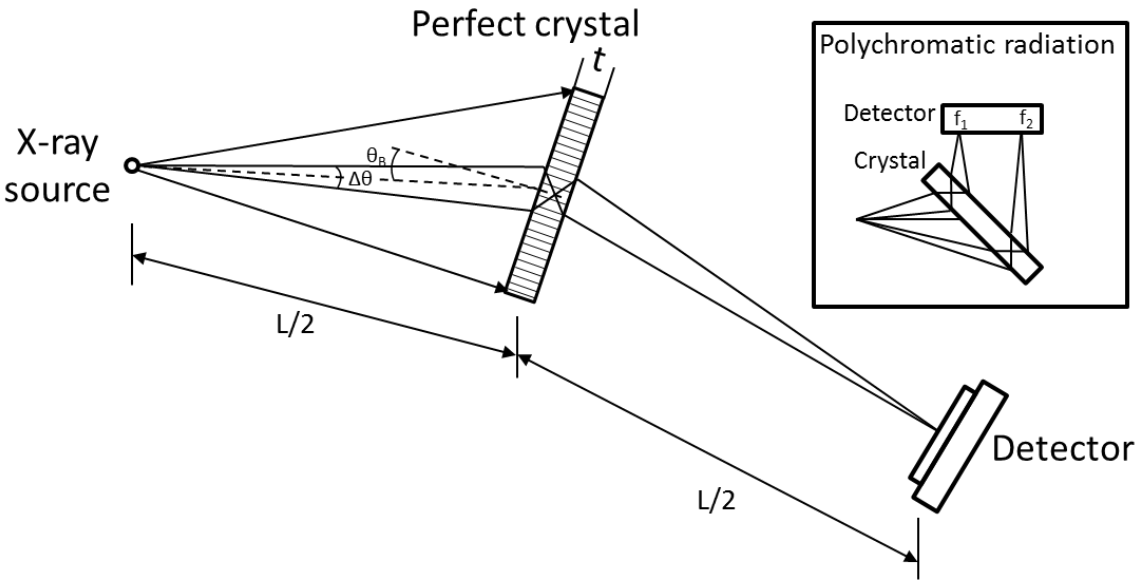

Fig.19. Dynamical focusing by a perfect crystal.

Pinhole is also an X-ray optics. It could be used as an imaging device (as an objective) or as a collimator (*Fig.* 20). As an obscure camera for visible light, pinhole could give magnified image of an object at X-rays. It is widely used for X-ray source monitoring.

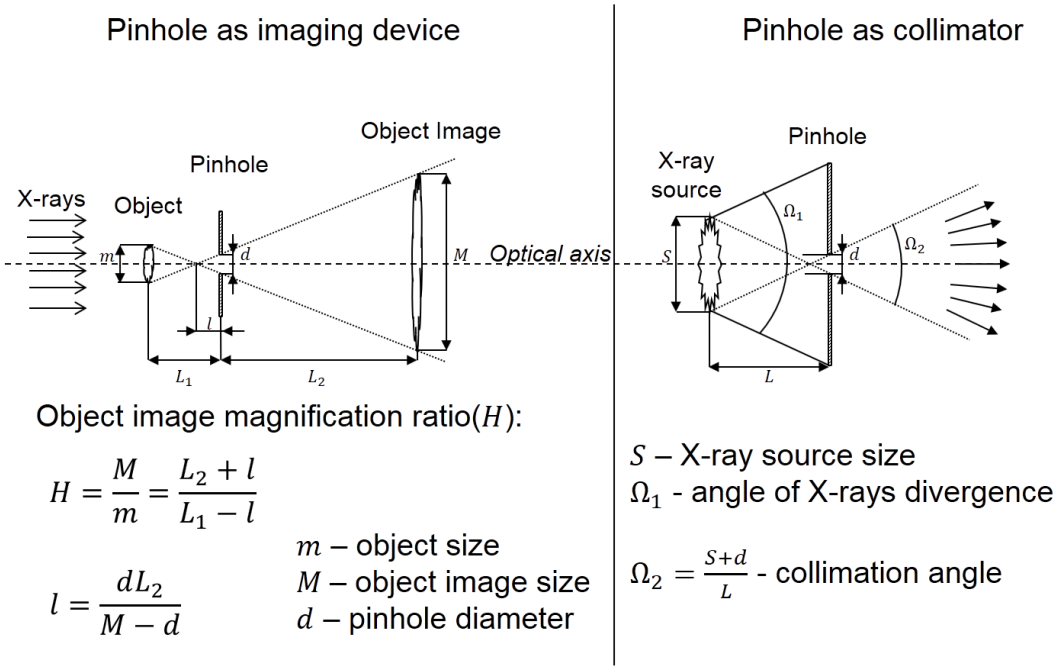

Fig. 20. Two experimental scheme of pinhole application.

Pinholes (*Fig.* 21) are manufactured from high-Z materials (Pt, Ta, Pb) to be able to block hard X-rays.

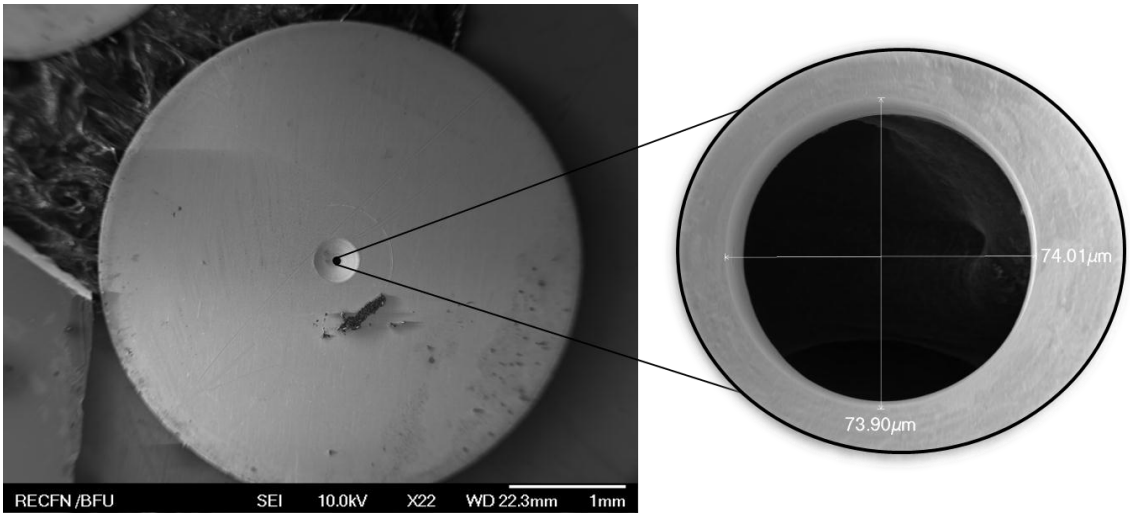

Fig. 21. SEM image of a pinhole used as an X-ray optics. The quality of a hole is almost perfect. That is necessary for an X-ray optical applications.

1.4. Compound Refractive Lenses

For the reason of a small refractive index of materials for X-rays, refractive optics has not been developing for a long time. Curved mirrors, Fresnel zone plates and crystals were the main focusing instruments [30]. Compound refractive lenses (CRL) were proposed for focusing high-energy X-rays in 1996 [9].

The idea was to use "voids" in a material as refractive lenses for focusing, due to the fact that the refraction index in the air or vacuum is higher than that for solid materials. However, since the order of refraction is small, effective focusing requires including the additional lenses into a stack.

As it was shown, focusing by CRL satisfies the formula for a thin lens adjusted for X-rays (*Fig. 22*):

$$F \approx \frac{R}{2N\delta} \tag{10}$$

where R is a "void" radius of curvature, N is the number of lenses in a stack, and δ is the decrement of refractive index, F is a CRL focal distance.

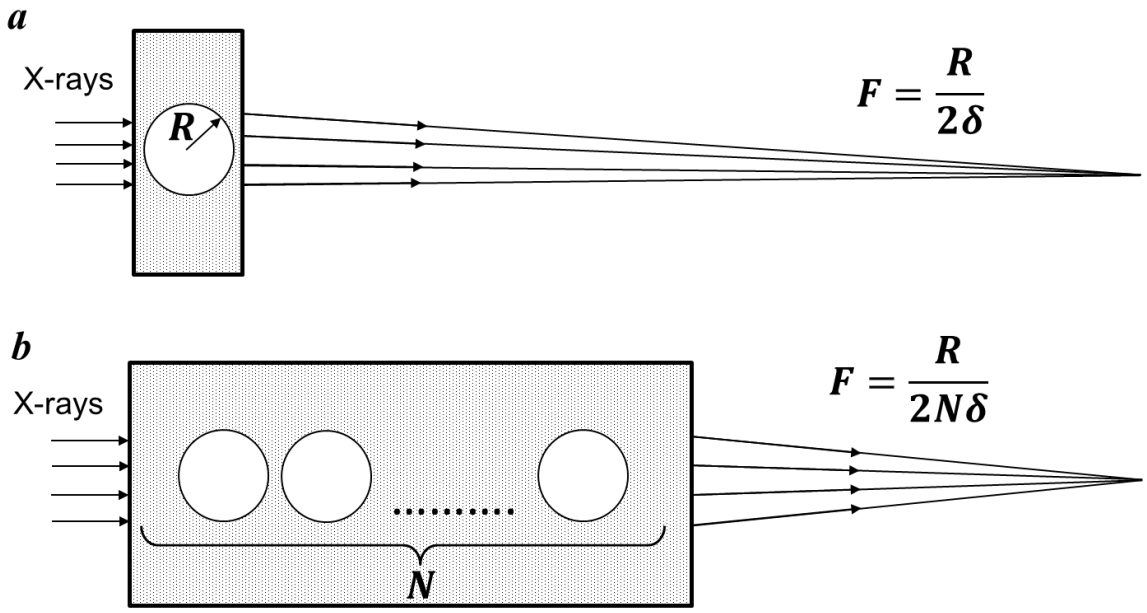

Fig. 22. Illustration of the basic principle of CRL focusing: the focal distance decreases with the increase of the number of "hole-lenses".

The optimal radius of curvature for the majority of lenses of on the order of hundreds of microns, and lens materials have a low atomic number (aluminum, beryllium, carbon). For example, 10 beryllium lenses with 50 um radii of curvature have a focal distance 1 m for X-

rays with wavelength 1 Å. Another important lens parameter is the length between apexes of paraboloids which determines absorption in the lens.

To characterize the efficiency of lenses, the two parameters have been introduced: the effective aperture A_{eff} and the diffraction limit σ[34]. The effective aperture defines a part of the physical aperture, which focuses the radiation. The diffraction limit determines the minimum achievable focal spot at the point source of radiation.

Thickness of the lens can be often neglected. The approximation of a thin lens may be applied:

$$A_{eff} = 0.707\sqrt{\frac{\lambda F}{\gamma}} \qquad \sigma = 0.47\,\frac{\lambda F}{A_{eff}} \tag{11}$$

where λ is the wavelength, F is the lens focal length, $\gamma=\beta/\delta$ is the parameter which determines refractive properties of lenses.

As for the visible optics, CRL are subjected to various aberrations. Sensitivity to the imperfections of the lenses becomes essential especially in coherent X-ray illumination. According to the our experimental study, the main technological parameters which determine the aberration degree are uniformity of the lens material and perfection of CRL surface profile.

Currently, refractive X-ray optics is widely used as a primary optics in microscopy applications where CRL is used as the condenser and the collimator of the X-rays.

The figure 23 shows an example of the influence of lens aberrations on the image quality of Siemens Star (the special etalon is usually employed to test the resolution of optical instruments).

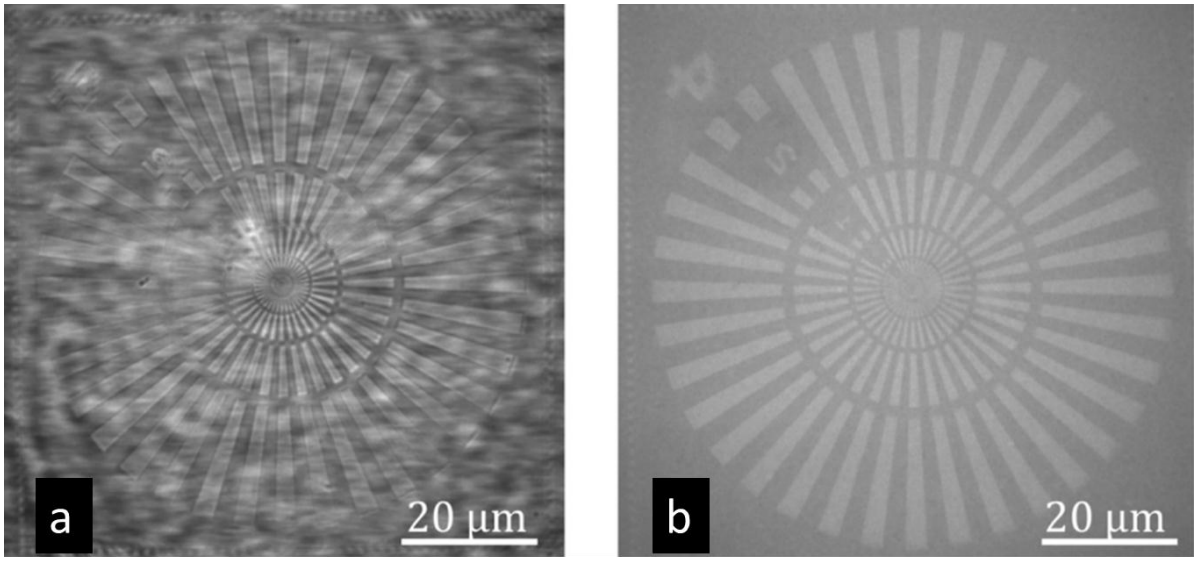

Fig. 23. The aberrated image of Siemens star(a) and not aberrated(b)(the images taken from [35])

The main advantages of CRL are as follows:

- Wide working energy range: from 2 KeV to 100 KeV.
- Possibility to vary focal length from 10 mm to dozens of meters.
- Possibility to control the focal spot from 10 nm to 100 µm.
- In-line geometry, which simplifies the arrangement of elements in the experiment.

As a result, CRL is a simple, convenient and effective X-ray optics for a wide range of research tasks. Due to the creation of transfocator [36, 37](a special device for focal distance) CRL become a versatile instrument at optics hutches and at the front end.

The number of lenses in the transfocator varies by means of the making use or removal of cartridges filled with a different number of lenses. In order to be able to use the maximum possible focal lengths the geometric progression algorithm of filling cartridges is used. This strategy allows to apply transfocator for the maximal energy range, which employs at synchrotron station (*Fig. 24*).

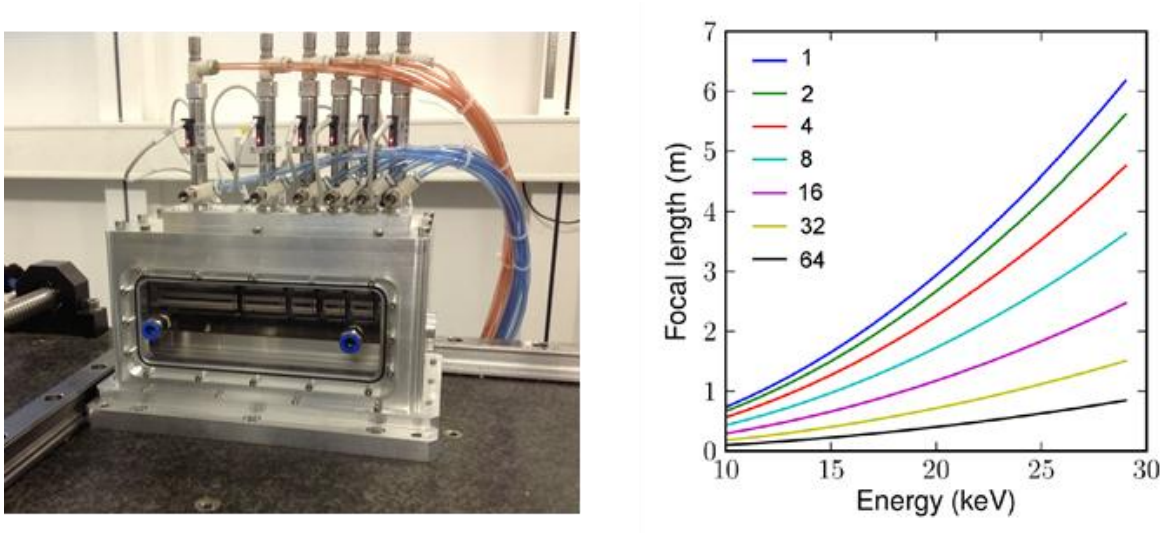

Fig. 24. The photo of a compact transfocator which is based on pneumatic actuators (left image) and the graph of the possible focal lengths for transfocator at different energies (right image).

Parabolic CRL (*Fig. 25*) are the best candidate for the purposes of this research due to the fine focusing and due to the image transition with a low aberration rate.

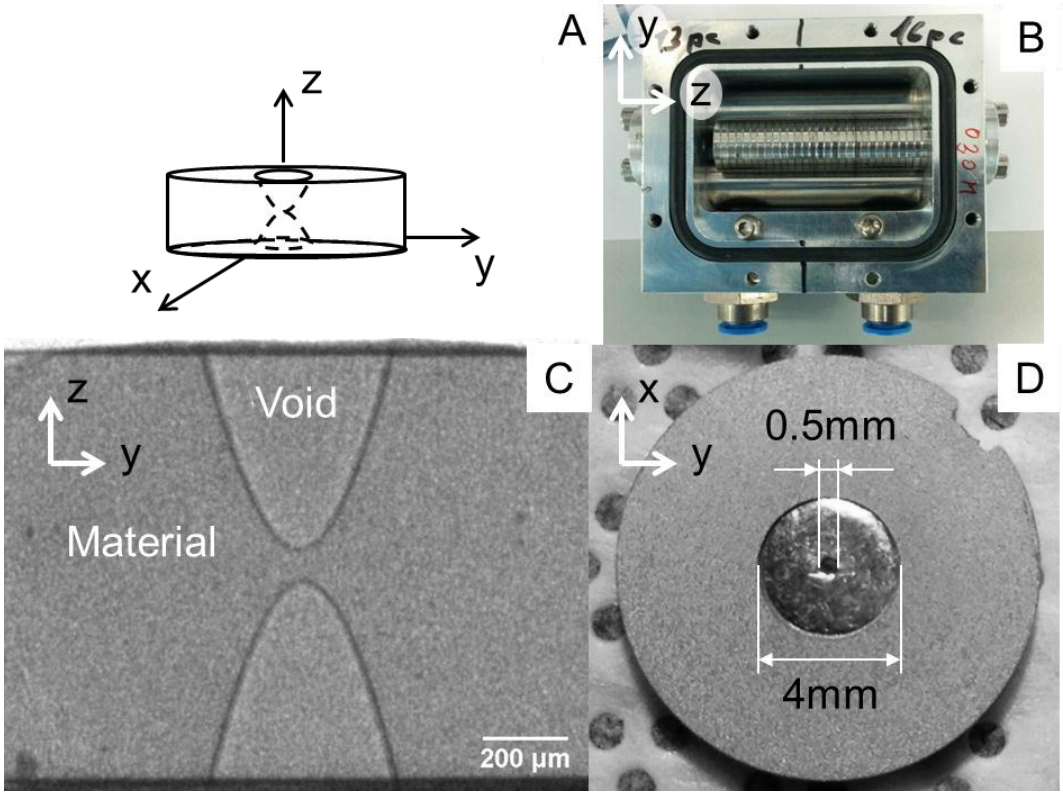

Fig. 25. Parabolic CRL: A. Orientation of views; B. CRL holder with lenses; C. X-ray microscopy image of one parabolic refractive lens; D. Photo of one parabolic refractive lens.

1.5. Basics of Fourier optics

The laws of refraction, reflection, diffraction, and interference are common for all electromagnetic waves. They differ in the ways they interact with the matter and, consequently, in constants and indexes.

In the visible spectrum of electromagnetic radiation, the theory of conversions with the help of optical devices (Fourier optics) [38] is highly developed. As it is known, the Fourier transform (FT) of incident on the lens light wavefront exists at the lens' back focal plane (*Fig. 26*).

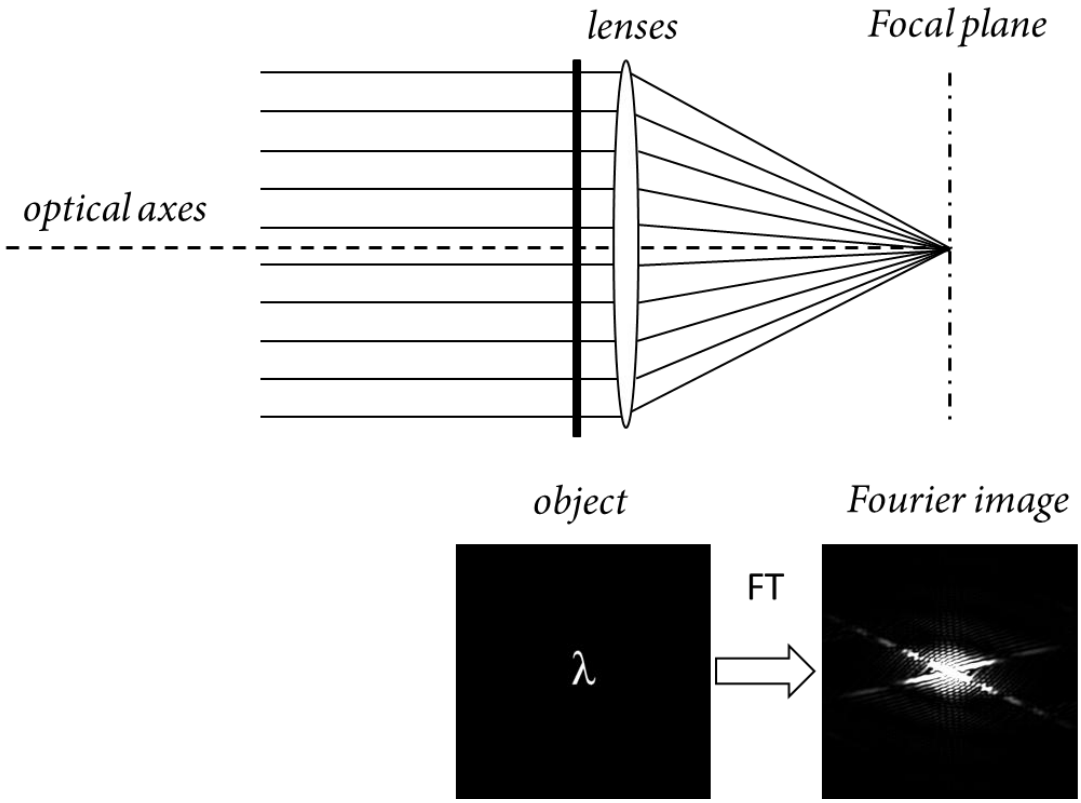

Fig. 26. Fourier transforms of lenses (LFT). The object forms the intensity distribution which is converted by lenses into a Fourier image of an object at lenses back focal plane.

LFT operation is described in more detail in Chapter 3.1.

In the X-ray region, the possibility of FT has been considered theoretically[11] and experimentally[4]. For today, CRL FT is used as one of the powerful methods of a photonic crystal investigation and study [1, 13, 39]. This optical method makes it possible to determine the photonic crystals' symmetry and period quickly.

CRL FT was used to analyse standing acoustic waves on a crystal surface at Bragg geometry [40].

In this thesis, CRL FT in Bragg geometry is proposed as a new X-ray optical method of the semiconductor micro- and nano-structures X-ray diffractometry.

X-ray diffractometry and reflectometry

2.1. Bragg's law

The discovery of X-rays had led to the new phenomenon of X-ray diffraction. The Braggs [29, 41], father and son, proposed a theory to describe X-ray diffraction in crystals. They found that crystals are three-dimensional diffraction lattices, and that X-rays diffraction occurs due to their periodicity.

The diffraction leads to the appearance of maxima of intensity which satisfy the equality:

$$2dsin(\theta) = n\lambda, \tag{12}$$

where d is the interplanar spacing of the diffracting plane; θ is the angle of diffraction; λ is the X-ray wavelength; and n is integer representing the diffraction order.

The Bragg's equation is based on an evaluation of the optical path difference between the waves reflected from the upper and bottom crystalline planes (*Fig. 27*).

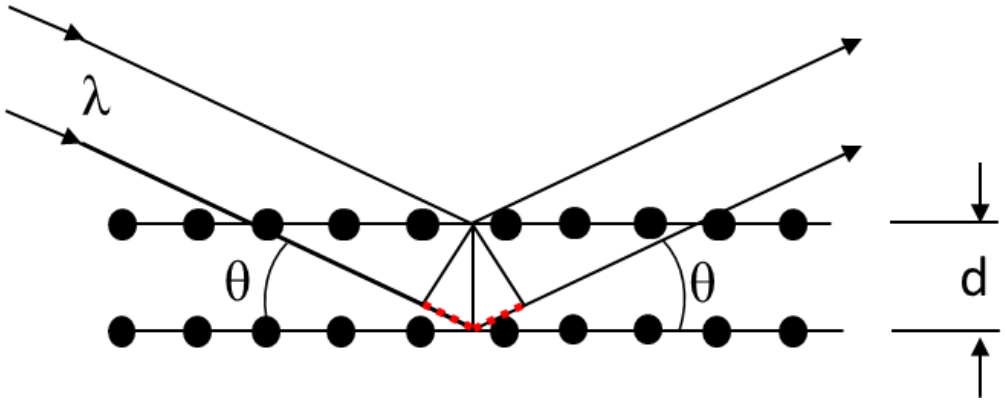

Fig. 27. The graph shows the optical path difference (marked with the red dots) between the waves reflected from the upper and bottom crystalline planes.

As a consequence, X-ray diffraction makes it possible to analyze crystal symmetry and to measure the distance between atom planes.

2.2. Reciprocal space

Max von Laue has developed the diffraction theory. He replaced diffraction angles and interplanar distances by incident and scattered vectors[42].

When the X-ray interference condition is satisfied, that means that we observe an interference order corresponding to the specific crystalline planes. We could construct a reciprocal space, which consist of all conditions of the X-ray diffraction, i.e. any possible diffraction will have its own place at the reciprocal space.

The relationship between primitive vectors of crystal **a**, **b**, **c** and corresponding reciprocal space with $\mathbf{Q_h}$, $\mathbf{Q_k}$, $\mathbf{Q_l}$ primitive vectors for a crystalline plane (h,k,l) is

$$\begin{aligned} \boldsymbol{a} \cdot \boldsymbol{Q_h} &= 2\pi h \\ \boldsymbol{b} \cdot \boldsymbol{Q_k} &= 2\pi k \\ \boldsymbol{c} \cdot \boldsymbol{Q_l} &= 2\pi l \end{aligned} \tag{13}$$

To describe the X-ray diffraction geometry the scattering vector $\mathbf{q}=\mathbf{k}_h-\mathbf{k}_0$ was introduced, where $\mathbf{k}_0$ is the incident beam vector, and $\mathbf{k}_h$ is the scattered beam vector.

When the reciprocal lattice vector $\mathbf{Q}_{hkl}=h\mathbf{Q}_h+k\mathbf{Q}_k+l\mathbf{Q}_l$ becomes equal to X-ray scattering vector **q**, the Bragg's condition is satisfied (*Fig. 28*).

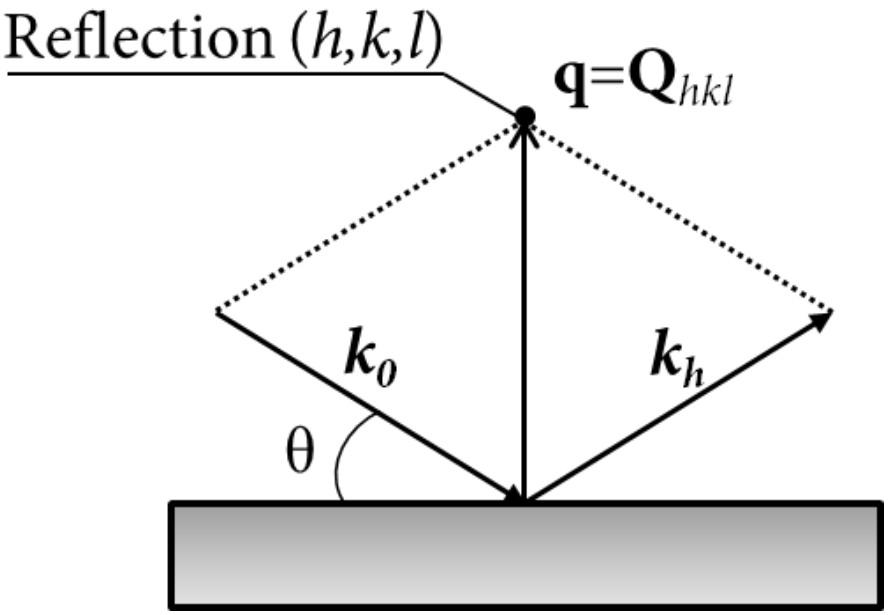

Fig. 28. The Bragg's geometry of X-ray diffraction. The scattering vector is equal to the reciprocal lattice vector.

The three-dimensional atomic periodical ordering in a crystal forms a periodical three-dimensional reciprocal space. In the experiment, if we fix the incident and scattered beam vectors $k=2\pi/\lambda$ by use of monochromatization and precise positioning of an object and detector, we can measure the scattering vector $q=4\pi\cdot\sin\theta/\lambda$ precisely. The interrelation between atomic plane (h,k,l) distances d_{hkl} and reciprocal vector $\mathbf{Q}_{hkl}$ is

$$d_{hkl} = \frac{2\pi}{Q_{hkl}} \tag{14}$$

In a diffraction experiment we cannot observe all the reciprocal space, we are limited by wave vector module $k_0=k_h=2\pi/\lambda$. The sphere of observation is called the Ewald sphere named after Paul Peter Ewald [43, 44] who first proposed using a sphere for the interpretation of diffraction experiments (*Fig. 29*). There may occur conditions under which either the incident beam is below the crystal surface or the exit beam is.

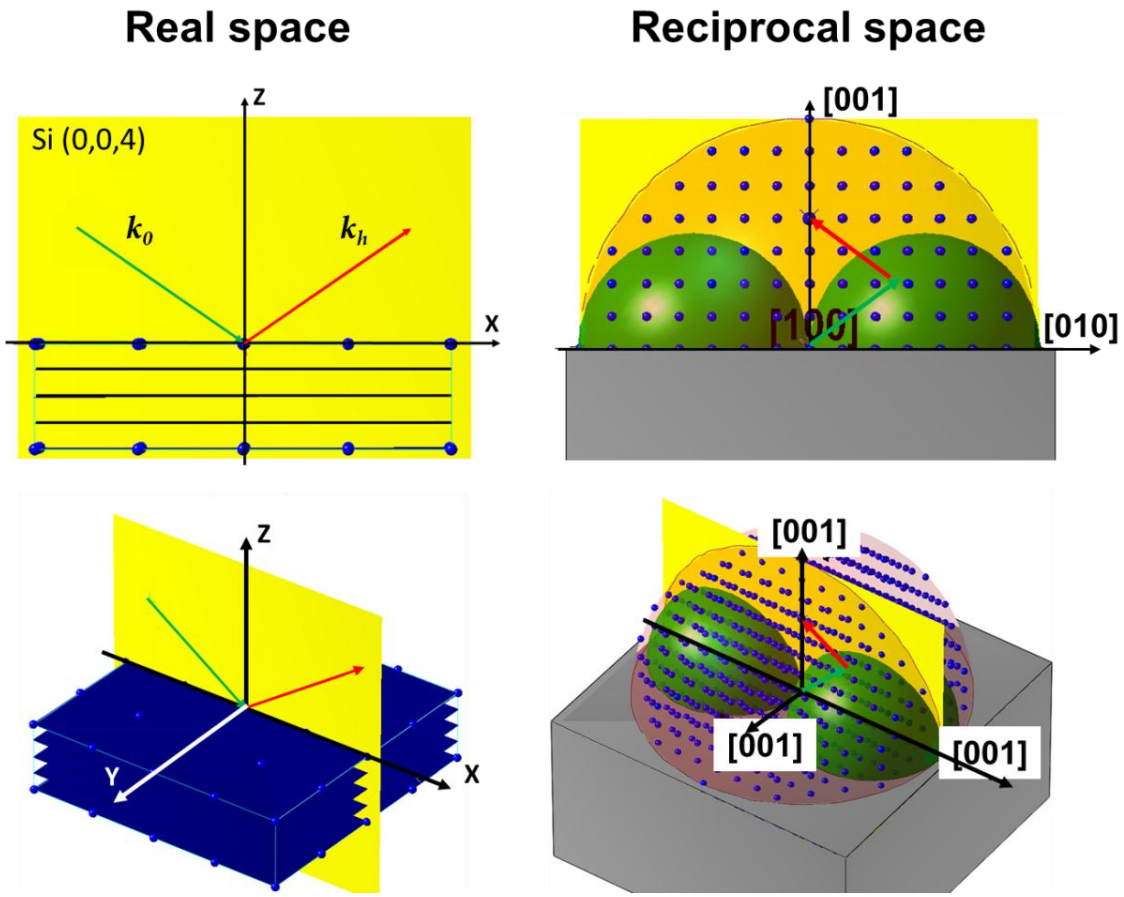

Fig. 29. Real space and reciprocal spaces of X-ray diffraction experiment for Silica. The observed crystal plane is (0,0,4). Yellow color indicates a diffraction plane; a pink half- sphere is the Ewald sphere; two green spheres are: incident beam below surface (left) and exit beam bellow surface (right).

The aim of HRXRD is a precise study of reciprocal space and the interpretation of results in a real space. Any defects, nano- and micro-structuring change the diffraction conditions and distort the Bragg reflection.

2.3. Traditional methods of a high-resolution X-ray diffractometry and reflectometry

High Resolution X-ray Diffractometry

Resolution in a reciprocal space is determined by the accuracy of detecting of Bragg's reflections. A special type of an X-ray diffraction experiments focused on improving the resolution is High Resolution X-ray Diffractometry (HRXRD)[45, 46].

All HRXRD experiments involve the following**:**

- An X-ray source. Currently, laboratory diffractometers equipped with conventional sealed X-ray tubes are widely used.
- A beam conditioner. The aims of beam conditioning are to collimate and monochromatize an X-ray beam. Usually, two - or four-fold ideal crystals are used as beam conditioners. Curved X-ray mirrors are also the part of a beam conditioner.
- A precise Goniometer. This mechanical device gives the opportunity to a relative rotation of an X-ray source, the studied crystal and detection system.
- A Beam Analyzer which ensures the precise analysis of directions of an X-ray beam scattering. In order to meet the requirements for resolution, we use ideal crystals as a Beam analyzer (triple crystal concept); to meet the requirements of sensitivity, slits (double crystal concept) are used.
- An X-ray Detector. Due to its high dynamical range and high sensitivity, scintillator detector-counter is currently the most wide-spread instrument for HRXRD.

When HRXRD experiments require high X-ray intensity instead of resolution, the double crystal concept is used. The triple crystal diffractometry (*Fig. 30*) is used for the high resolution, but not the X-ray intensity.

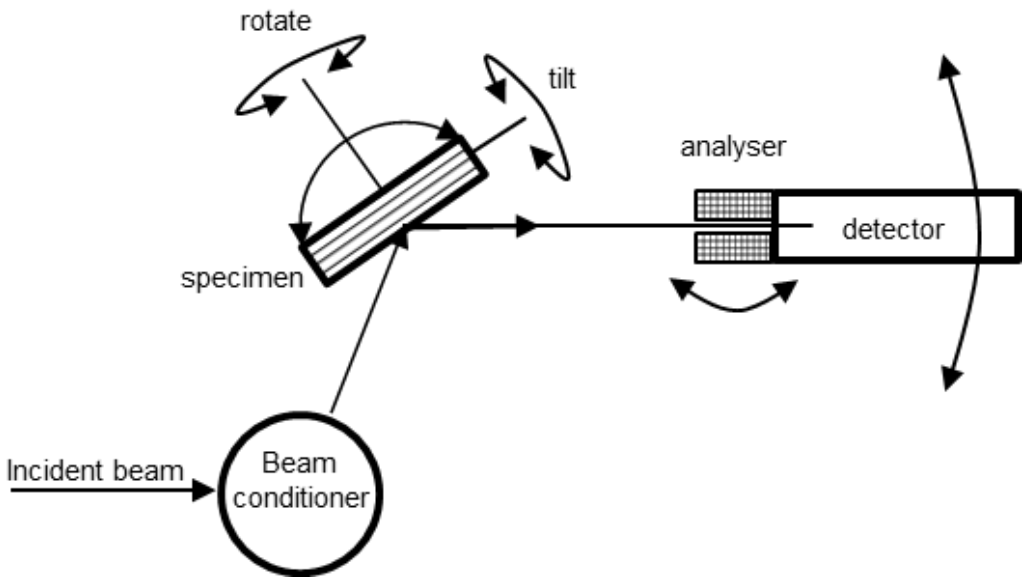

Fig. 30. Triple crystal diffractometers experimental scheme. The most precise analysis of X-rays diffraction.

The main requirements and problems of triple crystal diffractometry are:

- requirements of precision and stable mechanics;
- the scanning procedure should be time-consuming;
- problems with *in situ* experiments and dynamics observation;
- low analysis locality, that is up to tens of millimeters.

The lack of the "old generation" experiments is averaging over time and space (that will be described below)**.** The main claims to the new generation of HRXRD methods consist in providing a possibility to perform *in situ* experiments with high analysis localization – micro-HRXRD analysis.

There are three reciprocal space scanning options usable in HRXRD: rocking curve (ω scan), ω-2θ scan and 2θ scan (*Fig. 31*). The different regions of reciprocal space could be recorded according to type of the scan. Due to the finite incoming X-ray beam monochromatization level, presence of divergence, crystal-analyzer type, scans at reciprocal space have an instruments artefact. Mathematically this influence is described by the instrumental function.

CTR is intensity profile between RLP along q_z direction which correspond to presence of surface.

Monochromator streak is corresponding to the limited monochromator beam collimation and monochromatization level. It is affects on a FWHM of rocking curve. As an example,

for Si (002) rocking curve FWHM is 61 urad at Ge (022)x4 symmetric monochromator while monochromatization by Ge (044)x4 symmetric monochromator provides Si (002) rocking curve FWHM 26 μrad. As a result of monochromatization, the intensity decreases 30 times.

Analyser streak is corresponds to the energy and angular band pass of crystal-analyzer.

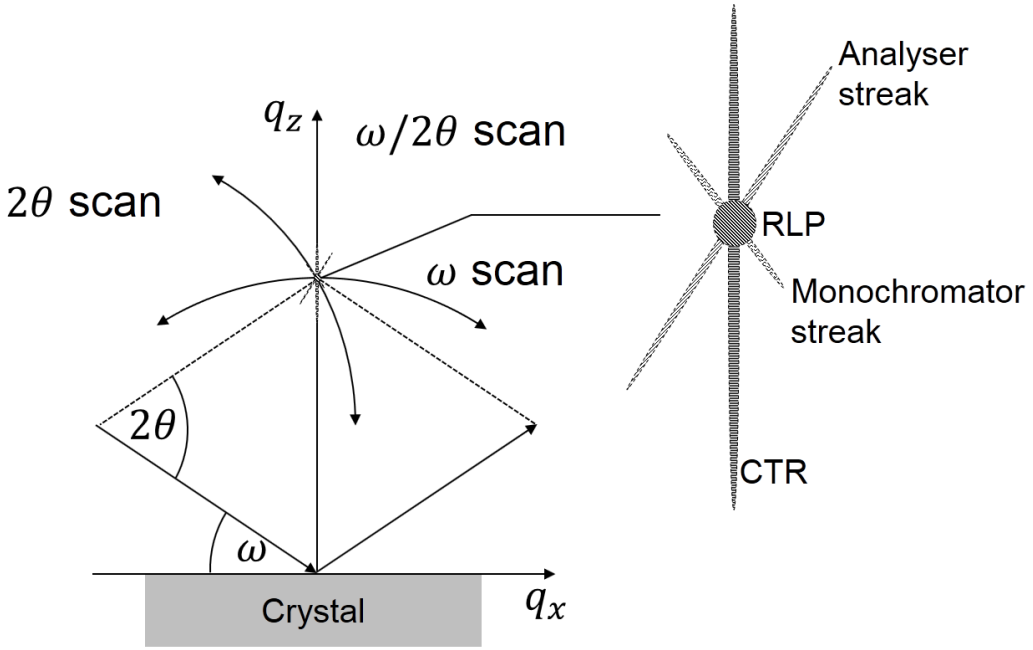

Fig. 31. The types of scan at reciprocal space and HRXRD instrument influence on a recorded reciprocal space

During analysis of rocking curves, it is possible to make conclusions about defects in the crystal such as a mosaic, twinning and dislocations. The main objectives of the experiment are to determine contribution of the instrument and of the structure under study to the diffraction peak.

HXRD becomes popular as an instrument of epitaxial film and crystal coverage investigation. It gives possibility to study lattices mismatch between layer and substrate, induced stresses, relaxation process, crystal structure of thin film on a surface and on inside interfaces (for complex multilayers) with high accuracy $\Delta d/d \sim 10^{-4}$ (where d is interplanar distance, Δd is minimal deviation of interplanar distance which is possible to detect).

For HRXRD investigation, the common practical recommendations exist and they are very useful due to the ability to provide a quick analyse without complex calculations.

Beside conventional rocking curve analyse and theta-2theta scans, the Reciprocal Space Mapping (RSM) approach is developed. The RSM is the cross-section of reciprocal space which recorded by sequential sample and detector rotation. The RSM provides information about in-plane and out-plane crystal perfection.

With the introduction of the X-ray camera, the RSM became much more easy and quick. As a result, the 3D reciprocal space reconstructions became applicable which provide information about crystal structure at three dimensions.

Also HRXRD method is sensitive to surface relief of a studied structure[47]. The satellites near Bragg reflection are formed in q_y and q_x directions (*Fig. 32*) at the reciprocal space for a periodical profiled crystal.

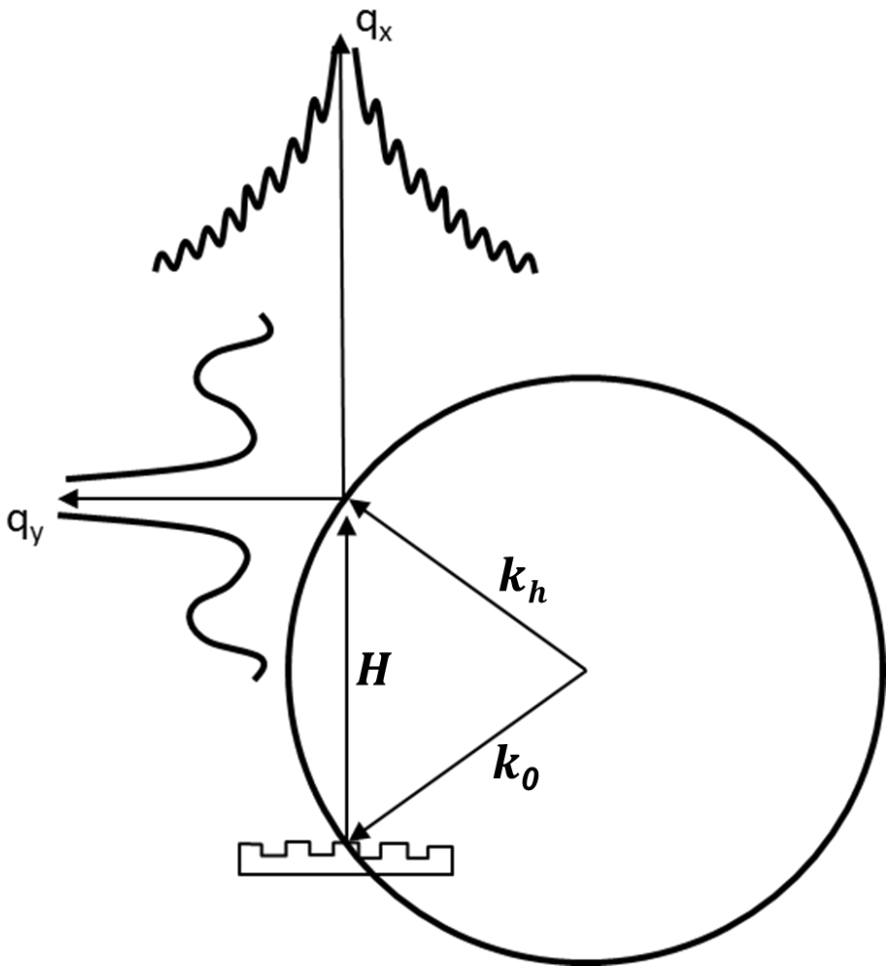

Fig. 32. The intensity distribution near Bragg reflection in q_x and q_y directions for periodical profiled crystals (adapted from [48])

An important requirement is the selection of the optimum X-ray optical elements to minimize the contribution of the instrument in the rocking curve.

High Resolution X-ray Reflectometry

The task of XRR is to observe and to analyze the reflection of X-rays on a surface[46, 49]. The main phenomena under analysis are externally total reflection and X-rays interference on thin films.

The Helmholtz equation defines X-rays propagation through the medium with refractive index n(x,y,z):

$$\Delta E(x,y,z) + k^2 n^2(x,y,z) E(x,y,z) = 0 \tag{15}$$

where $E(x,y,z)$ is electric field intensity, $k^2=\omega^2/c^2$ is the square modulus of the wave vector.

The main parameter defining surface reflectivity is refractive index $n(x,y,z)$ which depends on the electron density of the surface material (*Fig. 33*).

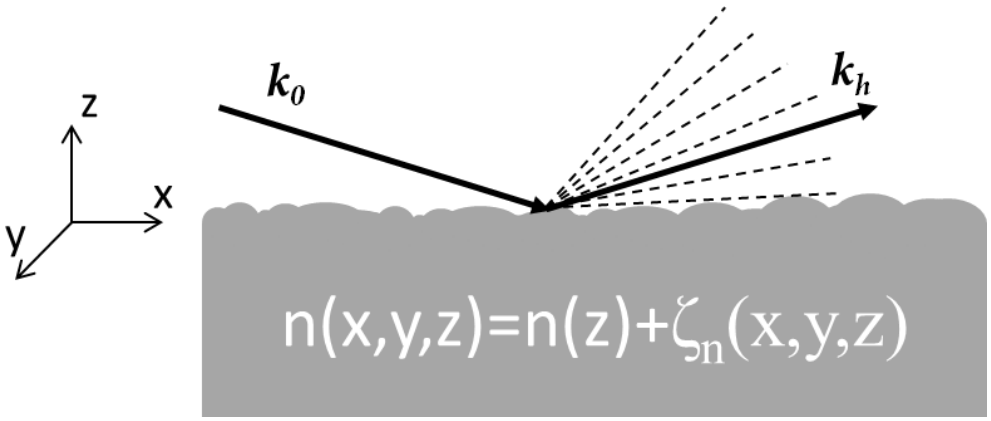

Fig. 33. X-ray surface reflection. Two parts of reflection are shown: the specular part (n(z)) and the diffuse part (ζn(x,y,z)) caused by the roughness of the surface.

For X-rays, the decrement of refraction index $\delta(x,y,z)$ plays the main role, which is determined as:

$$\delta = \frac{2\pi\rho r_0}{k^2} \tag{16}$$

where ρ is the electron density, r_0 is the scattering amplitude per electron. Under same conditions the wave doesn't penetrate the matter at low glancing angles but reflects from the surface. This phenomenon is called the total external reflection. The critical angle $\alpha=\alpha_c$ for the total external reflection is

$$\alpha_c = \sqrt{2\delta} = \frac{\sqrt{4\pi\rho r_0}}{k} \tag{17}$$

Usually, for any medium, α_c is of order 5 mrad and δ is of order 10^{-6}.

The main task of XRR is to restore electron density profile $\rho(z)$ according to the depth z. It is possible to observe interference of X-rays and to detect series of maxima and minima – Kiessig fringes, when a thin film (0.1 nm – 100 nm) is present on the surface (*Fig. 34).* The equation that describes these phenomena is the same as Bragg's equation, with the only difference that d is the film thickness instead of the atoms interplanar spacing.

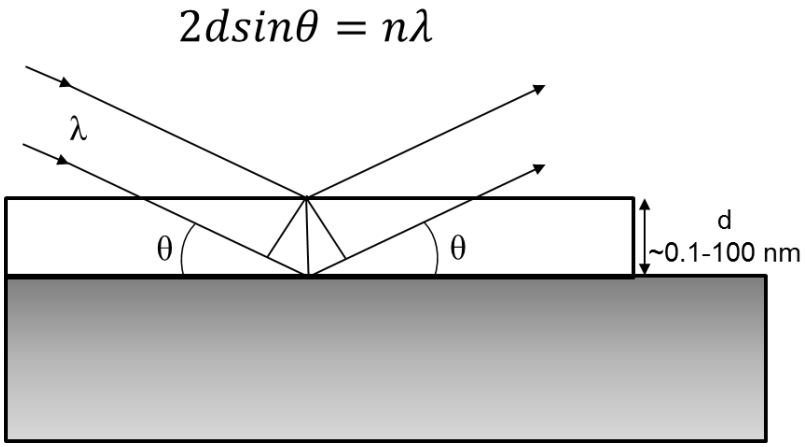

Fig. 34. The graph shows the optical path difference between the waves reflected from the upper and bottom boundaries of the film.

In order to observe and to analyze the total reflection and Kiessig fringes, special experimental setups similar to the HRXRD diffractometers were used.

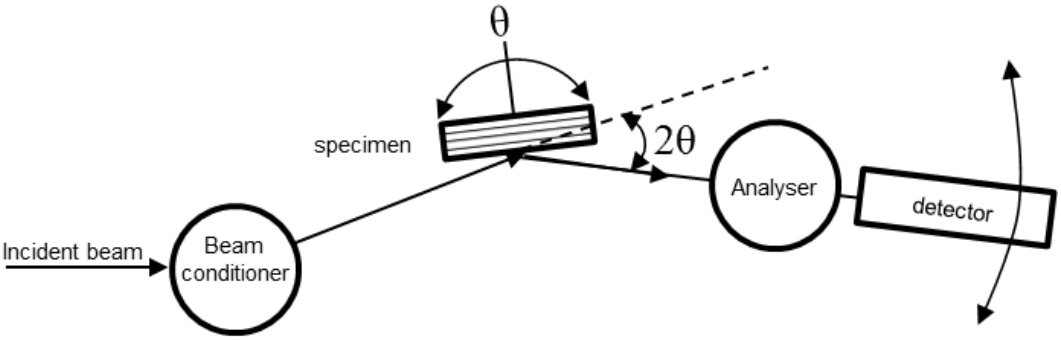

Fig. 35. The XRR setup. Typically, the θ-2θ intensity curve is analyzed by way of simultaneous rotation of specimen (θ angle) and detection system (2θ angle).

By simultaneous rotation of the detector and the surface of the film is carried scanning along q_x direction where Kiessig fringes are observed (*Fig. 35, 36*). By rotation exclusively of the detector is carried scanning along q_y direction where specular reflection is observed.

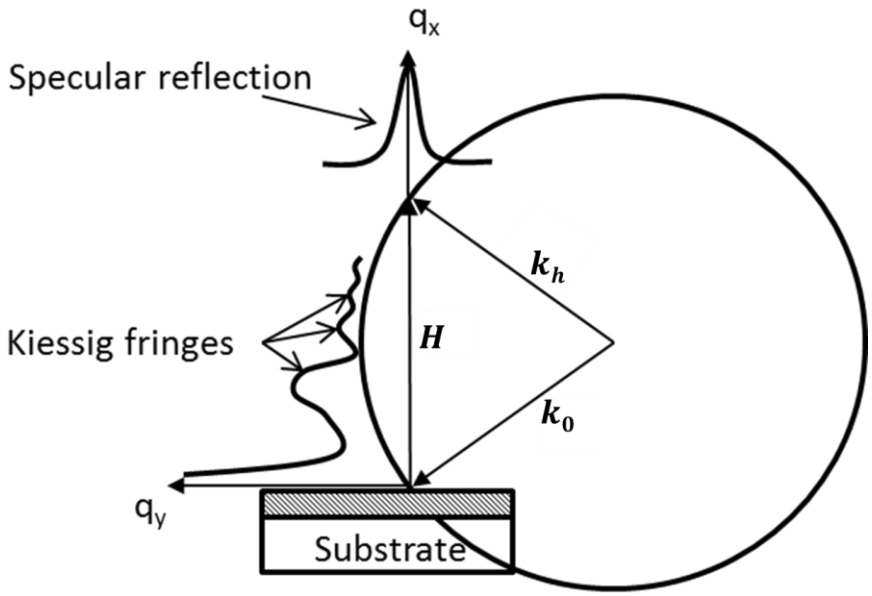

Fig. 36. The intensity distribution near (000) reciprocal point at the XRR experiment.

The period of Kiessig fringes is decrease when film thickness is increase (*Fig. 37*). The surface roughness change the number of observable Kiessig fringes and also decrease the specular reflection intensity.

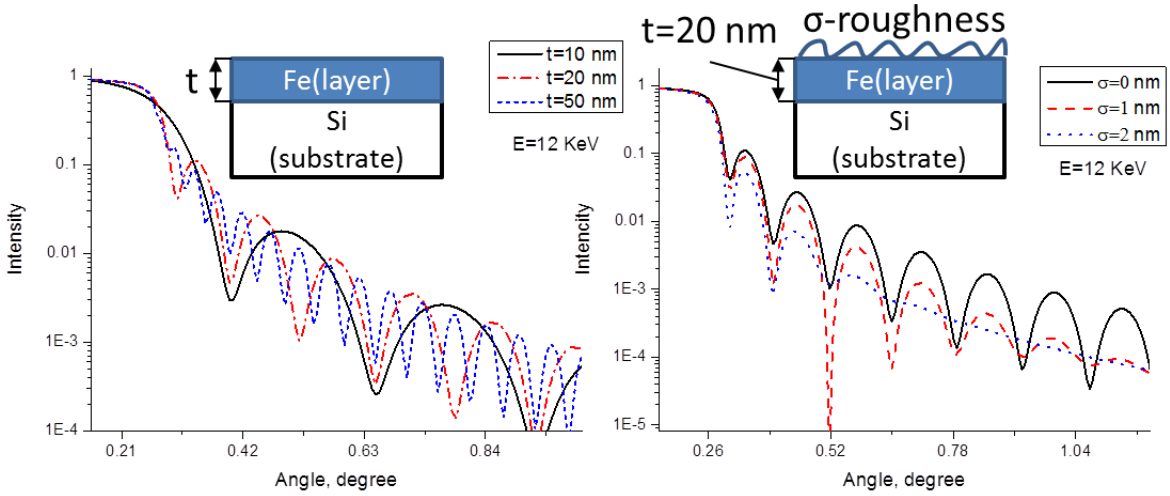

Fig. 37. XRR curves for different Fe layer thickness and surface roughness on silicon substrate.

Completely solved reflectometry task consists in the reconstructed density distribution profile in the layers along the surface normal. It is usually assumed that the solution is exact, if the standard deviation of the model and the experimental curve is minimal. However, it is necessary to provide extra measurements by other methods to minimize the probability of an interpretation error.

Both HRXRD and XRR techniques are used to analyze the average time and space characteristics, and they require further modernization and revision.

X-ray optical approach for high resolution diffractometry and reflectometry

3.1. Fourier transform high resolution diffractometry based on refractive optics

We tailored the theory of visible light Fourier transform to the cases of X-rays and Bragg diffraction. The main equations and relations are presented at this paragraph. Also, the simple phase-contrast object in the form of a binary square-wave phase grating and it Fourier transform are discussed.

Conventional triple crystal diffractometry technique is used to observe crystal's reciprocal space near the Bragg reflection with the help of additional crystal-analyser. Mathematically, this is described by a convolution operation of the reflection function of the analyzed crystal $R_x(\lambda,\theta)$ and crystal-analyser $R_A(\lambda,\theta)$[45]:

$$I(\theta) = \int_{\lambda_1}^{\lambda_2} I_0(\lambda) R_x(\lambda,\theta) R_A(\lambda,\theta) d\lambda \tag{18}$$

where $I(\theta)$ is the detected X-ray intensity, $I_0(\lambda)$ is the intensity of incident X-rays on the analyzed crystal, and λ is the X-ray wavelength.

Another approach is to perform the FT with X-ray optics. Similar to triple crystal concept, this method is also described mathematically as an integral transformation[38]. Let us assume that A is the amplitude of incident on an object wave λ; $t(x)$ is object transmittance function and the amplitude after the object $U(x)=A\cdot t(x)$. There are three options of lens arrangement: object placed before the lens, object placed in front of the lens and object placed behind the lens.

1) Object placed before the lens (*Fig. 38*). According to the theory of Fourier optics in the focal plane f we will observe the distribution of wave amplitude U(x) which satisfies the equation:

$$U(x) = \frac{A \cdot exp\left[i\frac{kx^2}{2f}\right]}{i\lambda f} \int_{-\infty}^{\infty} t(\chi) \cdot \exp\left[-i\frac{2\pi}{\lambda f}\chi x\right] d\chi \tag{19}$$

where A is the amplitude of the incident wave with wavelength λ, i is the imaginary unit. The FT is not complete due to the presence of the quadratic phase factor that stands by the integral.

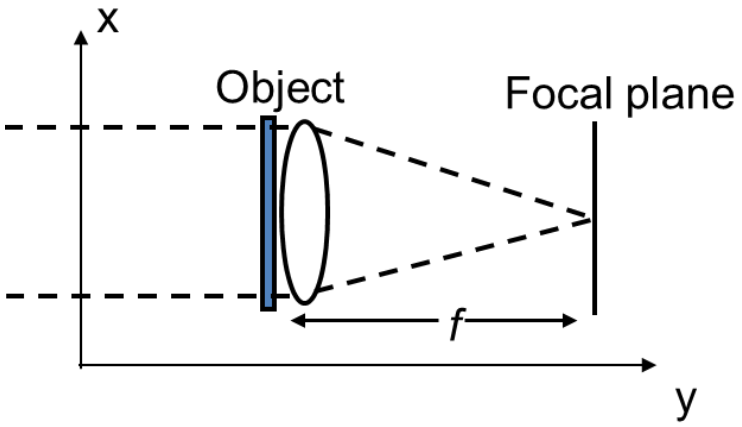

Fig. 38. Fourier transform operation with a lens. Object placed before the lens.

2) Object placed in front of the lens (*Fig. 39*). For this case the equation is converted into:

$$U(x) = \frac{A \cdot exp\left[i\frac{kx^2}{2f}(1-\frac{a}{f})\right]}{i\lambda f}\int_{-\infty}^{\infty} t(\chi)\cdot \exp\left[-i\frac{2\pi}{\lambda f}\chi x\right]d\chi \tag{20}$$

When the object is placed in the front focal plane of the lens ($a = f$), the phase curvature disappears, leaving the exact FT.

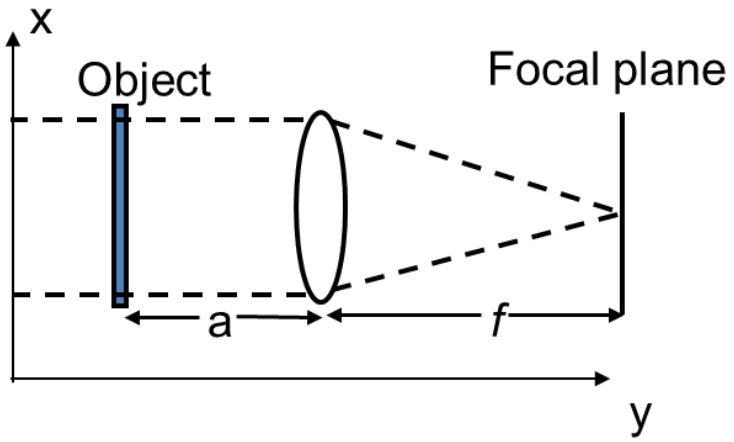

Fig. 39. Fourier transform operation with a lens. Object placed in front of the lens.

3) Object placed behind the lens (*Fig. 40*).

$$U(x) = \frac{Aexp\left[i\frac{kx^2}{2a}\right]}{i\lambda a}\frac{f}{a}\int_{-\infty}^{\infty} t(\chi)\exp\left[-i\frac{2\pi}{\lambda a}\chi x\right]d\chi \tag{21}$$

The scale of the FT depends on the distance *a* from the focal plane.

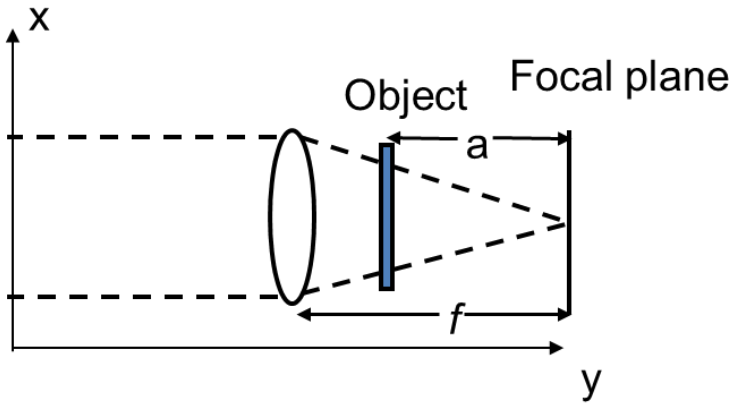

Fig. 40. Fourier transform operation with a lens. Object placed behind the lens.

These equations are correct if the source size is assumed to be negligible; however, in the case of synchrotrons or tubes the source size is finite, determining the resolution of the FT technique. For a finite source size the smallest X-ray spot is achievable at the imaging distance *b,* rather than at the focal plane. The focal distance *f*, source-lenses distance *a* and imaging distance *b* for CRL satisfies the thin lenses approximation[11]:

$$\frac{1}{f} = \frac{1}{a} + \frac{1}{b} \tag{22}$$

For example, on average, the ESRF X-ray source size is about 40 μm[22], the wavelength is λ=1Å, and Beryllium CRL stack is from 10 up to 50 lenses with curvature radius R_c= 50 μm, the relative mismatch between focal and imaging distances drops from 2.5% to 0.5 % (calculated at http://newton.phy.tu-dresden.de/applets/crlcalc.html) (*Fig.* 41).

So, for real X-ray sources the correction for the source size should be taken into account; LFT with highest resolution is achieved at the imaging distance *b,* rather than at focal plane.

Fourier optics theory was developing for in-line geometry. In this thesis, the FT optical approach applies to the Bragg geometry of a semiconductor crystal X-ray diffraction. It means that instead of the transmission function of the object t(x) we should consider the reflection function of the analyzed crystal $R_x(\lambda, \theta)$. As a result, the obtained Fourier patterns will depend on the incidence angle θ.

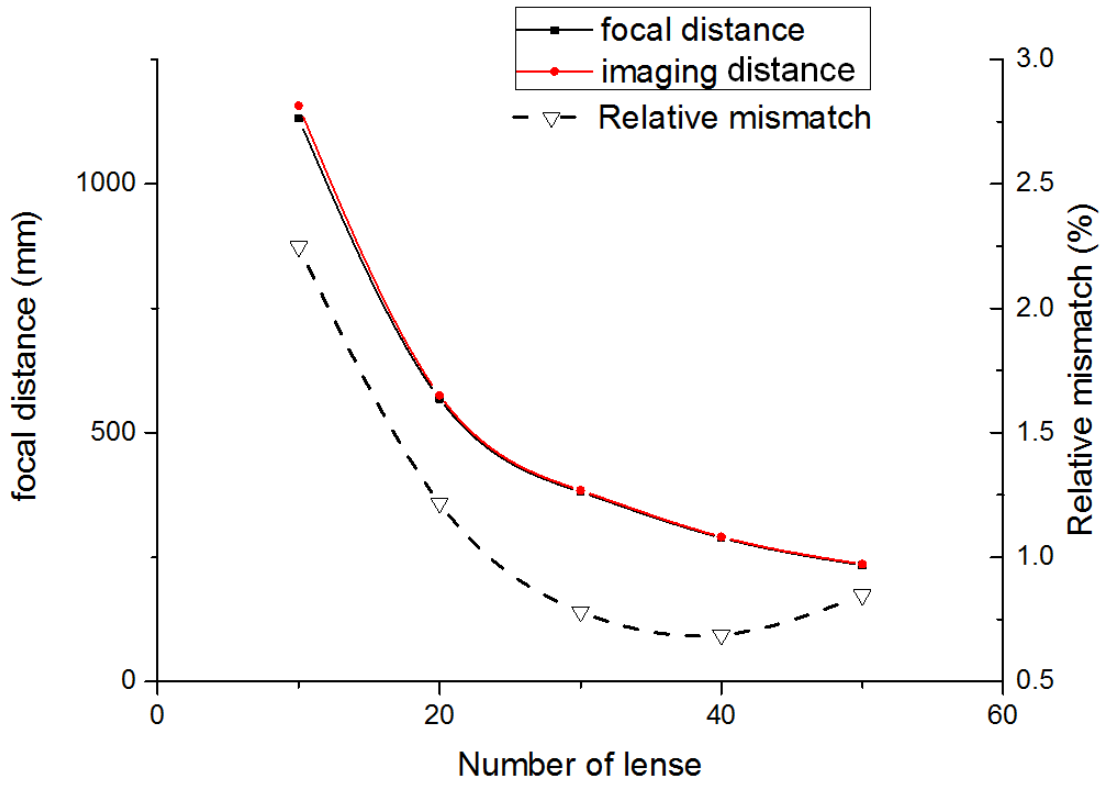

Fig. 41. Comparison of the imaging and focal distances for different amounts of lenses at 1Å of X-ray wavelength for Beryllium CRL with Rc=50 μm.

For the case when lenses are placed before the object, the equation should be replaced by the following one:

$$U(x,\theta) = \frac{A \cdot exp\left[i\frac{kx^2}{2a}\right]}{i\lambda a}\frac{f}{a}\int_{-\infty}^{\infty} R_x(\chi,\lambda,\theta)\cdot \exp\left[-i\frac{2\pi}{\lambda a}\chi x\right]d\chi \tag{23}$$

As for the Bragg's equation, due to the cone beam produced by the lenses instead of parallel beam, the conventional approaches will require modifications in diffraction equations. Due to the incident on an object cone beam at observation plane (at imaging or focal distance), there appear superposition of scattering vectors ($q_0 \pm \Delta q$):

$$(q_0 + \Delta q) = \frac{4\pi \sin(\theta_0 \pm \frac{\Delta\theta}{2})}{n\lambda} \tag{24}$$

where $\Delta\theta$ is the numerical aperture of the lens, θ_0 is the angle between optical axis of the lens and object's surface (*Fig. 42*).

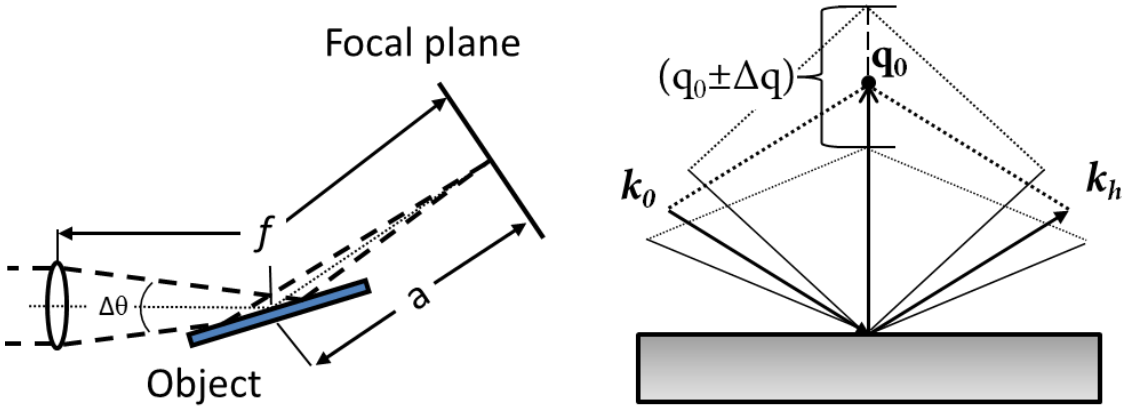

Fig. 42. LFT for Bragg geometry in real space (left) and in reciprocal space (right). The lens is located before the object.

When the lenses are behind the object, the wavefront is flat, and we observe a specific scattered vector q. In this case, lenses could limit the observable reciprocal space by their numerical aperture (*Fig. 43*). The equation for that case takes the form:

$$U(x,\theta) = \frac{A \cdot exp\left[i\frac{kx^2}{2f}\left(1-\frac{a}{f}\right)\right]}{i\lambda f}\int_{-\infty}^{\infty} R_A(\chi,\lambda,\theta)\cdot \exp\left[-i\frac{2\pi}{\lambda f}\chi x\right]d\chi \qquad (25)$$

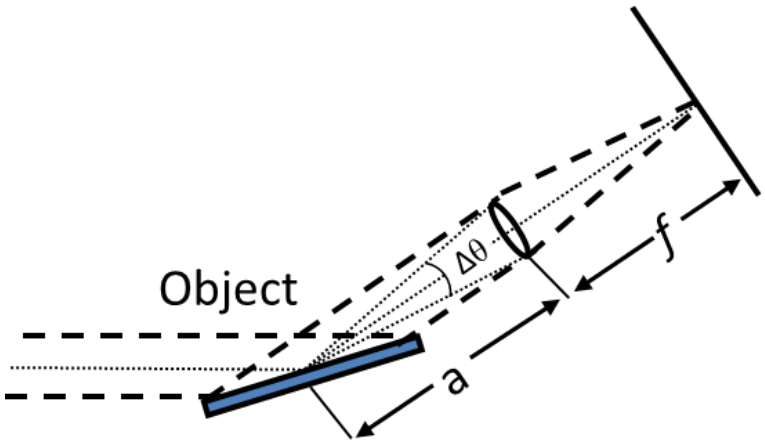

Fig. 43. LFT for Bragg geometry. Lenses behind the object.

The unique feature of the FT approach in Bragg geometry is the possibility to sweep reciprocal space. Apart from that, this approach is based on the classical principles of light optics, and together with new abilities of modern X-ray sources and refractive X-ray optics they are capable to enlarge the potential of HRXRD [50] experimenting.

Let us estimate the sensitivity of the FT technique and let us consider a simple phase-contrast object in the form of a binary square-wave phase grating with phase depth ϕ,

grating period Λ and line width b (Λ = 2b). Then the FT of such a binary square-wave phase grating is

$$F(q) = \frac{1}{2}\frac{\sin(\pi bq)}{\pi bq}\,[\exp(i\pi bq) + \exp(i\phi)\exp(-i\pi bq)] \tag{26}$$

The maximum values of *F(q)* are achieved at q = m/Λ and correspond to the diffraction orders m = 0, ±1, ±2, ±3, ... It should be noted that for a very small value of phase depth there should be a strong zero-order maximum and less pronounced odd-order maxima with the following values:

$$F(q)|_{q=m/\Lambda, m=\pm1,\pm3,\ldots} = \frac{1}{2}\frac{\sin(m\pi/2)}{m\pi/2}\,[isin(m\pi/2)][1-\exp(i\phi)] \tag{27}$$

From equation (27) it follows that the intensities of odd-order maxima are proportional to the square of the phase depth ϕ:

$$F(q)|_{q=m/\Lambda, m=\pm1,\pm3,\ldots} \cong \phi^2, \tag{28}$$

and therefore, the maximum contrast C is

$$C \cong \phi^2/\pi^2. \tag{29}$$

For example, for the contrast C = 5% the corresponding minimum phase depth ϕ= 0.22π. From equation (29) it is possible to estimate the minimal mean value of the deformation Δd/d for the binary grating made of a Si crystal with a periodically distorted crystal structure that can be resolved by the Fourier-transform technique. For example, in the case of the period Λ = 3.75 μm the minimal resolvable mean deformation is about $\Delta d/d \approx 10^{-5}$.

3.1.1. Concept of multifunctional X-ray microscopy

CRL already were applied as an X-ray objective for image formation and as a Fourier analyser of microradian X-ray diffraction on a submicrometer periodical structure - photon crystals.

The possibilities and functionality of the such X-ray microscopy are close to the electron microscopy which could operate in real image and reciprocal images regimes (*Fig. 44*). Due to the fact that X-rays highly penetrate through the matter, they provide more possibilities in solid matter study at different conditions.

As an example, Leonid Dubrovinsky and Natalia Dubrovinskaia published article[51] where the matter was studied by an X-ray microscopy based on CRL at high pressure(about 1 TPa). I participated at these research as a specialist in X-ray microscopy.

Due to the possibility to quickly change focal distance CRL based X-ray microscopy could also operate at two regimes. The advantages of such microscopy are high working distances (from tenth cm to meters).
Besides the fact that today CRL X-ray microscopy are limited by spatial resolution (~100 nm), that microscopy gives possibility to study of respectively big samples with average sizes about cm and to look inside of the sample.

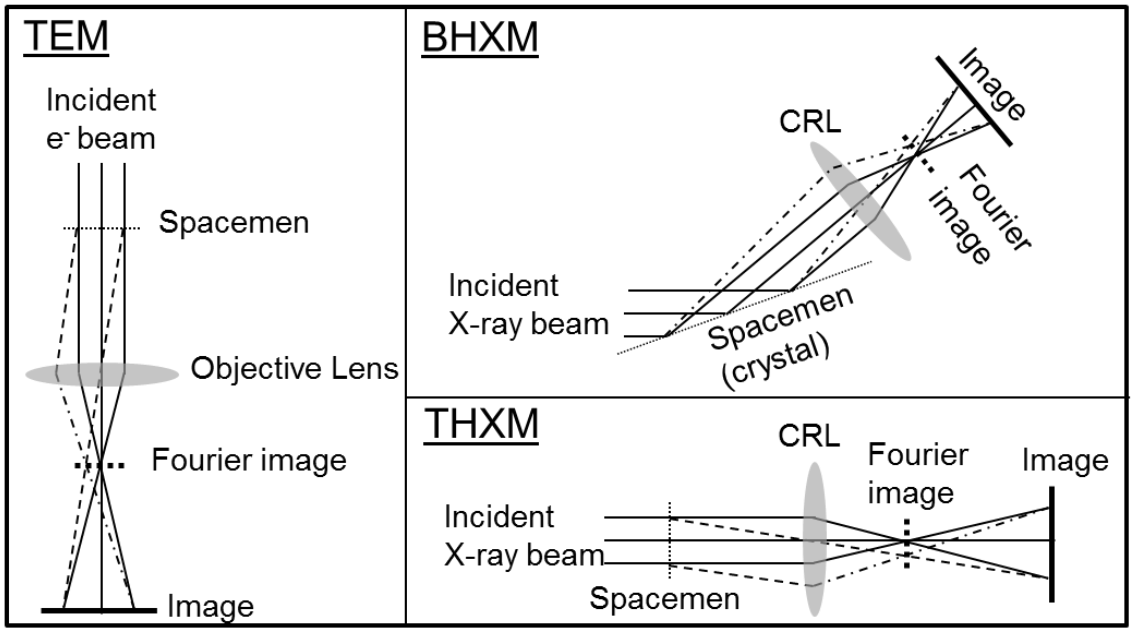

Fig. 44. The concepts of TEM - transmission electron microscopy, THXM - transmission High Resolution X-ray Microscopy, BHXM - Bragg High Resolution X-ray Microscopy.

At article [52] in situ observation of acoustic waves on a crystal surface by CRL Fourier method at Bragg geometry were published. At article[53] the concept of CRL based dark filed X-ray microscopy at Bragg geometry were declared and demonstrated.

The main feature of an X-ray microscopy at Bragg geometry is that image is stretched at one direction. But by image processing that feature could be compensated. The one of the main task of future CRL based multifunctional microscopy is development the low aberration rate lenses and translocators.

The Fourier regime at CRL based multifunctional microscope will be useful for express analyse of sample periodicity and symmetry of studied sample. Also, the Fourier regime could be useful for three-dimensional high resolution recording of crystals reciprocal spaces. This data could be highly improving the precision of the X-ray diffraction measurements and could be minimize possibility of wrong interpretation and conclusion.

3.2. X-ray reflecto-interferometry

Refractive optics for high energy X-rays has been successfully demonstrated [9] and is now mature and widely implemented. Similarly, to in-line optics, CRL make it possible to manipulate with beam divergence, and create a parallel beam. New types of interferometers based on refractive lenses have already been designed and implemented for X-ray beam characterization [21, 50, 54].

This thesis proposes a new approach to investigating X-ray reflectivity of thin films, on the basis of intensity front division interferometer - a Hard X-ray Reflecto-interferometer (HXRI).

It is well known, that a thin film can act as a wavefront splitter dividing a beam into parts, which can interfere with each other forming periodical fringes. In light optics, these fringes are called fringes of equal inclination[16]. These fringes are also found in the X-ray region and are called Kiessig fringes[55]. They are used in the XRR method for the evaluation of film thickness[56]. The fringes periodicity satisfies the equality $2d\sin\theta=n\lambda$, where d is the film thickness, θ is the angle of incidence, n is the integer which describes the interference order, and λ is the wavelength.

The concept of HXRI (*Fig. 45*) consists in the observation of the fringes of equal inclination at in the hard X-ray region with the help of CRL. The mechanism of the fringes formation consists in X-rays focusing on a film surface at angles near close to the total external reflection angle. Due to the interference between the rays reflected from upper and bottom film interfaces, a periodical pattern of bright and dark fringes forms inside the projected CRL numerical aperture($\Delta\theta$).

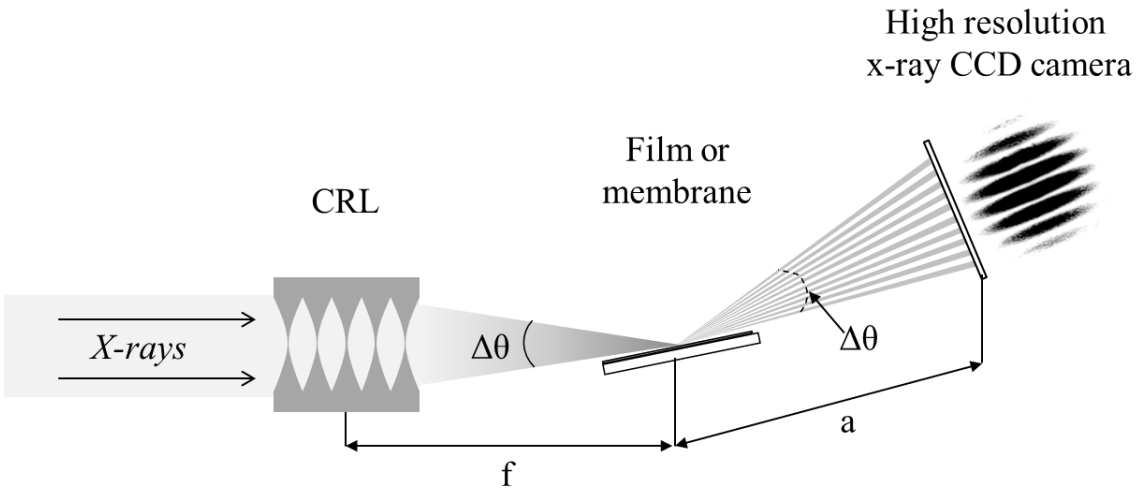

Fig. 45. The HXRI concept. X-ray cone beam produced by CRL placed on a film/membrane surface sweeps an interference pattern – Kiessig fringes.

The number of the observed fringes can be estimated by the following manner. By forming the cone beam we get several conditions for observing the maximum (*Fig. 46*):

$$\begin{aligned} 2dsin\theta_1 &= \lambda \\ &\vdots \\ 2dsin\theta_i &= i\lambda \\ &\vdots \\ 2dsin\theta_N &= N\lambda \end{aligned} \tag{30}$$

Also:

$$\theta_N - \theta_1 \leq \Delta\theta \tag{31}$$

Since the conditions of total external reflection are performed for small angles, we can assume that sinθ ~ θ (for the angle θ, measured in radians).

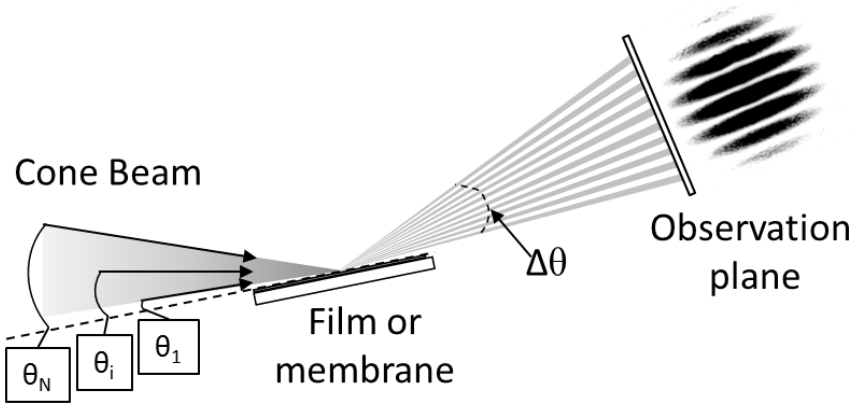

Fig. 46. Cone beam sweep interference pattern in one shot.

So, the number of the observed interference fringes is estimated by the equation:

$$N = \frac{2d}{\lambda} \cdot \Delta\theta, \tag{32}$$

where d is the membrane or film thickness, λ is the X-ray wavelength, $\Delta\theta$ is the CRL effective numerical aperture. By changing the number of lenses, it is possible to vary the CRL effective numerical aperture $\Delta\theta$, therefore, it is possible to vary the number of observed Kiessig fringes N. Making use of different the object-camera distances a, provideы a possibility to change the resolution of the observed reflection reciprocal space of membrane/film.

The angle resolution θ_{res} was determined by X-ray CCD camera pixel size r_{res} by equation:

$$\theta_{res} = \frac{r_{res}}{d} \tag{33}$$

where d is the object-camera distance (*Fig. 47*).

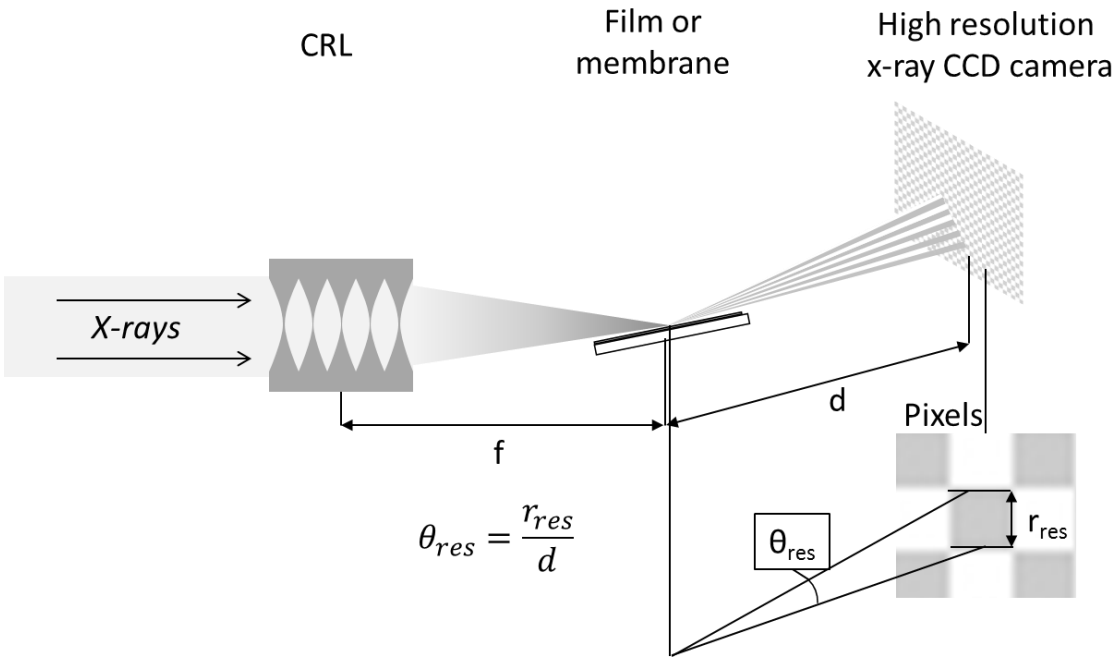

Fig. 47. HXRI experimental scheme and relation between angle resolution θ_{res} and pixel size rres.

The new X-ray optical approach in reflectometry could be useful in providing versatile instruments for thin films analysis and diagnostics. However, it should be taken into account that due to a high X-ray intensity, HXRI experiments can destroy the membrane/film.

Experimental Results

4.1. Experimental setup

All experiments were conducted on ID06 at European Synchrotron Radiation Facility (ESRF), Grenoble, France. The ID06 is a multipurpose undulator based beamline. Due to the high X-ray flux, small source size and relatively long beam path, this beamline ensures the X-ray beam with a high spatial coherence.

The beamline consists of three hutches: optics, experimental hutch 1 and experimental hutch 2. In the optics hutch, the white radiation from undulator is attenuated by metal foils-filters, collimated by slits, monochromated by nitrogen cooled Si-111 double crystal and pre-focused by transfocator filled by CRL (*Fig. 48*).

In experimental hutch 1, monochromatizated, collimated and attenuated X-ray beam is used for X-ray optical experiments. X-ray detector, ESRF-designed high resolution CCD camera "Sensicam" is used. Due to light optics, the "Sensicam" effective pixel size is 0.645 μm, which gives a spatial resolution of ~2 μm. For the X-ray optics test special Micro-optics Test Bench – MOTB[57] has been designed, which consists of an optical table and a system of motorized stages ensuring micro- and nano-sized precisions of movement.

The 40 μm undulator source size (in a vertical direction) and 60 m optical path have allowed us to achieve micro-focusing with the help of CRL and, as a result, they have enabled the development of high-resolution X-ray optical methods. Liquid nitrogen was applied to cool the Si-111 double crystal, a fixed exit monochromator was used to adjust X-ray energy in the range from 10 KeV to 20 KeV. For focusing, parabolic beryllium CRL with curvature radius R=50 μm was used as a more efficient X-ray optic in the chosen X-ray spectra.

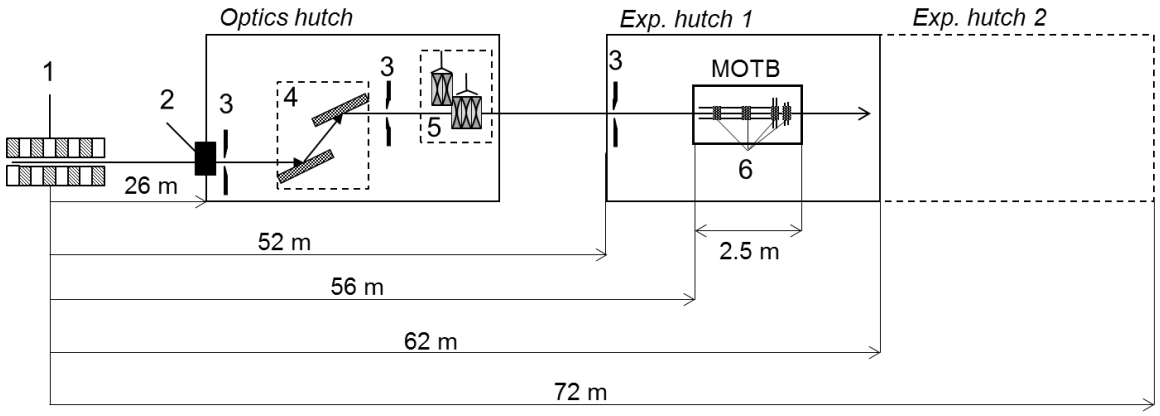

Fig. 48. ID06 beamline layout: 1. undulator X-ray source; 2. front end; 3. slits; 4. Si-111 double crystal, fixed exit monochromators; 5. transfocator; 6. system of motorized stages for an alignment.

4.2. Study of silicon micro-structures by CRL Fourier transform method

We studied two silicon microstructures [12]: the SiO_2 lattice deposited on silicon and profiled silicon lattice with periods of Λ=3.75 microns (Fig. 49). The profiled silicon lattice represents an one-dimensional binary grating made by profiling of the Si substrate surface. The profile is rectangular with a profile depth h = 1.28 μm. The SiO_2 lattice is Si (111) substrate masked with a 1.15 μm thick surface film of vapor-deposited silicon oxide. The periodic structure of oxide strips with a period Λ= 3.75 μm was obtained with the help of normal photo-resist etching techniques (*Fig. 49*).

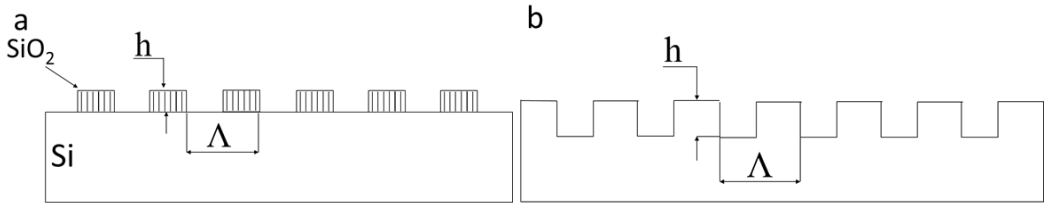

Fig. 49. The silicon gratings under study: SiO_2 lattice deposited on silicon (a) and profiled silicon lattice (b) with periods of Λ=3.75 microns.

The substrate was aligned to set the lattices ridges parallel to the diffraction plane. In order to take Fourier-transform images of the sample, the symmetric Bragg 111 reflection (θ_B = 6.88^0) was used. The primary slits were opened to 1000 mm height and 1000 mm width. The Sensicam camera was situated at CRL focal plane. The distance CRL–gratings were 0.85 m and distance grating-camera equals 0.5m (*Fig. 50*)

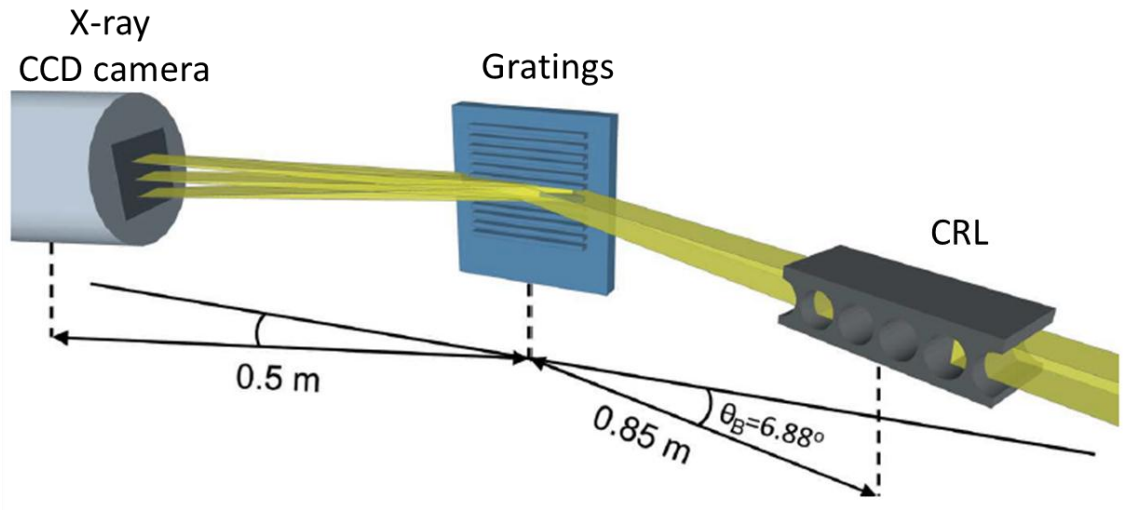

Fig. 50. The experimental scheme of the CRL Fourier transform on a silicon gratings

The Fourier transforms were performed by silicon planar parabolic lenses with the following parameters: radius of curvature R_c = 14.65 μm, number of individual lens N = 3, bridge spacing between individual lenses a = 5 μm, lens full aperture A = 500 μm. At the energy, E = 16.5 KeV any lens has a focal distance 135 cm, an effective aperture A_{eff} = 130 μm, an intensity transmission T = 17.5% and a diffraction-limited resolution $\sigma \approx 0.5$ um. During the experiment, the focal spot size is mainly defined by the source-size projection and equals $\sigma \approx$ 2.7 μm.

As a result, series of images were obtained near the silicon (111) diffraction (*Fig. 51*) reflection for both SiO_2 deposited on silicon and for profiled silicon structures.

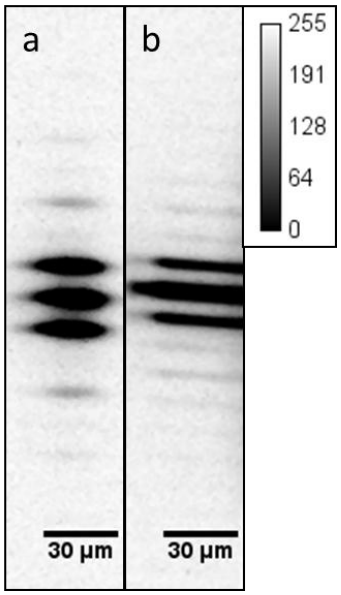

Fig. 51. Diffraction images near Si (111) diffraction reflection for profiled Si grating (a) and for SiO2 grating deposited on a Si (b).

As it can be seen in reciprocal space maps obtained by lens Fourier transform method (*Fig. 52*) different microstructures yield different results. By analyze of reciprocal space map we can conclude about different nature of images contrast formation.

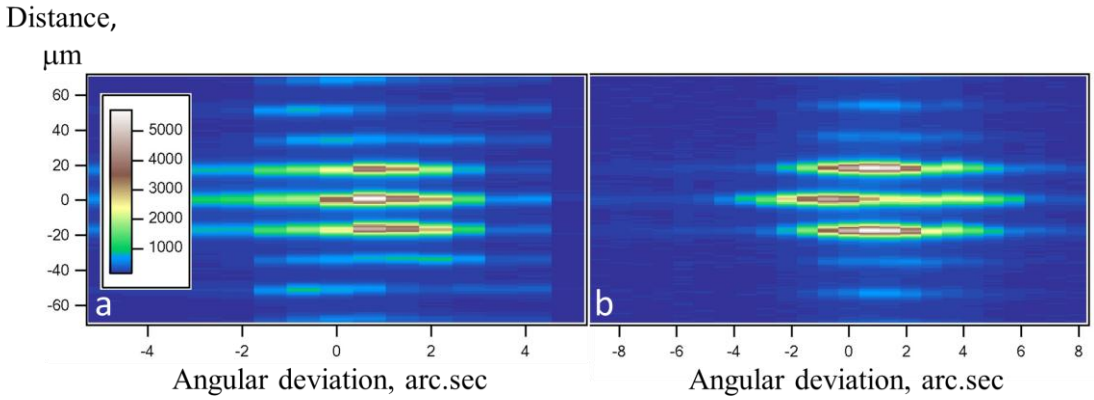

Fig. 52. Reciprocal space map at Si (111) reflection for SiO2 grating deposited on a Si (left) and for profiled Si grating (right).

The diffraction planes are parallel to the oxide ridges in our experimental arrangement, and the function $\varphi(x)$ describes the phase distribution on the surface across the direction of periodicity:

$$\varphi(x) = 2\sin^2\theta_B \frac{H}{\chi_h K} u(x) + \pi, \tag{34}$$

where H is the reciprocal lattice vector, χ_h is the polarizability coefficient, $K = 2\pi/\lambda$ is the absolute value of the wavevector and $u(x)$ is the vertical crystal lattice displacement from the ideal position. The maximum value of the displacement u_{max} is evaluated as

$$u_{max} = 2\sigma t\left(A\frac{\sqrt{B}}{B^2+1} + C\arctan\sqrt{B}\right), \tag{35}$$

where σ is the average stress, E is the Young's modulus, η is the Poisson's ratio, and

$$A = \frac{1}{4\pi\mu}, B = \frac{1-\eta}{\eta}, C = \frac{1}{4\pi(\gamma+\mu)},$$
$$\mu = \frac{E}{2(1+\eta)}, \gamma = \frac{E\eta}{(1+\eta)(1-2\eta)} \tag{36}$$

From the above formulae and the values for an Si substrate (E = 170 GPa, η = 0.28,σ = -0.3 GPa) and for the reflection Si (111) we can obtain that the minimum oxide strip thickness t

that can be resolved by this FT technique with 5% intensity contrast is about 40 nm for a structure with a period Λ = 3.75 mm. In this case the maximum phase shift $\phi = \pi/4$.

The profiling of the perfect crystal surface results in the binary phase modulation of the wave diffracted by the perfect crystal, and this phase modulation depth depends linearly on the profile depth:

$$\phi = \frac{2\pi|\chi_0|h}{\lambda \sin\theta_B}, \tag{37}$$

where h is the profile depth and χ_0 is the zeroth-order Fourier component of the crystal polarizability. It follows from equation (37) that in the used experimental conditions the phase depth φ of this binary phase grating should be equal π at the chosen energy.

Reciprocal space maps were simulated near (111) reflection of silicon for two types of gratings (*Fig. 53*).

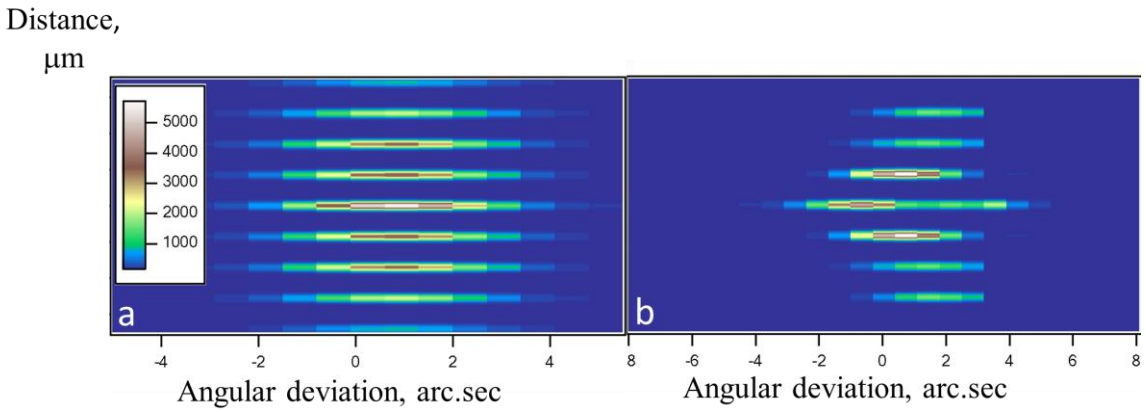

Fig. 53. The simulated reciprocal space maps for SiO_2 grating deposited on Si(left)and for profiled Si grating(right).

The best fit between the calculated and experimental rocking curve patterns was achieved with the value of the average stress σ = -0.27 GPa for SiO_2 grating. This value is smaller than σ = -0.3 GPa for Si substrates [58] and this difference can arise from the lower adhesion properties of SiO_2 films on the Si substrate prepared by the chosen technology. The difference between the theoretical and experimental rocking curve mappings can be explained by the fact that the mathematical model of displacement or strain in the substrate lattice planes is not exactly correct.

As it can be seen from the simulated reciprocal space maps, the chosen approach is valid. Inaccuracies are associated with diffuse scattering which was not taken into account in the modeling.

4.3. Study of Si-Ge nano-heterostructure by CRL Fourier transform method

To understand the main principles of the X-ray CRL FT method in Bragg geometry, Si-Ge nano-heterostructure was chosen as a sample. The sample was produced by IHP laboratory, Frankfurt (Oder), Germany[59]. The Si-Ge nano-heterostructure was obtained by the epitaxial growth of germanium on nanostructured silicon (001) wafers with low defect density[60]. The preparation of nanostructured Si(001) wafers is based on the methods used to realize gate oxide spacers within the IHP 0.13 μm BiCMOS technology[61]. A regular grid of structures with a periodicity of 360 nm in perpendicular directions was produced.

The concept of nano-heteroepitaxy was first proposed by Zubia [62, 63]. The main idea is to create a three-dimensional stress relief mechanism by nanostructuring of hetero-epitaxial object. The Si-Ge hetero-epitaxy has the high lattice mismatch m=4% between silicon and germanium which resulted in stress formation in the interface. Lattice parameter for Si is 5.4309 Å and for Ge is 5.6578 Å in the relaxed state. Nanostructuring makes it possible to relieve stress from germanium.

The studied Si-Ge nano-heterostructure is 100 nm Ge nanocrystals on free-standing 90 nm width and 150 nm height Si (100) pillars with a periodicity of 360 nm along the (110) crystal direction (*Fig. 54*).

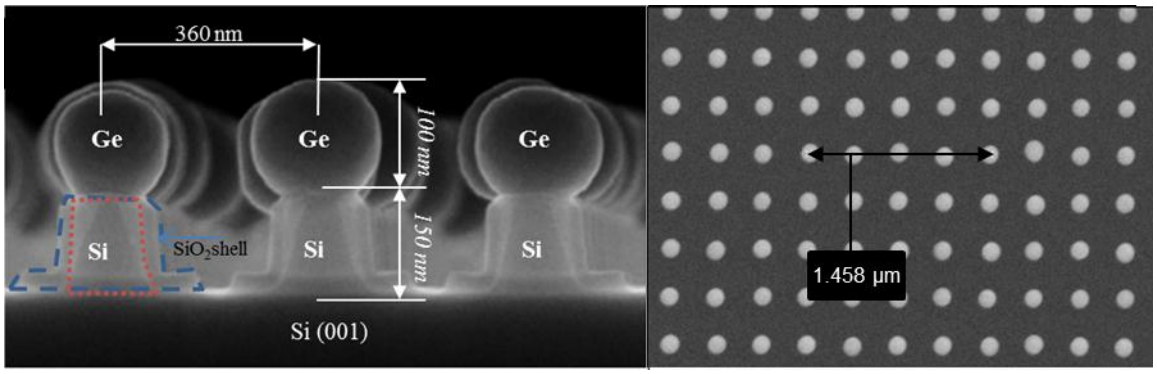

Fig. 54. The SEM micro - images of Si-Ge nano-heterostructure, side view (left image, adapted from[64]) and top view(right image).

4.3.1. Lenses before object

In the chosen geometry transfocator is located closer to the source (see the table 3). This position of the focusing element makes it possible to reduce the angular aperture on the side of the image in the horizontal direction in comparison with unfocused radiation,

which allows one to reduce the instrumental contribution to the crystal rocking curves. Focusing was performed in the vertical direction.

The Si (001) substrate plane was generally rotated for the angle θ and the camera was oriented so as to form the angle 2θ with the incident radiation direction. The angle θ corresponds to the Bragg diffraction peak 400 from the Si sample surface. The X-ray camera recorded a series of images at different detuning angles $\Delta\theta$ from the angle θ.

In the case of focusing by use of the transfocator, we scanned the vicinity of the Si Bragg diffraction peak 400 with a step δq = 0.83 μm^{-1}. Cartridges with 12 refractive lenses with a radius of curvature of 200 μm and one refractive lens with a radius of curvature of 500 μm were mounted in the transfocator. No diffraction peaks (or nonzero Fourier components) caused by the submicron sample structure were found in this region. Nonzero Fourier components begin to arise upon crystal detuning by Δq=86 μm^{-1}. According to the relation between the observed pattern period T and the grating period d,

$$d = \lambda r/T$$

(λ is the wavelength and r is the distance from the sample to the detector).

Table 3. Experimental parameters

Measurement scheme	X-ray energy, KeV	Distance to the source L, m	Focal length f, cm	Distance from the sample to the camera r, cm
Transfocator before the sample, linear focusing	24	39	1965	35

The error in estimating the period is mainly related to the accuracy of determining the distances between the object and the camera.

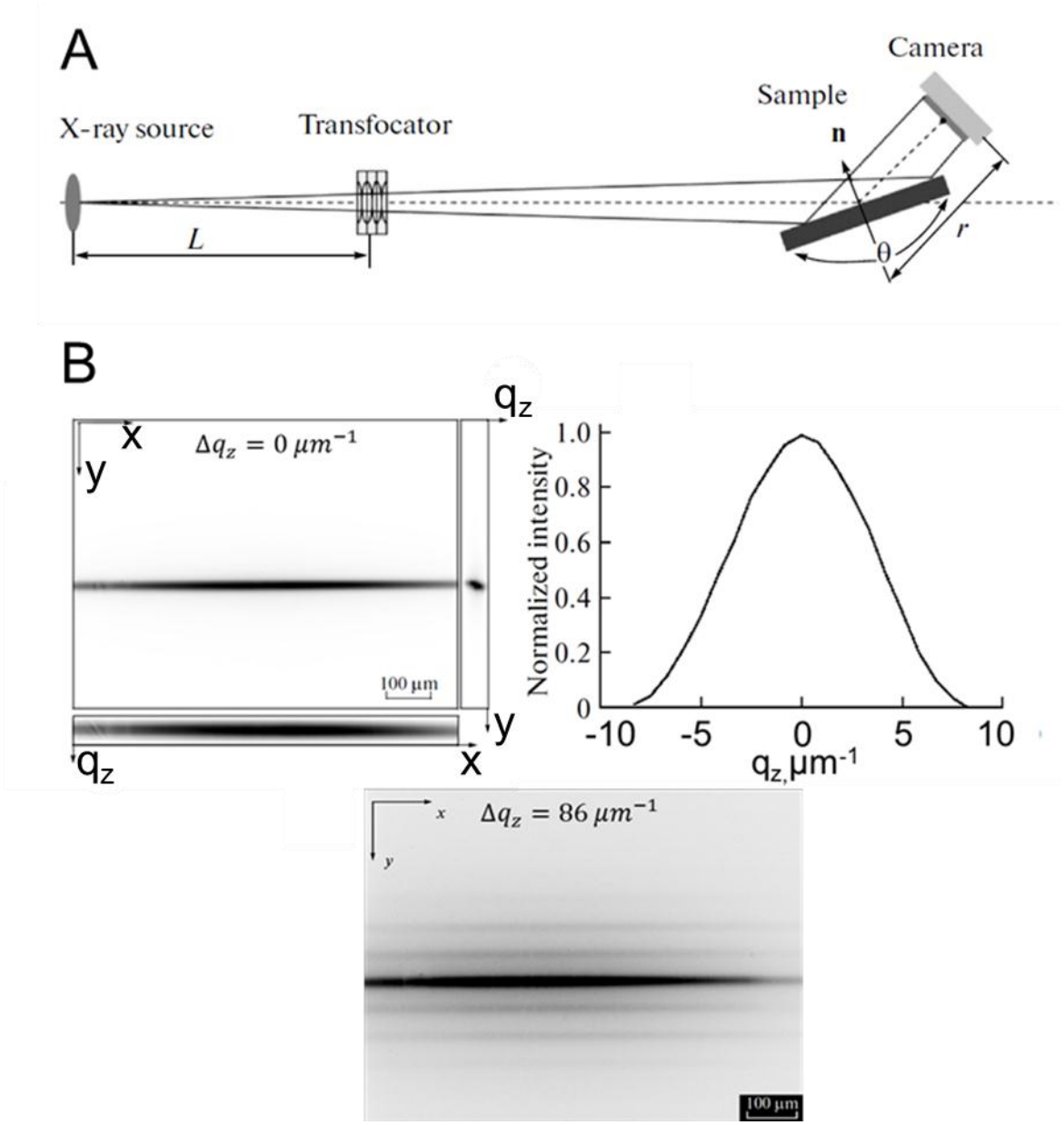

Fig, 55. A. Experimental scheme. B. Experimental results.

The image obtained by the camera also contains pattern distortions related to the presence of defects in the sample, which yield contrast at the observed Fourier components. Hence, use of the transfocator makes it possible to make the Fourier transform in one direction and obtain a topographic image of the analyzed region, limited by the projection of the source, in the other direction.

To perform CRL FT, 10 Beryllium lenses were used which enabled us to obtain the focal distance f=1.49 m. The Si-Ge nano-heterostructure was placed at the distance a=1.05 m (*Fig. 57*).

Si 400 reflection was chosen due to the high Bragg reflection intensity. Firstly, on the X-ray camera a Bragg reflection was found. The Si 400 Bragg angle is $\theta = 19.034^0$ at energy E=14 KeV.

After the alignment of an X-ray camera, several images of the focal spot were recorded and compared. The X-ray spot size should be as small as possible to provide the maximal FT resolution at the required camera position. The experimentally obtained focal spot size is 7 μm in vertical direction and 17 μm in horizontal direction (*Fig. 56*).

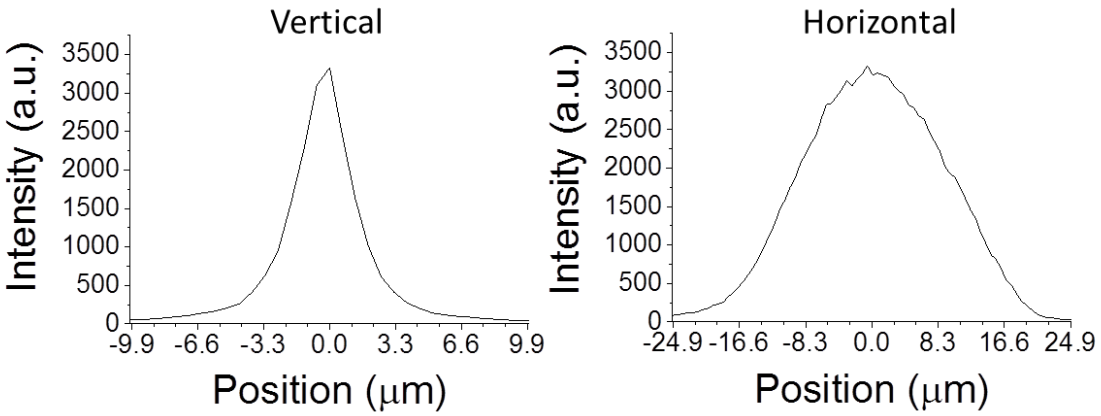

Fig. 56. The vertical and horizontal beam profiles of the smallest achieved beam spot at the experiment.

After the alignment procedure, a series of images were recorded at different angles θ in the area of the Bragg reflection Si 400 (*Fig. 58*). As it can be seen in *Fig. 58*, a periodical pattern is obtained at angles $\theta_1=-0.012^0$ and $\theta_6=0.007^0$. In the $\Delta\theta=0\pm0.004$ range, effects of dynamical diffraction is represented as horizontal intensity line on the FT pattern. So, we could distinguish the angle range at the rocking curve useful to analyse the silicon pillars periodicity and symmetry.

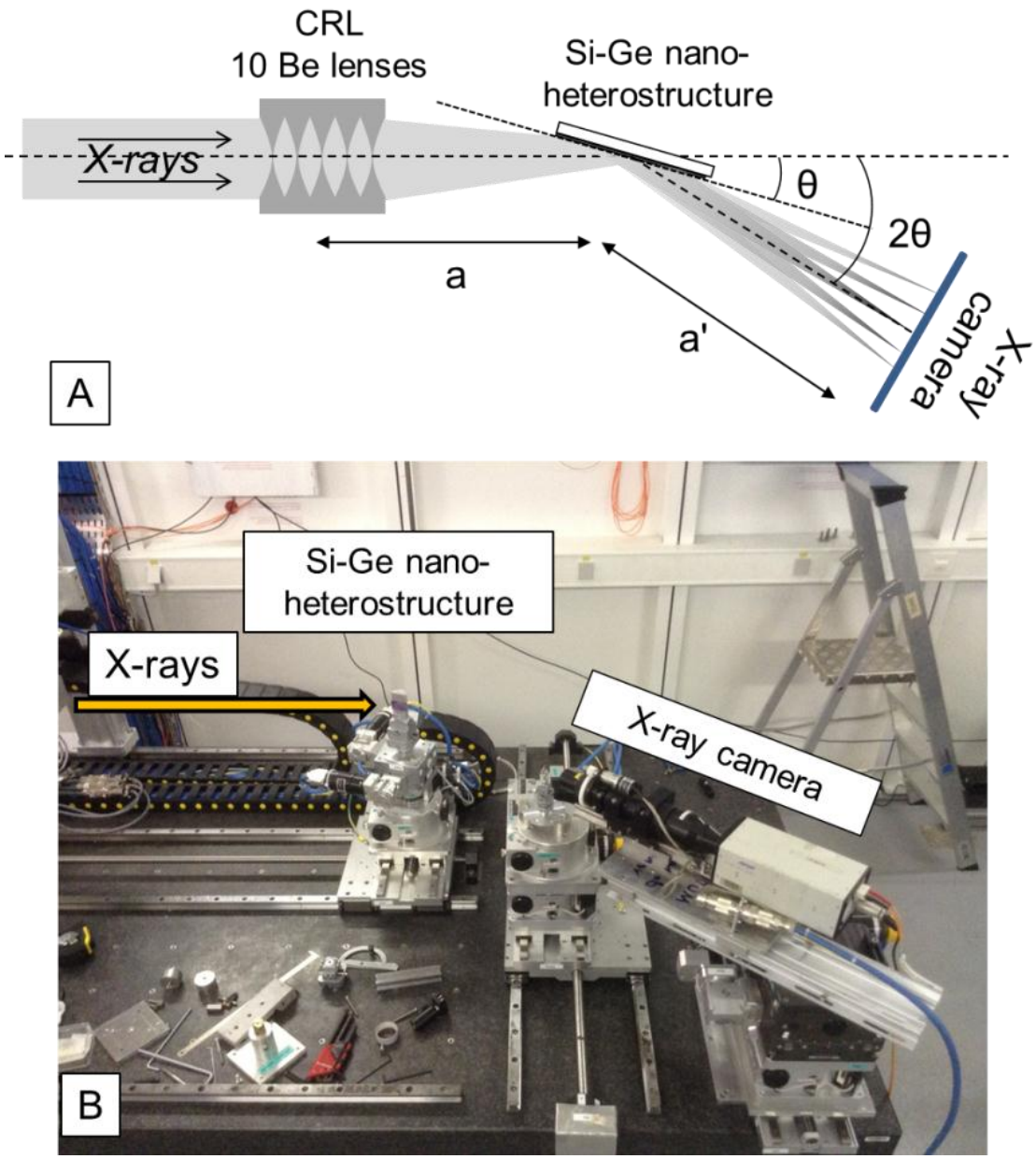

Fig. 57. CRL FT experimental scheme, CRL before object: A. scheme drawing; B. photo from experiment on experimental hutch 1, ID06.

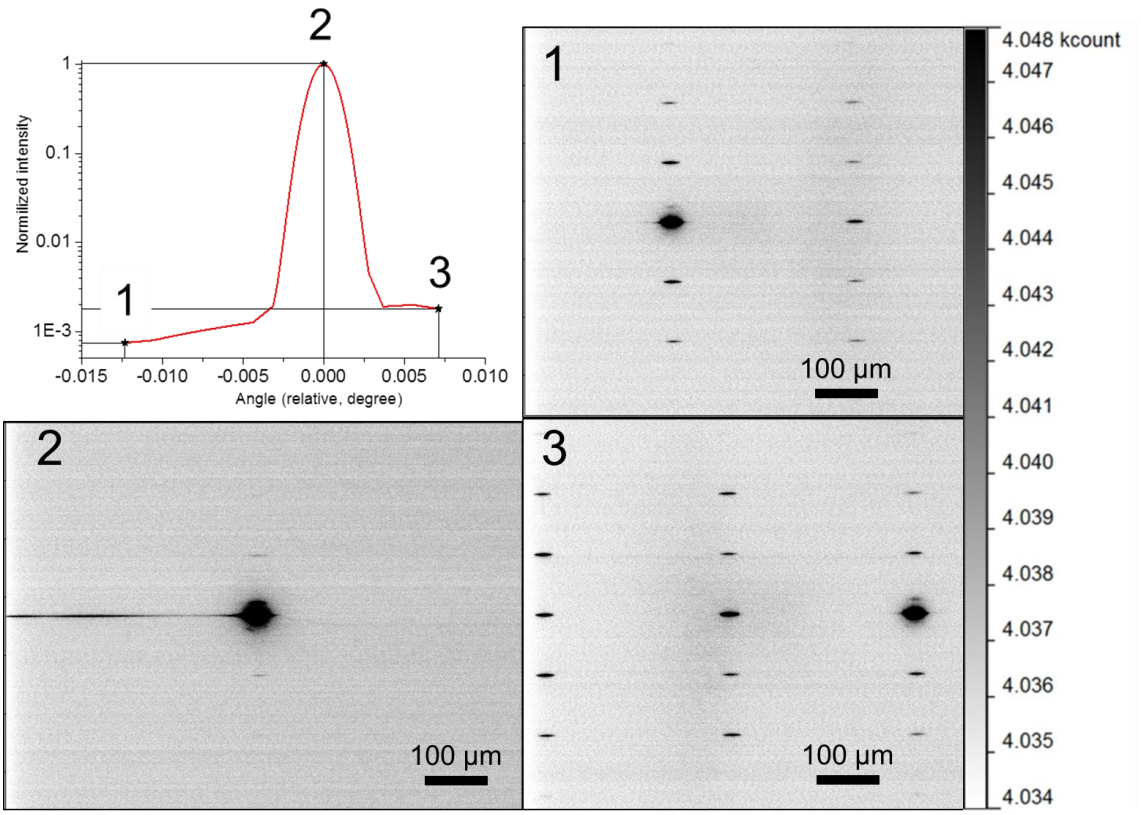

Fig. 58. Rocking curve of Si-Ge nano-heterostructure (upper left figure) and corresponding images of obtained FT patterns.

Fig. 59 shows the line profiles of obtained FT patterns which consist of periodical spots, which are Fourier frequencies. The sizes of the Fourier components correspond to the X-ray source size and lens demagnification factor. Under the classical Fourier optic theory, the FT from a periodical object represents the multiplied source image within the Fourier frequencies. The highest resolution is achieved at lenses imaging distance, where the source image is created.

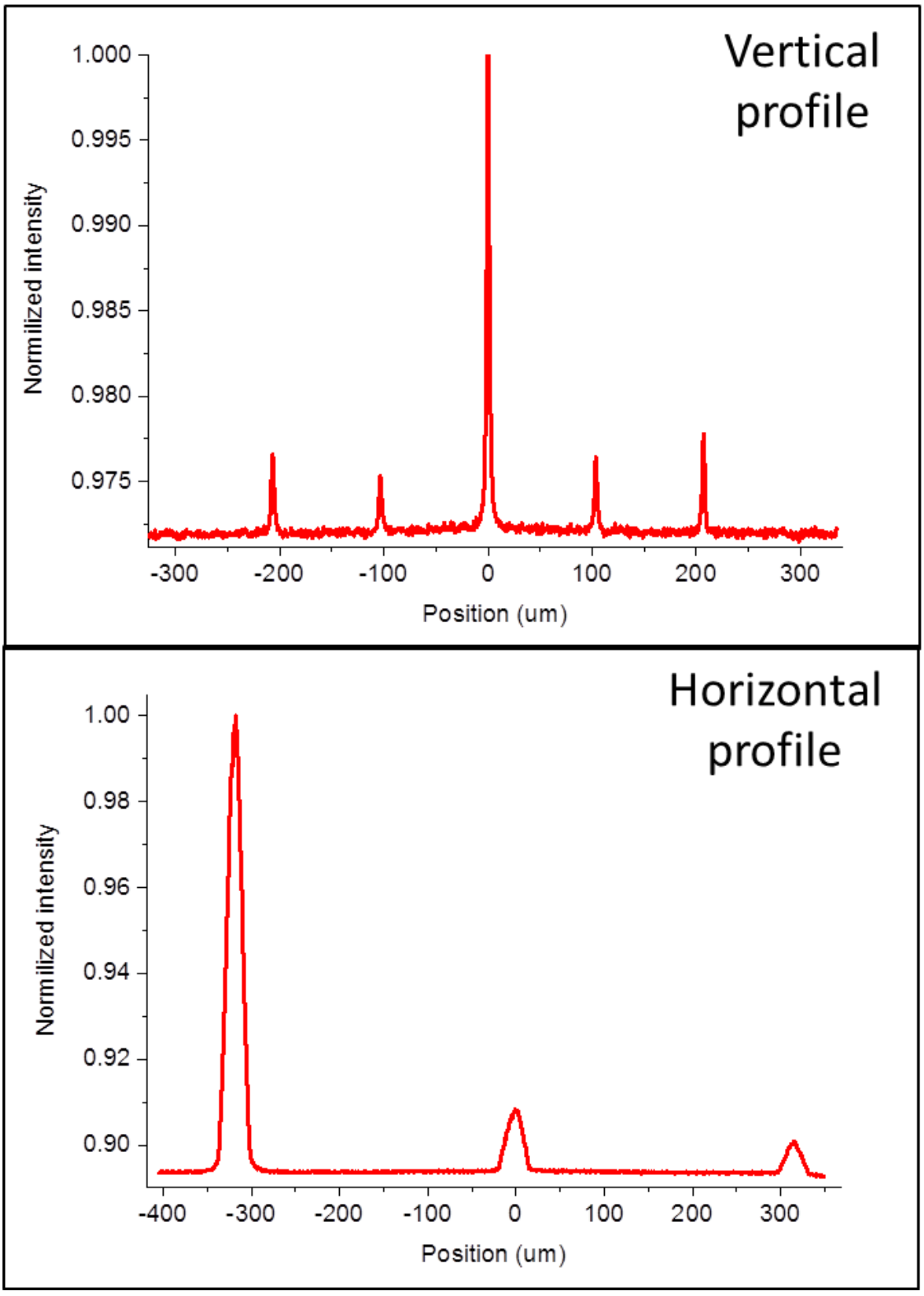

Fig. 59. Periodical Fourier pattern at θ_6=0.007° with corresponding vertical and horizontal line profiles.

After the determination of Fourier frequencies positions (table 4), it can be evaluated that the vertical period is T_v=103±1 μm, and the horizontal period is T_h=317±1 μm.

Table 4. The measured peak position of line profiles.

Vertical profile		Horizontal profile	
№ of peak	Position, μm	№ of peak	Position, μm
1	-207	1	-318
2	-103	2	0
3	0	3	316
4	103		
5	207		

According to the relation between the periodical function and its FT image, the observed Fourier frequencies period T satisfies the equality $T=\lambda a'/\Lambda$, where λ is the X-ray wavelength, a' is the distance from sample to imaging plane, and Λ is the sample periodicity.

The nominal silicon pillars period is in good agreement with the calculated period from Fourier image (Table 5).

Table 5. The main CRL FT parameters in the experimental scheme.

Fourier Period, μm	Wavelength, Å	Distance sample-camera a', m	Calculated pillars period, μm	Nominal pillars period, μm
103	0.886	0.42	0.360	0.360

The calculations are correct for the vertical Fourier frequencies periodicity T_v, but for the horizontal they are not. In Bragg geometry, Fourier image is stretched horizontally. In order to recalculate the real horizontal periodicity T_h, and to take into account the Bragg geometry, the equality should be used

$$T_h = T_h' \cdot sin\theta, \tag{38}$$

where T_h' is the stretched horizontal periodicity of the Fourier frequency, θ is the Bragg angle. For the obtained experimental data, T_h =103 μm for θ = 19.034^0 this is equivalent to

the vertical periodicity T_v. The equality between T_h and T_v is valid for cubic symmetry of the silicon pillars.

It means that by CRL FT it is possible to observe precisely the existing nanostructure over a surface, and to provide dynamical experiments. The geometry where the lenses are before the object, makes more problematic to interpret the reciprocal space. Due to the fact that the wave incident on the object diverges, the produced Fourier pattern emerges as a superposition of rays diffracted at different angles.

Solution to this problem is in situation of lenses after the object.

FT on a large area detector

For observation X-ray diffraction on Germanium islands PS detector were used (table 6). Due to the higher quantum efficiency, PS camera is much more sensitive in comparison with Sensicam.

Table 6. PS detector technical characteristics

Pixel size, μm	6.5
Average Quantum efficiency at 8-20 KeV, %	50
Working Area	2048·2048 pix 13.3 mm·13.3 mm

Due to the higher sensitivity and large detector area, the whole diffraction pattern was detected near the Si 400 reciprocal point. Zero Fourier component corresponds to X-ray diffraction from Si substrate without Si pillars and Ge islands.

Due to the Si pillars existence on a surface, Bragg's satellites forms at reciprocal spaces which correspond to two-dimensional lattice in qx and qy directions.

The X-ray camera split reciprocal space at angle which corresponds to a crystal rocking angle due to the Bragg geometry of experimental scheme (*Fig.* 60). That's a reason why observable periodicity has longer period along x direction than along y direction.

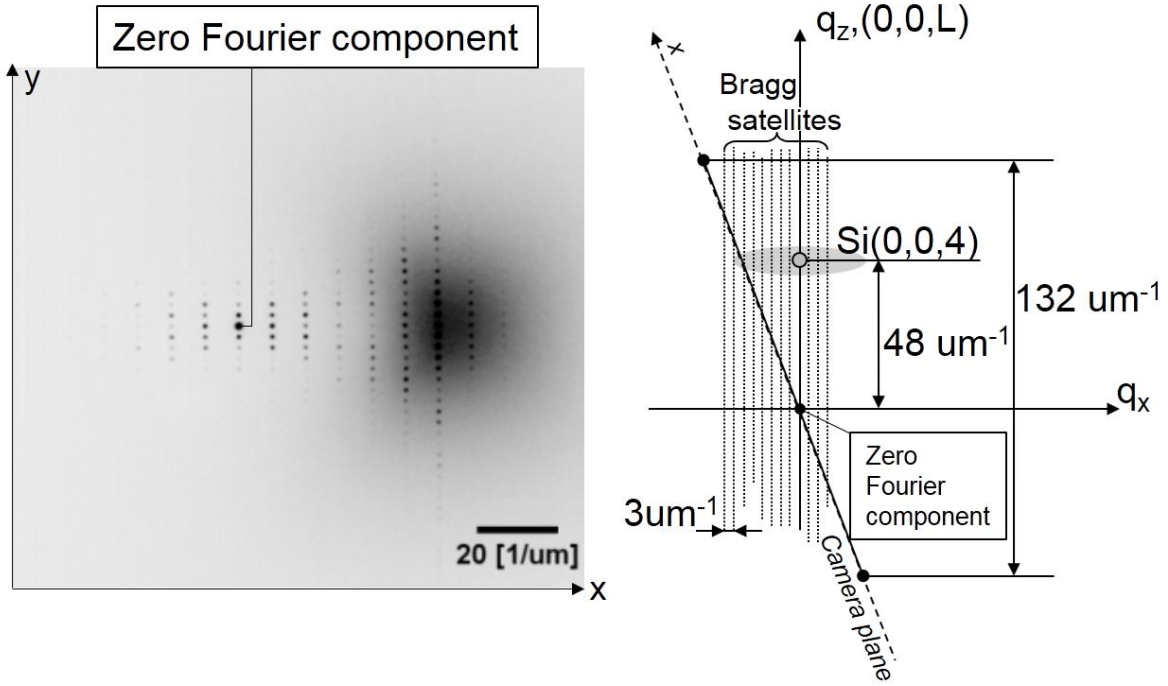

Fig. 60. The detected on an X-ray camera diffraction pattern and scheme of a camera alignment at reciprocal space.

Due to the nano-structure perfection, the fine diffraction pattern appeared at reciprocal space. As a result, reciprocal space with dimensions 51 $\mu m^{-1} \cdot 129\ \mu m^{-1}$($q_x \cdot q_y$) was registered by PS camera and CRL.

4.3.2. Lenses after object

The beam conditioning and alignment for this geometry are the same as for lenses before object except of the sequence of procedures. The lens positioning was performed at the end of alignment procedure by pin diode. Pin diode was used to find maximum of an intensity, which proved that lenses were in the correct position. After establishment of the intensity maximum, the smallest spot was found with the help of consequent recording and comparing images of the X-ray camera.

50 parabolic beryllium lenses were used at X-ray Energy E=15 KeV to perform CRL FT (*Fig. 61*).

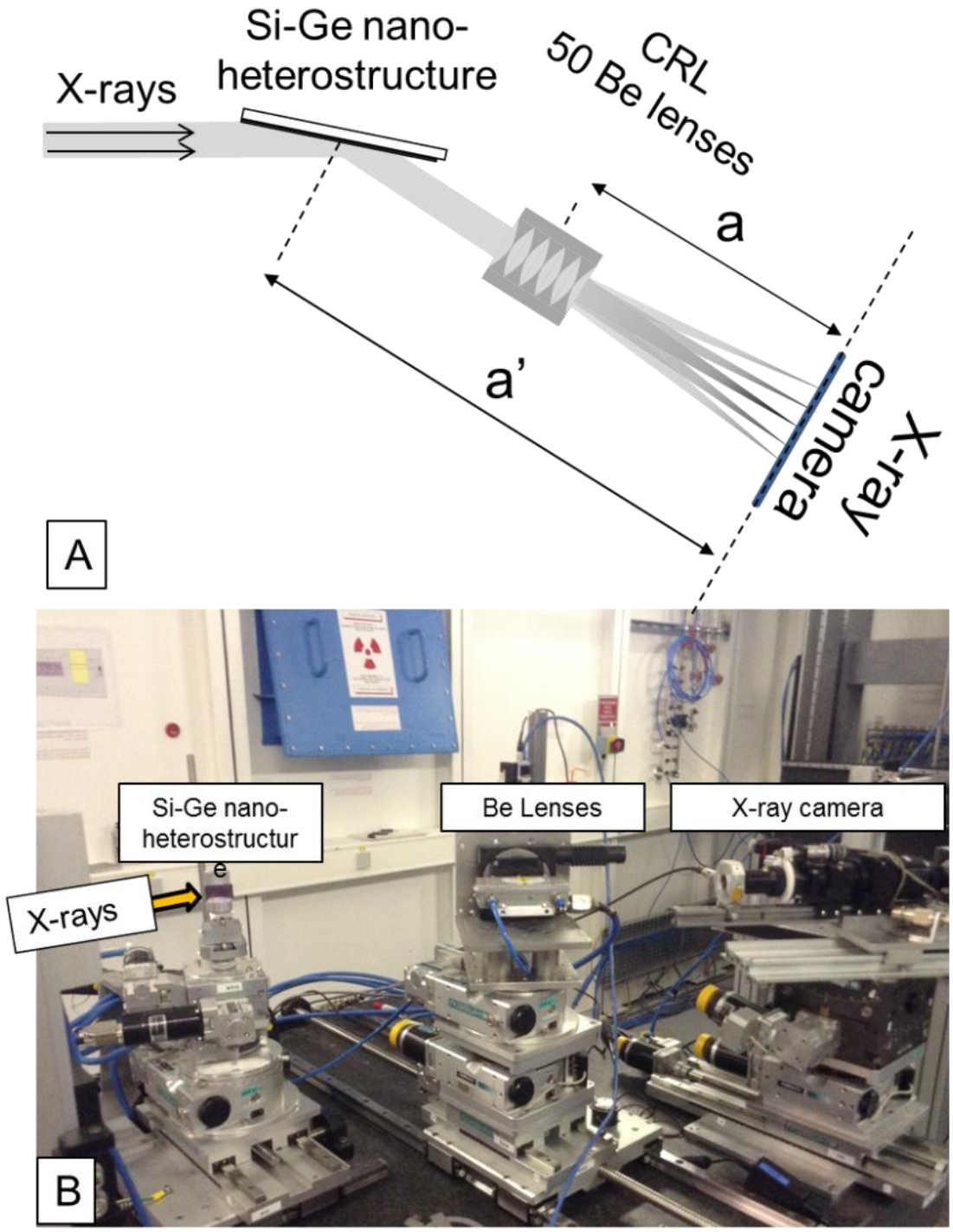

Fig. 61. FT experimental scheme, CRL after object: A. scheme drawing; B. photo from experiment on ID06 experimental hutch 1.

After the alignment procedure, the series of images for different angles θ close to the silicon 400 reflection (θ_b= 17.722^0) was recorded. As we can see at the images (*Fig. 62*), the periodical pattern from silicon pillars is observed at angles $\theta=\theta_b\pm0.006^o$. The problem in observing of a periodical Fourier pattern at Bragg angles relates to the high intensity of the

reflection and limitations of camera- dynamical detection range. As a result, it is useful to attenuate the intensity by an offset from Bragg reflection during the silicon pillar analysis. The calculated pillar period is in a good agreement with the nominal.

The main differences between the lens arrangements relative to the object are:

- When lenses are before the object, they produce a divergent beam which creates an image of a superposition of different incident ray directions. As a result, additional elements corresponding to the reciprocal space sweep appear on a Fourier pattern.
- When lenses are located after the object, one can separate Fourier images for specific θ angles. As a result, it is possible to record a series of images and assemble 3-dimensional reciprocal space volumes.

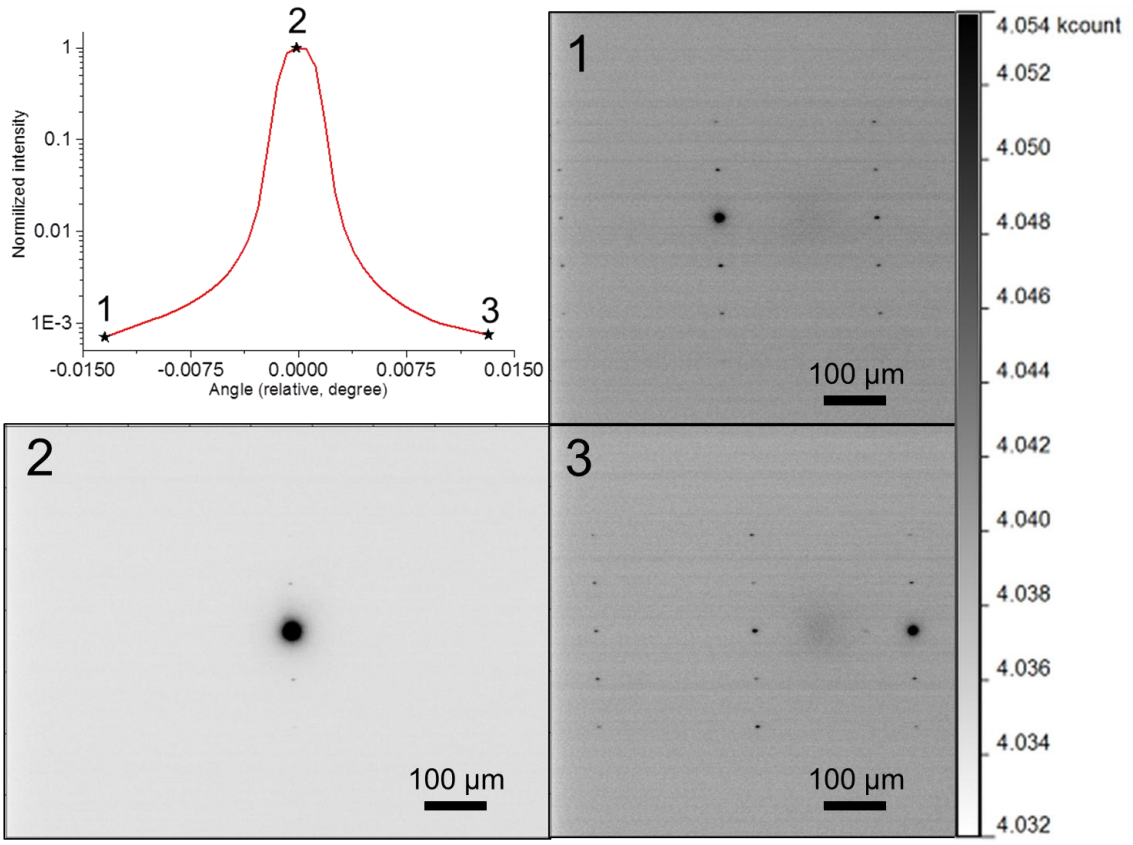

Fig. 62. Rocking curve of Si-Ge nano-heterostructure (upper left figure) and corresponding images on an X-ray camera.

FT on a large area detector

At another geometry, when lenses were after the sample, the Germanium 400 reciprocal point was detected. Also, CRL filter higher Fourier orders at used experimental alignment (*Fig. 63*).

As a result, reciprocal space near Ge 400 reciprocal point represents blurred halo which corresponds to the defected crystal structure of Ge islands.

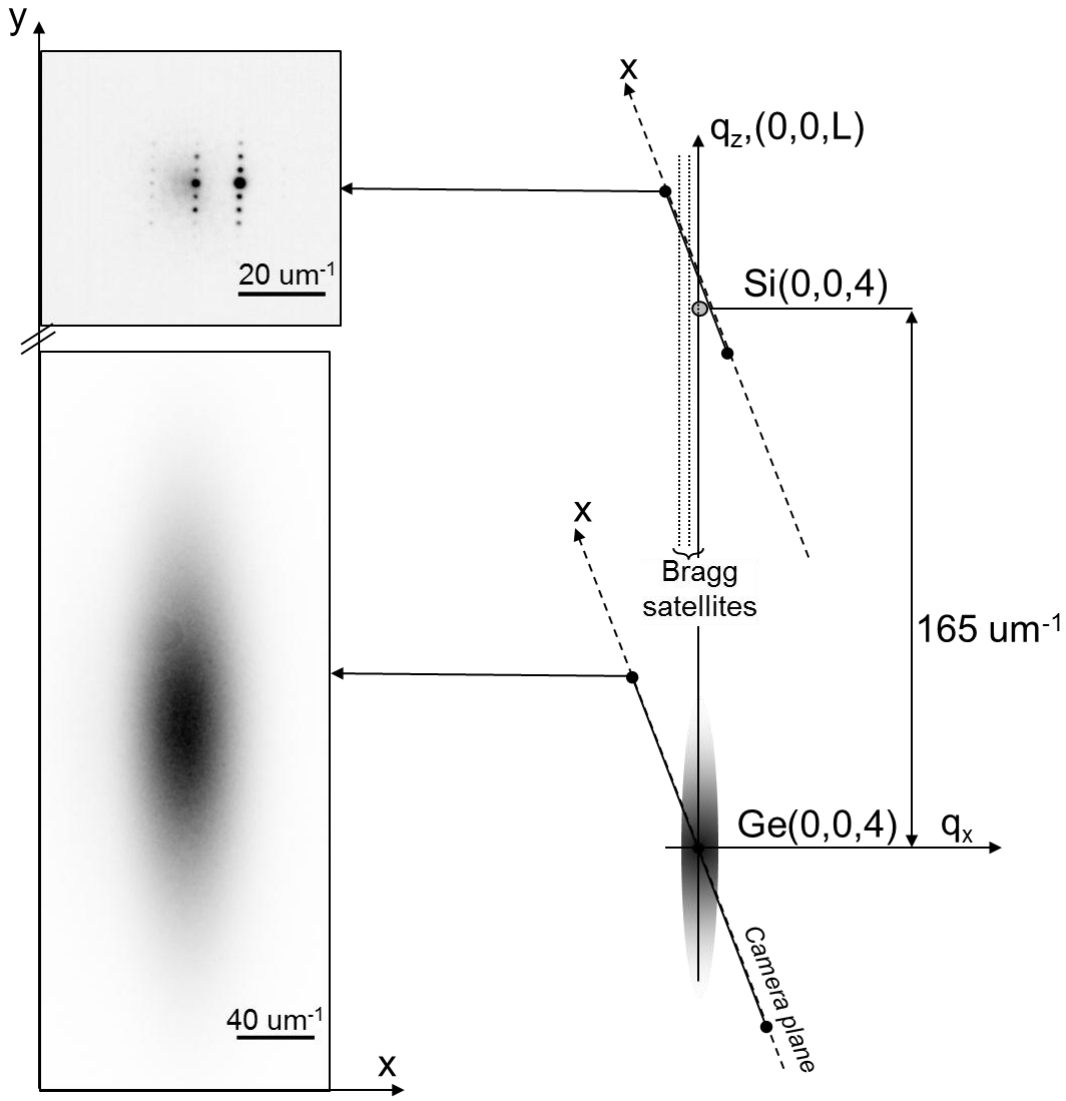

Fig. 63. The reciprocal space near Si004 and Ge 004. CRL after the sample.

4.3.3. Resolution in reciprocal space

Å^{-1} was chosen as a measurement unit of scattering vector in reciprocal space due to the versatility of this unit for different wavelengths. The resolution of FT in a reciprocal space is determined by minimal recordable scattering vector. That parameter depends on X-ray source size and magnification factor of the used optics. The smallest spots obtainable in the Fourier experiment are demagnified source image in an imaging plane. Vertical and horizontal profiles of recorded spots for different geometries are shown at *figure 64*. Also, the achieved resolution in the reciprocal space was estimated.

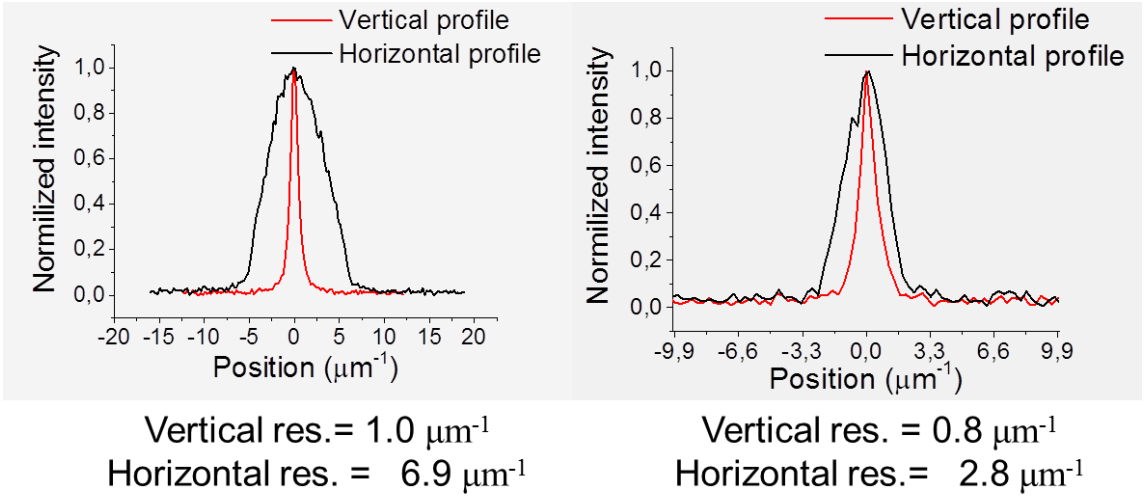

Fig. 64. Recorded Fourier patterns for two geometries: CRL before object (left) and CRL after object (right).

As for the conventional triple crystal technique, the maximal achievable resolution for these samples, is about of 10 μm^{-1} [64].

4.3.4. Comparison of the new approach with conventional techniques

The main parameters to compare are:

- Resolution in the real space. Due to the focusing of the X-ray beam for CRL FT, the analyzed region decreases, which opened up new possibilities in sample mapping.
- Resolution in the reciprocal space. CRL FT technique gives an opportunity to record reciprocal space with the highest resolution possible to date. The achieved resolution allows us to analyze a crystalline micro-structured grid with periodicity up to 8 μm.
- Exposure time. The new approach is not scanning in principle, which means that one could sweep reciprocal space quickly and observe dynamical processes in a reciprocal space.

Table 7. Comparison between Triple Crystal Diffractometry and CRL FT

Parameters	**CRL FT**	**Triple Crystal Diffractometry**
Resolution achieved in reciprocal space	0.8 μm^{-1}	~10 μm^{-1}
Resolution achieved in real space	~0.2 mm	tens of millimeters
Average experimental time	0.1 sec	hours

4.3.5. Conclusions

The new CRL FT approach as a HRXRD technique gives an opportunity to analyze semiconductor nano- and micro- structures with the highest possible resolution in a reciprocal space. Also, the new method is a feasible way to observe dynamical processes with high resolution in real space. The minimal experimental size of analyzed region which was achieved is about 0.2 mm.

As a result of the effective use of new synchrotron X-ray sources, the 3D reciprocal volumes could be recorded in detail. The high-resolution diffraction volumes will provide the information about symmetry, sizes, 3D- stress and defects distribution in nano- and micro- structures.

An X-ray CRL FT could be used to design the X-ray dark-field microscope similar to the transmission electron microscope where both electron micro-images (information about real space) and diffraction patterns (information about reciprocal space) can be observed for the same region.

4.4. Study of membranes and films with X-ray reflecto-interferometer

To estimate HRXRI possibilities, three Si_3N_4 membranes 200 nm, 500 nm and 1000 nm and PMMA film with thickness 100 nm were used as objects (*Fig. 65*). Beryllium parabolic refractive lenses were used to produce a cone beam.

To obtain an interference pattern, the X-ray beam was focused on a sample surface. The sample was tilted at angles close to critical, where Kiessig fringes exist.

4.4.1 Si_3N_4 Membrane. Test of angular resolution

To estimate the HXRI possibility of resolving Kiessig fringes, three types of Si_3N_4 membranes were used with 200-, 500 - and 1000 nm thickness.

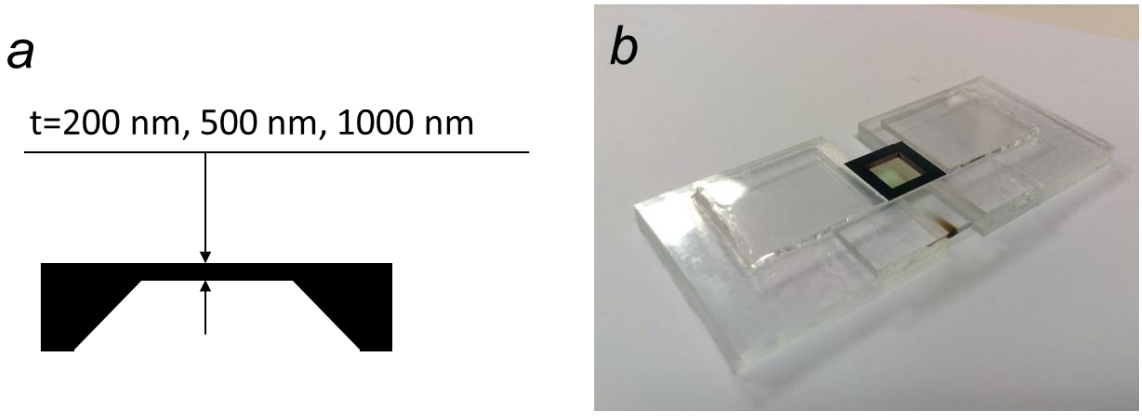

Fig. 65. The Si3N4 membranes drawing (a). Specially designed glass holder for membranes with burnt beam print (b).

The main experimental parameters are shown in table 8. To create a cone beam, 71 beryllium lenses were used with 50 μm radius of curvature with focal distance f=22.7 cm at 14.4 KeV X-ray energy (*Fig. 66*). The interferograms were formed at angular aperture $\Delta\theta$=2.08 mrad. The main errors come from measuring of a distance between the membrane and the X-ray camera.

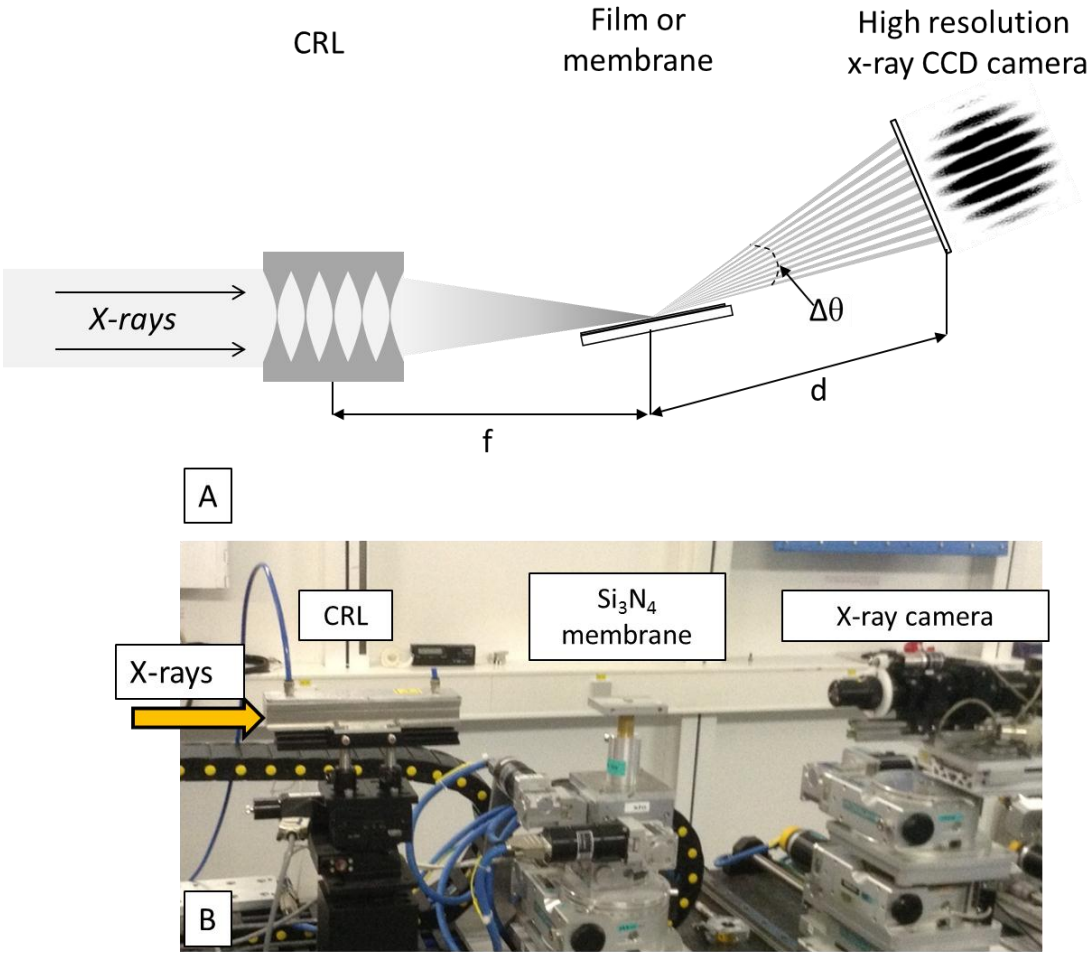

Fig. 66. HXRI experimental setup, CRL focus X-ray beam onto a film/membrane surface and sweep interference pattern on the X-ray camera: A. HXRI drawing; B. HXRI setup photo from ID06 experimental hutch 1.

Table 8. HXRI experiment parameters.

Nominal membrane thickness, nm	Focal distance, f, cm	Distance from membrane to X-ray camera, d, cm	The angular distance between maxima, μrad	Calculated membrane thickness, nm
200	22.7	34.0±1.5	211±25	204 ±24
500		30.6±1.5	87±5	495 ±28
1000		30.6±1.5	41±2	1053 ±61

As can be seen from interferograms (*Fig. 67*), Kiessig fringes from all membranes are resolvable. At $\theta=\theta_{cr}$, total external reflection region can be observed where the interference pattern disappears.

The 71 beryllium lenses produce a focal spot with 2.8 μm sizes in horizontal direction and 0.2 μm sizes in vertical direction (calculated at http://newton.phy.tu-dresden.de/applets/crlcalc.html) (*Fig. 68*). Due to the sample tilt, close to the critical angle, the beam projection on the sample in vertical direction varies from 110 μm to 10 μm. Despite this, HXRI provides thickness analysis for considerably smaller regions than conventional XRR techniques.

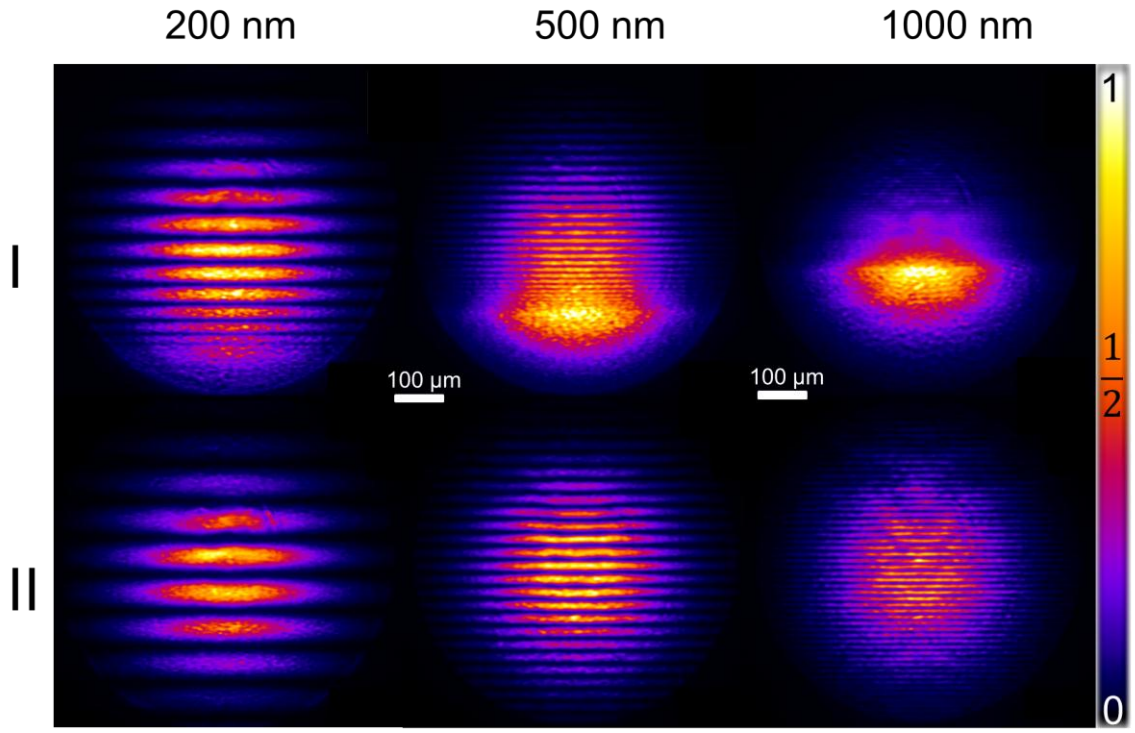

Fig. 67. HXRI patterns for Si3N4 membranes with different thickness at the critical angle of incidence (I) and at the region after the critical angle $\theta=\theta_{cr}+0.112^0$(II).

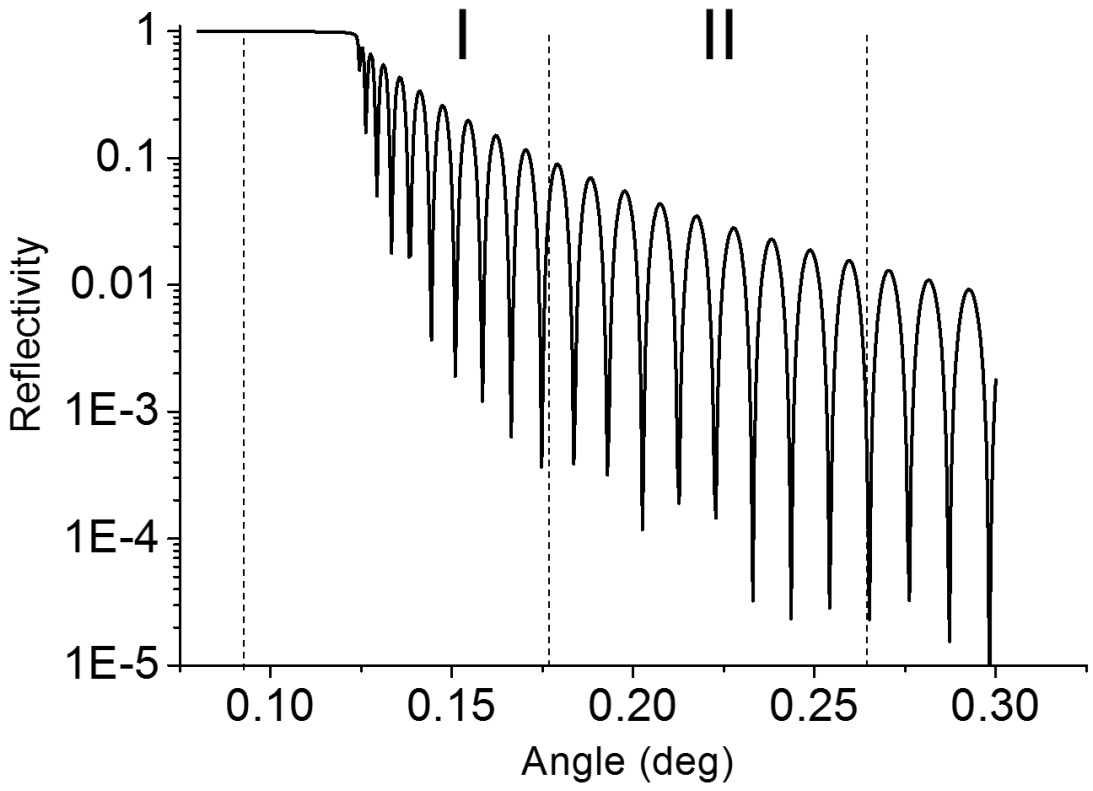

Fig. 68. Reflectivity curve calculated for the 200 nm Si3N4 membrane with marked regions shown in Fig. 67.

In the used experimental setup, the minimal membrane thickness possible to study is 62 nm which correspond to observation of 3 maxima in the interference pattern.

It can be seen in *Fig. 69*, the angular resolution limit of HXRI was not reached. For the used setup, the resolution limit is determined by the X-ray camera pixel size. The minimal camera-resolvable interference peak size is 2 μm. For the used HXRI setup, the calculated camera angular resolution is 6 urad, that means that the maximum resolvable film/membrane thickness is ~3000 nm. These estimates were made without taking into account the dependence of interference pattern contrast on a film/membrane thickness.

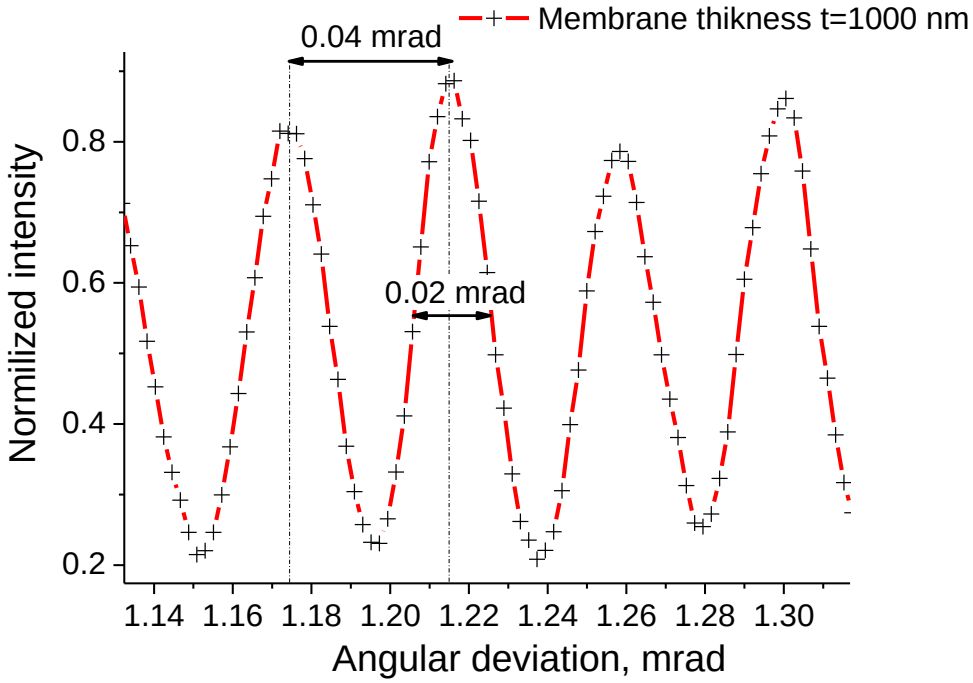

Fig. 69. Part of the obtained interference pattern from Si3N4 membrane with the thickness t=1000nm. The angular resolution limit is not reached.

The obtained results demonstrate that the new approach significantly improves the possibilities of reflectivity analysis in time, space and angular resolution (see table 9).

Table 9. Comparison between conventional XRR and HXRI

Parameters	HXRI	XRR
Analysis locality	~40 μm	Tens of millimeters
Experiment time	Less than a second	minutes
Angular resolution	6 μrad (experimentally obtained for selected geometry)	~100 μrad (for High resolution set-up consisting of Beam conditioning and analyzing crystals)

4.4.2. PMMA film. The HXRI PMMA degradation study under X-ray radiation

In order to test the HXRI as an instrument for *in situ* observations, we used 100 nm PMMA film as an object, which may degrade due to the radiation exposure.

In order to study the X-ray radiation degradation process, a fast shutter was used, which gave an exposure time control within 10 μsec accuracy. The exposure time was 0.5 s. After four images (2s), the interference pattern was blurred, which means that the integrity of the film was destroyed.

The most probable degradation mechanism is the formation of MMA in the exposed area. It can be seen in maxima movement in a low angle region due to the material density changes (*Fig. 70*). The PMMA density is 1.18 g/cm^3 and MMA density is 0.94 g/cm^3. The degradation process mainly changed the film density and flatness in the region.

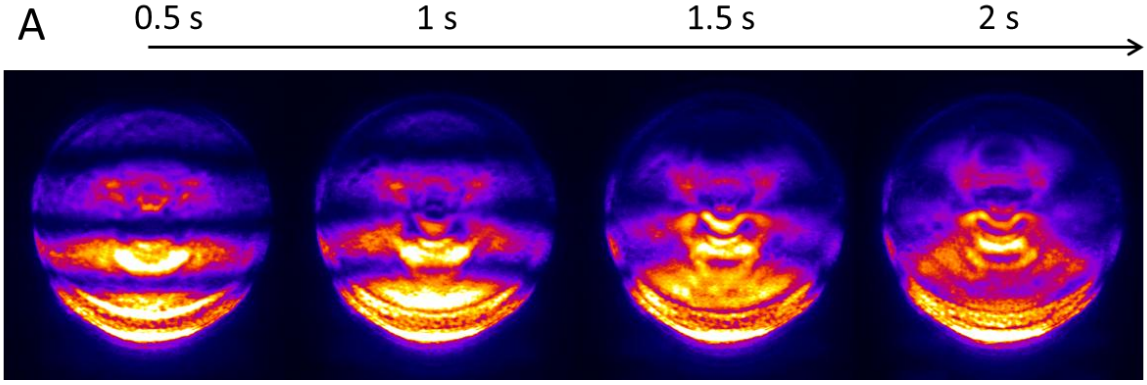

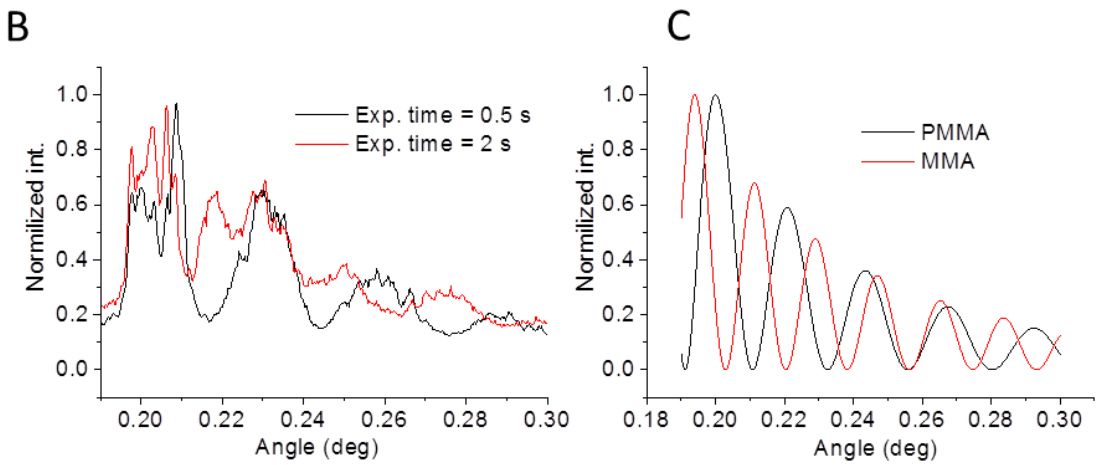

Fig. 70. A. Series of HXRI patterns showing the changing in a PMMA film after beam exposure. B. HXRI intensity profile at the 0.5s exposure time and at the 2s exposure time.C. Calculated XRR curve shows the maxima movement due to the MMA formation.

The considerable advantage of the HXRI is storage the XRR data without scanning. It opens up new possibilities in thin film researches and gives an opportunity to observe different processes in the film thickness in real time.

Conclusion and Outlook

In this thesis, the novel synchrotron X-ray diffractometry and reflectometry methods based on a refractive optics are proposed, discussed and studied. The experimental results obtained from the ID06 beamline at ESRF, Grenoble, France are presented and analyzed in this work in order to demonstrate a high angular and space resolution in addition to the opportunity to manage *in situ* and *on operando* experiments with the help of the proposed X-ray optical techniques.

We tailored the theory of visible light Fourier transform to the cases of X-rays and Bragg diffraction. The main equations and relations are presented at this thesis. Different geometries of sample and lens arrangement discussed. Also, the FT of a binary square-wave phase grating with phase depth ϕ is discussed.

The concept of multifunctional X-ray microscopy is considered as a possible future applying of CRL FT.

CRL FT techniques were used to analyze micro-radian diffraction from Si microstructures (SiO_2 lattice deposited on silicon and profiled silicon lattice) and from Si–Ge nano-heterostructures representing two–dimensional lattice of nano-epitaxial germanium islands on a silicon pillars. It was concluded that CRL FT technique is usable for reciprocal space mapping and provides a resolution 10 times higher than that achieved with traditional HRXRD methods.

The HXRI concept is an alternative to the conventional XRR. It demonstrates the possibility to provide express analysis of a thin film or membrane. The main advantages of HXRI are the high space resolution (tens of microns), high angular resolution (easy to resolve films with micrometer thickness) and non-scanning geometry, which give opportunity for real-time observations. In the present work, Kiessig fringes were resolved on 200-, 500 - and 1000 nm-thick Si_3N_4 membranes with the help of HRXI, and PMMA film degradation process under X-ray radiation was observed.

The main advantages of the X-ray optical Fourier transform method as compared to the standard SEM analysis, are:

- carrying out the experiment under any external pressure and temperature conditions. It is difficult for SEM experiment which requires vacuum;

- a statistical one-off analysis of a group of nano-objects. The Fourier analysis gives information about the collective perfection of nano-objects. This type of analysis greatly simplifies the study of nanostructured object as a whole;
- carrying out *in situ* and *on operando* experiments that are technologically difficult for SEM analysis;
- carrying out the nano-objects volume analysis despite of surface analysis typical for SEM technique.

The future of CRL FT belongs to the creation of a multifunctional dark-field X-ray microscope[53] similar to the Transmission Electron Microscope (TEM) in performing images in real and reciprocal spaces with the help of optics. Apart from that, the new concept could give an impetus to the development of 3-dimensional analysis of crystal's reciprocal spaces. It is important to have a complete picture of crystal's diffraction in order to minimize the probability of false experimental data interpretation.

The HXRI gives an opportunity to solve new scientific problems, such as:

- The study micro-structured films/membranes; the analysis of specific films regions;
- The study of highly curved coating surfaces;
- The study of coatings resistance to X-ray radiation;
- The study of rapid processes (occurring within less than a second) inside material thicknesses.

List of abbreviations

Bragg High Resolution X-ray Microscopy	BHRXM
Compound refractive lenses	CRL
Compound refractive lenses Fourier transform	CRL FT
European Synchrotron Radiation Facility	ESRF
Free Electron Laser	FEL
Fourier transform	FT
Fresnel Zone Plate	FZP
Hard X-ray Reflecto-Interferometer	HXRI
High Resolution X-ray Diffractometry	HRXRD
Lenses Fourier Transform	LFT
Linear accelerator	LINAC
Micro-Optics Test Bench	MOTB
Order Sorting Aperture	OSA
Reciprocal Space Mapping	RSM
Self Amplified Stimulated Emission	SASE
Synchrotron Radiation Facility	SRF
Transmission High Resolution X-ray Microscopy	THXM
X-ray Reflectivity	XRR

Results of work & merits

On the topic of the dissertation the following articles have been published:

- Ershov, P., et al., Fourier crystal diffractometry based on refractive optics. Journal of Applied Crystallography, 2013. 46(5): p. 1475-1480.
- Ershov, P., et al. X-ray refractive optics as a Fourier transformer for high resolution diffraction. in Damage to VUV, EUV, and X-Ray Optics IV; and EUV and X-Ray Optics: Synergy Between Laboratory and Space III. 2013. Prague.
- Ershov, P.A., et al., High-resolution X-ray diffraction based on 1D and 2D refractive lenses. Journal of Surface Investigation. X-ray, Synchrotron and Neutron Techniques, 2015. 9(3): p. 576-580.

I'm participating with the dissertation topics at conferences:

- "Damage to VUV, EUV, and X-ray Optics IV; and EUV and X-ray Optics: Synergy between Laboratory and Space III", SPIE, Prague, 2013;
- "22nd International Congress on X-ray Optics and Microanalysis", Hamburg, 2013;
- "Science of the future", Saint-Petersburg, 2014;
- "Smart Nanomaterials and X-ray Optics", Kaliningrad, 2014.

The personal contributions to the article were assembling and setting experiments at the synchrotron and the subsequent processing of the experimental results.

I was taken part in projects nos. 14.Y26.31.0002 and 02.G25.31.0086 of Ministry of Education and Science of the Russian Federation.

Besides the theme of the dissertation, I was also the co-author of the following scientific publications:

- Minnekaev, M., et al., Structural, ferroelectric, electronic and transport properties of BaTiO3/Pt heterostructures grown on MgO (001). Microelectronic Engineering, 2013. 109: p. 227-231.
- Medvedeva, S.S., et al., On the use of a ZrO x -SiO2 multilayer structure as a test sample for high-resolution X-ray microscopy. Journal of Surface Investigation. X-ray, Synchrotron and Neutron Techniques, 2015. 9(2): p. 341-345.
- Goikhman, A., et al., Highly porous nanoberyllium for X-ray beam speckle suppression. J Synchrotron Radiat, 2015. 22(Pt 3): p. 796-800.
- Kononenko, T.V., et al., Fabrication of polycrystalline diamond refractive X-ray lens by femtosecond laser processing. Applied Physics A, 2016. 122(3): p. 1-6.

- Dudchik, Y.I., et al., X-ray microbeam formation at the laboratory source using compound X-ray refractive lenses with short focal length. Journal of Surface Investigation. X-ray, Synchrotron and Neutron Techniques, 2016. 10: p. 1-6.
- Dubrovinskaia, N., et al., Terapascal static pressure generation with ultrahigh yield strength nanodiamond. Science Advances, 2016. 2(7).
- Polikarpov, M., et al. Diamond X-ray refractive lenses produced by femto-second laser ablation. 2016.

I'm a coauthor of the patent «Device for optical characteristic determination by interferometric pattern", registered as Utility Model at national registry of utility models of Russian Federation, № 155377.

Bibliography

[1] A. Bosak, I. Snigireva, K.S. Napolskii, A. Snigirev, High-Resolution Transmission X-ray Microscopy: A New Tool for Mesoscopic Materials, Advanced Materials, 22 (2010) 3256-3259.
[2] B. Lengeler, C.G. Schroer, M. Richwin, J. Tümmler, M. Drakopoulos, A. Snigirev, I. Snigireva, A microscope for hard X-rays based on parabolic compound refractive lenses, Applied Physics Letters, 74 (1999) 3924.
[3] A.A. Snigirev, V. Kohn, Bragg-Fresnel optics at the ESRF: microdiffraction and microimaging applications, in: X-Ray Microbeam Technology and Applications, San Diego, CA, USA, 1995, pp. 27-37.
[4] D. Michael, S. Anatoly, S. Irina, S. Jörg, X-ray high-resolution diffraction using refractive lenses, Applied Physics Letters, (2005) 014102.
[5] J.M. Rodenburg, A.C. Hurst, A.G. Cullis, B.R. Dobson, F. Pfeiffer, O. Bunk, C. David, K. Jefimovs, I. Johnson, Hard-x-ray lensless imaging of extended objects, Phys Rev Lett, 98 (2007) 034801.
[6] A. Snigirev, V. Kohn, I. Snigireva, A. Souvorov, B. Lengeler, Focusing high-energy x rays by compound refractive lenses, Applied optics, 37 (1998) 653-662.
[7] C. Schroer, B. Benner, M. Kuhlmann, O. Kurapova, B. Lengeler, F. Zoutone, A. Snigirev, I. Snigireva, H. Schulte-Schrepping, Focusing Hard X-ray FEL Beams with Parabolic Refractive Lenses, in: Proc. SPIE.
[8] B. Lengeler, C. Schroer, J. Tümmler, B. Benner, M. Richwin, A. Snigirev, I. Snigireva, M. Drakopoulos, Imaging by parabolic refractive lenses in the hard X-ray range, Journal of Synchrotron Radiation, 6 (1999) 1153-1167.
[9] A. Snigirev, V. Kohn, I. Snigireva, B. Lengeler, A compound refractive lens for focusing high-energy X-rays, Nature, 384 (1996) 49-51.
[10] A. Snigirev, B. Filseth, P. Elleaume, T. Klocke, V. Kohn, B. Lengeler, I. Snigireva, A. Souvorov, J. Tummler, Refractive lenses for high-energy x-ray focusing, Proceedings of SPIE, 3151 (1997) 164-170.
[11] V. Kohn, I. Snigireva, A. Snigirev, Diffraction theory of imaging with X-ray compound refractive lens, Optics Communications, 216 (2003) 247-260.
[12] P. Ershov, S. Kuznetsov, I. Snigireva, V. Yunkin, A. Goikhman, A. Snigirev, Fourier crystal diffractometry based on refractive optics, Journal of Applied Crystallography, 46 (2013) 1475-1480.
[13] A.V. Petukhov, J.H.J. Thijssen, D.C.t. Hart, A. Imhof, A.v. Blaaderen, I.P. Dolbnya, A. Snigirev, A. Moussaid, I. Snigireva, Microradian X-ray diffraction in colloidal photonic crystals, Journal of Applied Crystallography, 39 (2006) 137-144.
[14] W.K. Rontgen, On A New Kind of Rays, CA: A Cancer Journal for Clinicians, 22 (1972) 153-157.
[15] P. Willmott, Introduction, in: An Introduction to Synchrotron Radiation, John Wiley & Sons, Ltd, 2011, pp. 15-28.
[16] E. Hecht, Optics, Addison-Wesley, 2002.

[17] J.K. Albert C. Thompson, David T. Attwood, Eric M. Gullikson, Malcolm R. Howells, Jeffrey B. Kortright, Yanwei Liu, and Arthur L. Robinson, X-ray data booklet, in: Third (Ed.), Center for X-ray Optics, Advanced Light Source, Berkeley, California 94720, 2009, pp. 38-52.
[18] P. Willmott, An Introduction to Synchrotron Radiation: Techniques and Applications, in, Wiley, 2011, pp. 50-52.
[19] J. Als-Nielsen, D. McMorrow, Elements of Modern X-ray Physics, John Wiley & Sons, 2011.
[20] K. Fezzaa, F. Comin, S. Marchesini, R. Coisson, M. Belakhovsky, X-Ray Interferometry at ESRF Using Two Coherent Beams from Fresnel Mirrors, J X Ray Sci Technol, 7 (1997) 12-23.
[21] A. Snigirev, I. Snigireva, V. Kohn, V. Yunkin, S. Kuznetsov, M.B. Grigoriev, T. Roth, G. Vaughan, C. Detlefs, X-ray nanointerferometer based on si refractive bilenses, Phys Rev Lett, 103 (2009) 064801.
[22] V. Kohn, I. Snigireva, A. Snigirev, Direct measurement of transverse coherence length of hard x rays from interference fringes, Physical Review Letters, 85 (2000) 2745-2748.
[23] T. Skarzynski, Collecting data in the home laboratory: evolution of X-ray sources, detectors and working practices, Acta Crystallographica Section D, 69 (2013) 1283-1288.
[24] H. Ebel, X-ray tube spectra, X-Ray Spectrom., 28 (1999) 255-266.
[25] A.A. Shaltout, On X-ray tube spectra, the dependence on the angular and electron energy of X-rays from the targets, Eur. Phys. J. Appl. Phys., 37 (2007) 291-297.
[26] S.L. Hulbert, J.M. Weber, Flux and brightness calculations for various synchrotron radiation sources, Nuclear Instruments and Methods in Physics Research Section A: Accelerators, Spectrometers, Detectors and Associated Equipment, 319 (1992) 25-31.
[27] H.R. Rudolf Dimper, Pantaleo Raimondi, Luis Sánchez Ortiz, Francesco Sette and Jean Susini., ESRF UPGRADE PROGRAMME PHASE II (2015-2022) TECHNICAL DESIGN STUDY, Orange book, ESRF, ESRF, 2015.
[28] O. Hemberg, M. Otendal, H.M. Hertz, Liquid-metal-jet anode electron-impact x-ray source, Applied Physics Letters, 83 (2003) 1483.
[29] W.H. Bragg, X-rays and Crystals, Letter to: Nature, (1912) 219.
[30] A. Snigirev, I. Snigireva, High energy X-ray micro-optics, Comptes Rendus Physique, 9 (2008) 507-516.
[31] I. Snigireva, A. Snigirev, S. Kuznetsov, C. Rau, T. Weitkamp, L. Shabel'nikov, M. Grigoriev, V. Yunkin, M. Hoffmann, E. Voges, Refractive and diffractive X-ray optical elements, in: I. McNulty (Ed.) X-Ray Micro- and Nano-Focusing: Applications and Techniques II, San Diego, CA, 2001, pp. 64-73.
[32] S. Tamura, M. Yasumoto, N. Kamijo, K. Uesugi, A. Takeuchi, Y. Terada, Y. Suzuki, Quasi-kinoform type multilayer zone plate with high diffraction efficiency for high-energy X-rays, Journal of Physics: Conference Series, 186 (2009) 012075.
[33] V.V. Aristov, Y.A. Basov, G.N. Kulipanov, V.F. Pindyurin, A.A. Snigirev, A.S. Sokolov, Focusing properties of a Bragg-Fresnel lens in the white spectrum of synchrotron radiation, Nuclear Inst. and Methods in Physics Research, A, 274 (1989) 390-393.

[34] V.G. Kohn, An exact theory of imaging with a parabolic continuously refractive X-ray lens, J. Exp. Theor. Phys., 97 (2003) 204-215.
[35] A. Goikhman, I. Lyatun, P. Ershov, I. Snigireva, P. Wojda, V. Gorlevsky, A. Semenov, M. Sheverdyaev, V. Koletskiy, A. Snigirev, Highly porous nanoberyllium for X-ray beam speckle suppression, J Synchrotron Radiat, 22 (2015) 796-800.
[36] A. Snigirev, I. Snigireva, G. Vaughan, J. Wright, M. Rossat, A. Bytchkov, C. Curfs, High energy X-ray transfocator based on Al parabolic refractive lenses for focusing and collimation, Journal of Physics: Conference Series, 186 (2009) 012073.
[37] G.B. Vaughan, J.P. Wright, A. Bytchkov, M. Rossat, H. Gleyzolle, I. Snigireva, A. Snigirev, X-ray transfocators: focusing devices based on compound refractive lenses, J Synchrotron Radiat, 18 (2011) 125-133.
[38] J.W. Goodman, Introduction to Fourier Optics, McGraw-Hill, 1996.
[39] K.S. Napolskii, I.V. Roslyakov, A.A. Eliseev, A.V. Petukhov, D.V. Byelov, N.A. Grigoryeva, W.G. Bouwman, A.V. Lukashin, K.O. Kvashnina, A.P. Chumakov, S.V. Grigoriev, Long-range ordering in anodic alumina films: a microradian X-ray diffraction study, Journal of Applied Crystallography, 43 (2010) 531-538.
[40] D. Roshchupkin, D. Irzhak, A. Snigirev, I. Snigireva, L. Ortega, A. Sergeev, Diffraction of a focused x-ray beam from La3Ga5SiO14 crystal modulated by surface acoustic waves, J Appl Phys, 110 (2011) 124902.
[41] W.L. Bragg, The Diffraction of Short Electromagnetic Waves by a Crystal., Proceedings of the Cambridge Philosophical Society, (1913) 43-57.
[42] M.v. Laue, Eine quantitative Prufung der Theorie fur die Interferenzerscheinungen bei Rontgenstrahlen., Annalen der Physik, (1913) 989-1003.
[43] P.P. Ewald, Dispersion und Doppelbrechung von Elektronengittern (Kristallen), Konigl. Ludwigs-Maximilians-Universitat zu Munchen., 1912.
[44] P.P. Ewald, Kristalle und Röntgenstrahlen: mit 189 Abbildungen, Berlin, 1923.
[45] D.K. Bowen, B.K. Tanner, High resolution X-ray diffractometry and topography, Taylor & Francis, London, Bristol, PA, 1998.
[46] U. Pietsch, V. Holy, T. Baumbach, High-Resolution X-Ray Scattering: From Thin Films to Lateral Nanostructures, Springer, 2004.
[47] V.V. Aristov, A.Y. Nikulin, A.A. Snigirev, P. Zaumseil, Experimental investigation of X-ray bragg diffraction on the periodic surface relief of a perfect crystal, Phys Status Solidi A, 95 (1986) 81-86.
[48] A.Y.N. V.V. Aristov, A.A. Snigirev, P. Zaumseil, Experimental Investigation of X-ray Bragg Diffraction on the Periodic Surface Relief of a Perfect Crystal, Phys Status Solidi A, 95 (1986).
[49] J. Daillant, A. Gibaud, X-ray and Neutron Reflectivity: Principles and Applications, Springer, 2009.
[50] A. Snigirev, I. Snigireva, M. Lyubomirskiy, V. Kohn, V. Yunkin, S. Kuznetsov, X-ray multilens interferometer based on Si refractive lenses, Optics express, 22 (2014) 25842-25852.
[51] N. Dubrovinskaia, L. Dubrovinsky, N.A. Solopova, A. Abakumov, S. Turner, M. Hanfland, E. Bykova, M. Bykov, C. Prescher, V.B. Prakapenka, S. Petitgirard, I.

Chuvashova, B. Gasharova, Y.-L. Mathis, P. Ershov, I. Snigireva, A. Snigirev, Terapascal static pressure generation with ultrahigh yield strength nanodiamond, Science Advances, 2 (2016).
[52] D. Roshchupkin, L. Ortega, A. Snigirev, I. Snigireva, X-ray imaging of the surface acoustic wave propagation in La 3Ga5SiO14 crystal, in: 2013 Joint European Frequency and Time Forum and International Frequency Control Symposium, EFTF/IFC 2013, Prague, 2013, pp. 683-686.
[53] H. Simons, A. King, W. Ludwig, C. Detlefs, W. Pantleon, S. Schmidt, I. Snigireva, A. Snigirev, H.F. Poulsen, Dark-field X-ray microscopy for multiscale structural characterization, Nat Commun, 6 (2015) 6098.
[54] V. Kohn, I. Snigireva, A. Snigirev, Interferometric characterization of spatial coherence of high energy synchrotron X-rays, Optics Communications, 198 (2001) 293-309.
[55] H. Kiessig, Untersuchungen zur Totalreflexion von Röntgenstrahlen, Annalen der Physik, 402 (1931) 715-768.
[56] R.W. James, The optical principles of the diffraction of X-rays, Cornell University Press, Ithaca, N.Y., 1967.
[57] A. Snigirev, R. Hustache, P. Duboc, J.Y. Massonnat, L. Claustre, P. Van Vaerenbergh, I. Snigireva, M. Grigoriev, V. Yunkin, Micro-optics test bench at the ESRF, Proceedings of SPIE, 6705 (2007) 670511-670514.
[58] S. Kuznetsov, I. Snigireva, A. Souvorov, A. Snigirev, New Features of X-Ray Bragg Diffraction Topography with Coherent Illumination, Phys. Status Solidi A Appl. Mater. Sci., 172 (1999) 3-13.
[59] V.V. Aristov, Y.A. Basov, S.V. Redkin, A.A. Snigirev, V.A. Yunkin, Bragg zone plates for hard X-ray focusing, Nuclear Inst. and Methods in Physics Research, A, 261 (1987) 72-74.
[60] Y. Yamamoto, P. Zaumseil, T. Arguirov, M. Kittler, B. Tillack, Low threading dislocation density Ge deposited on Si (100) using RPCVD, Solid-State Electronics, 60 (2011) 2-6.
[61] H. Rucker, B. Heinemann, W. Winkler, R. Barth, J. Borngraber, J. Drews, G.G. Fischer, A. Fox, T. Grabolla, U. Haak, D. Knoll, F. Korndorfer, A. Mai, S. Marschmeyer, P. Schley, D. Schmidt, J. Schmidt, M.A. Schubert, K. Schulz, B. Tillack, D. Wolansky, Y. Yamamoto, A 0.13 υμ SiGe BiCMOS Technology Featuring f_T/f_{max} of 240/330 GHz and Gate Delays Below 3 ps, IEEE Journal of Solid-State Circuits, 45 (2010) 1678-1686.
[62] D. Zubia, S.D. Hersee, Nanoheteroepitaxy: The Application of nanostructuring and substrate compliance to the heteroepitaxy of mismatched semiconductor materials, J Appl Phys, 85 (1999) 6492.
[63] D. Zubia, S.H. Zaidi, S.D. Hersee, S.R.J. Brueck, Nanoheteroepitaxy: Nanofabrication route to improved epitaxial growth, J Vac Sci Technol B, 18 (2000) 3514.
[64] P. Zaumseil, Y. Yamamoto, A. Bauer, M.A. Schubert, T. Schroeder, X-ray characterization of Ge epitaxially grown on nanostructured Si(001) wafers, J Appl Phys, 109 (2011) 023511.

Acknowledgements

First of all, I am grateful to Dr. Anatoly Snigirev and Dr. Irina Snigirev for their scientific supervising.

I am grateful to the Ministry of Education and Science of Russian Federation for their material support of my research.

I am grateful to Dr. Anna Perelomova for her help and her constructive critique.

I am grateful to Dr. Alexander Goikhman for his help, support, critique.

I am grateful to Dr. Mikhail Lyubomirskiy for his constructive (and non-constructive) critique of my work. By him I try to work harder.

I am grateful to the Immanuel Kant Baltic Federal University for supporting of my studies.

I am grateful to the ESRF. Especially I grateful to the Carsten Detlefs for tech support and nice discussions.

I am grateful to the REC "FN" team for cooperation. Ivan Lyatun, Svetlana Medvedeva, Dmitrii Zverev, Nataly Klimova, Pavel Prokopovich, Maxim Polikarpov, Anastasia Vinarskaya, Alexander Borisov, Olga Toropova, Inna Smirnova, Ekaterina Makarova, Anton Narikovich, Polina Medvedskaya.

I am grateful to my collaborators for interesting discussions and joint activities.

I am grateful to the developers of:

- ImageJ;

-Gwyddion;

- Sergey Stepanov's X-ray Server;

- CXRO database;

- Origin Lab;

- Microsoft Office & Windows.